

Simulation of Metal Quenching Processes for the Minimization of Distortion and Stresses

Dissertation

zur Erlangung des akademischen Grades

Doktoringenieur

(Dr.-Ing.)

vorgelegt von

M.Sc. Yalçın Kaymak

geb. am 08.07.1978

in Ankara, Türkei

genehmigt durch die

Fakultät für Verfahrens- und Systemtechnik
der Otto-von-Guericke-Universität Magdeburg

Gutachter:

Prof. Dr.-Ing. E. Specht, Universität Magdeburg
Prof. Dr.-Ing. A. Bertram, Universität Magdeburg

eingereicht am 02.07.2007

Promotionskolloquium am 12.10.2007

Preface

This dissertation is submitted to Otto-von-Guericke-University, Magdeburg for the degree of Doctor of Engineer. The research described herein was conducted under the supervision of Prof. E. Specht and Prof. A. Bertram between May 2003 and July 2007. To the best of my knowledge, this work is original, except where suitable references are made to previous works. Neither this, nor any substantially similar dissertation has been submitted for any degree, diploma or qualification at any other university or institution.

Yalçın Kaymak
Magdeburg, 02.07.2007

If we knew what it was we were doing, it would not be called research, would it?

Albert Einstein (1879-1955)

Acknowledgement

I would like to express my sincere gratitude to Prof. E. Specht for his guidance, knowledge, encouragement and great enthusiasm. I am extremely grateful to Prof. A. Bertram for his constant support and friendship. I am extremely grateful to both of my supervisors, Prof. E. Specht and Prof A. Bertram for their guidance and support, and for their unique way of teaching the simplicity and beauty of everything that surrounds us. I acknowledge the German Research Foundation for providing me with a scholarship to pursue this Ph.D. degree. It is my pleasure to acknowledge all the members of Graduiertenkolleg-828, past and present, for their assistance, friendship and for many enjoyable times, in particular Miroslaw Brzoza and Shabi Ulzama. It was an enormous pleasure to work with them. Thanks also to my friends and to the people I met in Otto-von-Guericke-University, Magdeburg. Thanks to iğdem Sevinç for her passions and understanding, and also for all the wisdom she gave me throughout this time. I would like to thank all the Turkish friends in Magdeburg for their endless sharing and friendship. Last but not the least, I would like to express my thanks to my junior Ashok Kumar Nallathambi for helping me to enrich the quality of this dissertation. Finally, I take this opportunity to express my deepest gratitude to my family and specially my parents Asiye and Ali Sait Kaymak for their love and unfailing support, without which I won't be able have the achievement at all.

Dedication

I would like to dedicate this small piece of work to my parents (Asiye and Ali Sait), without whose grace, love and forbearance it would not have been possible for me to learn many things not only in science but even in general aspects of life in the course of these four years and all through my life.

Abstract

A complex thermo-mechanical model and its finite element implementation for simulating the transient fields of the temperature, micro structure, stress, strain, and displacement during a heat treatment process is introduced. At the integration points, the temperature, phase fractions, Scheil's sum, plastic strain, transformation induced plastic strain tensors, hardening parameter, and stress tensor is stored as state variables at each time step. The thermo-plastic material model is reformulated with a temperature and phase fraction dependent yield limit on the basis of J_2 -plasticity theory. Each phase has its own material properties, which are used for computing mixture material properties. Coupling effects such as dissipation of mechanical energy into heat energy, phase transformation enthalpy, and transformation induced plasticity (TRIP) are considered. The developed model is validated by comparing the simulation results with available experimental measurements. Many simulations have been carried out in order to investigate the optimum cooling strategies for avoiding the distortion and reducing stresses for various geometries such as long profiles, disks and shafts made of 100Cr6, C45, C80 and aluminum. The results have shown that by reducing the cooling at thin parts and edges as well as increasing the cooling at thicker parts, the distortion and stresses can be reduced concurrently.

Keywords: Quenching process, TRIP, J_2 -plasticity theory, phase transition, distortion

Zusammenfassung

Ein kompliziertes thermomechanisches Modell und seine Finite Elemente Formulierung für das Simulieren des transient Feldes von der Temperatur, Mikrostruktur, Spannung, Dehnung und die Gestaltänderungen (Verzug), werden während eines Wärmebehandlungsprozesses dargelegt. An den Integrationspunkten wird die Temperatur, Phasenanteile, die Summe des Scheil, plastischer Dehnungstensor, Phasenumwandlung plastischer Dehnungstensor, der Verfestigungsparameter und Spannungstensor als Zustandsvariablen an jeden Zeitabschnitt gespeichert. Das Modell des thermoplastischen Materials wird neu formuliert, auf der Grundlage von der J_2 -Plastizitätstheorie, die Streckspannung ist abhängig von der Temperatur und der Phaseanteile. Jede Phase hat seine eigenen materiellen Eigenschaften, diese werden für die Berechnung der Mischungseigenschaften benutzt. Koppelungseffekte wie die Umwandlung von mechanischer Energie in Wärme, Phasenumwandlungsenthalpie und Phasenumwandlungsplastizität (PUP) werden Berücksichtigt. Das entwickelte Modell wird überprüft, indem man die Simulationsresultate mit vorhandenen experimentellen Messungen vergleicht. Viele Simulationen sind durchgeführt worden, um nach optimalen abkühlenden Strategien, für das Vermeiden der Verzerrung sowie das Reduzieren der Spannung für verschiedene Geometrien, wie z. B. langen Profilen, Scheiben und Wellen zu Forschen, die aus 100Cr6, C45, C80 und Aluminium bestehen. Die Resultate haben gezeigt, dass durch das Verringern des Abkühlens, an den schmalen Bereichen und an den Rändern, sowie die Erhöhung des Abkühlens an den breiten Bereichen, die Verzerrung und die Spannung gleichzeitig reduziert werden können.

Schlagwörter: Wärmebehandlungsprozess, PUP, J_2 -Plastizitätstheorie, Phasenumwandlung, Verzerrung

Contents

Preface	i
Acknowledgement	iii
Dedication	v
Abstract	vii
Zusammenfassung	ix
List of Tables	xv
List of Figures	xx
Abbreviations	xxi
1 Introduction	1
1.1 Motivation	1
1.2 Common cooling problems	4
1.3 Common existing solutions	7
1.3.1 Press hardening	7
1.3.2 Straightening	7
1.3.3 Stretching	9
1.4 Distortion engineering	9
1.5 Summary	9
2 Literature review	11
2.1 Introduction	11
2.2 Phase transformation kinetics	12
2.3 Constitutive relations	13
2.4 Coupling phenomena	13
2.4.1 Dilatation due to temperature and phase changes	13
2.4.2 Transformation induced plastic strains (TRIP)	14
2.4.3 Dissipation of mechanical energy into heat	14
2.5 Estimation of mixture material properties	15
2.6 Mathematical models for coupled field applications	15
2.6.1 Quenching	15
2.6.2 Welding	16
2.7 Summary	16

3	Mathematical modeling	17
3.1	Temperature field	17
3.2	Micro-structure field	18
3.2.1	TTT charts and diffusive transformations	18
3.2.2	Displacive transformation	20
3.3	Displacement field	20
3.3.1	Plasticity formulation	20
3.3.2	Dilatation due to temperature and phase changes	23
3.3.3	Transformation induced plasticity (TRIP)	23
3.4	Generalized mixture rule for material properties	23
3.5	Description of the distortion	25
3.6	Summary	26
4	Finite element modeling	27
4.1	Reasons to choose finite element method	27
4.2	Solution algorithm	27
4.3	Temperature field formulation	28
4.3.1	Preliminaries	28
4.3.2	Two-dimensional elements	31
4.3.3	Three-dimensional element	32
4.4	Phase field formulation	34
4.4.1	Computation of diffusional phase fractions	34
4.4.2	Computation of displacive phase fractions	36
4.5	Displacement field formulation	36
4.5.1	Preliminaries	36
4.5.2	Two-dimensional elements	39
4.5.3	Three-dimensional element	41
4.5.4	Integration scheme for the plastic strains	44
4.6	Summary	45
5	Validation of mathematical model	47
5.1	Introduction	47
5.2	Validation of temperature field formulation	47
5.3	Validation of phase transformation formulation	52
5.4	Validation of displacement field formulation	53
5.5	Comparison with experimental results	54
5.5.1	Necessity of experiments	54
5.5.2	Shaft with notches	54
5.5.3	Disk with a hole	56
5.6	Summary and conclusions	57
6	Simulation results	59
6.1	Introduction	59
6.2	L profiles made of 100Cr6	60
6.3	L profiles made of C80	67
6.4	L profiles made of C45	70
6.5	Mesh convergence test	74
6.6	Comparison of different sizes	76
6.7	Comparison of different optimums	79
6.8	Comparison of different materials	80

6.9	T profiles made of aluminum	81
6.10	Comparison of different geometries	84
6.11	Disks made of 100Cr6	89
6.12	Effects of material properties on	93
6.12.1	Effects of mechanical material properties	93
6.12.2	Effects of thermal material properties	95
6.12.3	Effects of metallurgical material properties	96
6.13	Summary and conclusions	98

Appendix **105**

A Material properties **107**

A.1	Steel 100Cr6	107
A.2	Steel C45	112
A.3	Steel C80	115
A.4	Aluminum	117

Curriculum Vitae **121**

List of Tables

5.1	Numerical values of temperature from analytical and numerical solutions in time	51
5.2	Numerical values of temperature from analytical and numerical solutions in space	52
5.3	Calculated and measured phase fractions for the shafts	56
5.4	Calculated and measured phase fraction for the cutting disks	57
6.1	Required computer resources for different meshes and time steps	74
A.1	Material properties of steel 100Cr6 [Pie00]	107
A.2	Numerical values for IT and CCT graphs and their graph, (100Cr6)	111
A.3	Material properties of steel C45 [Pie00]	112
A.4	Material properties of steel C80 [Pie00]	115
A.5	Material properties of Aluminum [MPD99]	117

List of Figures

1.1	Variation of temperature in a typical heat treatment process . . .	2
1.2	Typical distortion of an L, T or U profile after cooling	4
1.3	Typical distortion of plates after cooling [YM03]	5
1.4	Schematic description of cutting saw distortion	5
1.5	Typical distortion of steel cutting saw after cooling	6
1.6	Geometry of the disk with a hole	6
1.7	Geometry of the shaft with notches	6
1.8	Mechanism of press hardening equipment	7
1.9	Schematic representation of a role arranging	8
1.10	Flame straightening of a plate with 3 flame nozzles	8
2.1	Couplings of temperature, micro-structure and displacement fields	12
3.1	Crystallographic structure of Face centered cubic (FCC) iron and body centered cubic (BCC) iron lattice	18
3.2	Typical TTT diagram for steel [Hoe96]	19
3.3	Typical plastic loading increment in stress space	22
3.4	Micro regional orthotropy due to effect of phase distribution . . .	24
3.5	Deflection of an L profile, definition of the distortion by curvature, and central hole of the cutting disk before and after the cooling .	26
4.1	Quadrilateral parent element and its typical mapping to global coordinates	31
4.2	3D parent element and its node numbering for temperature field calculations	33
4.3	Illustration of the Scheil's sum algorithm	35
4.4	Typical 2D element for displacement calculation	39
4.5	Typical 3D parent element and its node numbering	42
5.1	Geometry of the solid prism for analytical solution of convective cooling	48
5.2	Error in computed temperature θ_1 at the corner vs. time	49
5.3	Error in computed temperature θ_2 on the mid-surface vs. time .	50
5.4	Error in computed temperature θ_3 in the core vs. time	50
5.5	Error in computed temperature θ between the core and mid-surface	51
5.6	Comparison of IT diagram, computed CCT diagram and CCT diagram from the data sheet (provided by Saarlstahl [Fig. A.6 and Fig. A.7]), for the pearlitic transformation of a typical steel	52

5.7	Variation of martensite fraction after the cooling depending on cooling time	53
5.8	Patch test problem with its mesh and material model	54
5.9	Geometry of notched shaft and disk	54
5.10	Geometrical dimensions [in <i>mm</i>] of big and small shaft	55
5.11	Calculated and measured values of stress at different positions [BSO ⁺ 05, BSO ⁺ 06]	55
5.12	Actual dimensions of the disk with a hole and its idealization for modeling	56
5.13	Comparison of experimental and calculated radial displacement of the hole for the big disk on the top and small disc on the bottom	57
6.1	Distortion, average and max. residual stress vs. HTC α (100Cr6, L profile)	60
6.2	Average temperature and max. temperature difference vs. time for different HTC α (100Cr6, L profile)	61
6.3	Phase fractions vs. time for different HTC α (100Cr6, L profile)	62
6.4	Distortion vs. time for different HTC α (100Cr6, L profile)	62
6.5	Distortion of L profile at different stages of cooling	63
6.6	Average residual stress and maximum residual stress vs. time for different HTC α (100Cr6, L profile)	63
6.7	Distortion and average residual stress vs. HTC α_1 at mass lumped region (100Cr6, L profile)	64
6.8	Average temperature and max. temperature difference vs. time for different cooling strategies (100Cr6, L profile)	65
6.9	Phase fractions vs. time for different cooling strategies (100Cr6, L profile)	65
6.10	Distortion vs. time for different cooling strategies (100Cr6, L profile)	66
6.11	Average temperature and max. temperature difference vs. time for different cooling strategies (100Cr6, L profile)	66
6.12	Average residual stress and maximum residual stress vs. time for different cooling strategies (C80, L profile)	67
6.13	Average temperature and max. temperature difference vs. time for different HTC α (C80, L profile)	68
6.14	Phase fractions vs. time for different HTC α (C80, L profile)	68
6.15	Distortion vs. time for different HTC α (C80, L profile)	69
6.16	Average residual stress and maximum residual stress vs. time for different HTC α (C80, L profile)	70
6.17	Distortion and average residual stress vs. HTC α (C45, L profile)	71
6.18	Average temperature and max. temperature difference vs. time for different HTC α (C45, L profile)	72
6.19	Phase fractions vs. time for different HTC α (C45, L profile)	72
6.20	Distortion vs. time for different HTC α (C45, L profile)	73
6.21	Average residual stress and maximum residual stress vs. time for different HTC α (C45, L profile)	73
6.22	Three different meshes considered in the mesh convergence analysis (Aluminum, L profile)	74
6.23	Distortion vs. time for different meshes and time steps (Aluminum, L profile)	75

6.24	Maximum residual stress vs. time for different meshes and time steps (Aluminum, L profile)	75
6.25	Contours of max. residual stress for different meshes (Aluminum, L profile)	76
6.26	Distortion vs. HTC α for different sizes of Aluminum L profiles .	76
6.27	Average residual stress vs. HTC α for different sizes of aluminum L profile	77
6.28	Distortion vs. time for different sizes of aluminum L profiles . . .	77
6.29	Average temperature and max. temperature difference vs. time for different sizes of aluminum L profiles	78
6.30	Average residual stress and max. residual stress vs. time for different sizes of aluminum L profiles	78
6.31	Distortion vs. time for different optimum coolings (Aluminum, L profile)	79
6.32	Contours of axial residual stress for different optimum coolings (Aluminum, L profile)	80
6.33	Distortion vs. HTC α for different materials (L profile)	81
6.34	Distortion, average residual stress and max. residual stress vs. HTC α (Aluminum, T profile)	82
6.35	Average temperature and max. temperature difference vs. time for different HTC α (Aluminum, T profile)	82
6.36	Distortion vs. time for different HTC α (Aluminum, T profile) .	83
6.37	Average residual stress and max. residual stress vs. time for different HTC α (Aluminum, T profile)	83
6.38	Distortion, average residual stress and max. residual stress vs. time for different cooling strategies (Aluminum, T profile)	84
6.39	Distortion, average residual stress and max. residual stress vs. HTC α (Aluminum, U profile)	85
6.40	Average temperature and max. temperature difference vs. time for different HTC α (Aluminum, U profile)	85
6.41	Distortion vs. time for different HTC α (Aluminum, U profile) .	86
6.42	Average residual stress and max. residual stress vs. time for different HTC α (Aluminum, U profile)	87
6.43	Distortion vs. HTC α for different geometries made of aluminum	87
6.44	Distortion vs. time for different geometries (Aluminum)	88
6.45	Average temperature and max. temperature difference vs. time for different geometries of aluminum profiles	88
6.46	Average residual stress and max. residual stress vs. time for different geometries of aluminum profiles	89
6.47	Distortion, average residual stress and max. residual stress vs. HTC $\alpha_1 - \alpha$ (100Cr6, Disk)	90
6.48	Average temperature and max. temperature difference vs. time for different cooling strategies (100Cr6, Disk)	90
6.49	Phase fractions vs. time for different cooling strategies (100Cr6, Disk)	91
6.50	Average residual stress and max. residual stress vs. time for different different cooling strategies (100Cr6, Disk)	92
6.51	Contours of maximum residual stress for different optimum coolings (100Cr6, Disk)	92
6.52	Distortion vs. time for different cooling strategies (100Cr6, Disk)	93

6.53	Sensitivity of distortion to the mechanical material properties (100Cr6, L profile)	94
6.54	Sensitivity of average stress to the mechanical material properties (100Cr6, L profile)	94
6.55	Sensitivity of maximum stress to the mechanical material properties (100Cr6, L profile)	95
6.56	Sensitivity of distortion to the thermal material properties (100Cr6, L profile)	95
6.57	Sensitivity of average stress to the thermal material properties (100Cr6, L profile)	96
6.58	Sensitivity of maximum stress to the thermal material properties (100Cr6, L profile)	96
6.59	Sensitivity of distortion to the metallurgical material properties (100Cr6, L profile)	97
6.60	Sensitivity of average stress to the metallurgical material properties (100Cr6, L profile)	97
6.61	Sensitivity of maximum stress to the metallurgical material properties (100Cr6, L profile)	98
A.1	Elasticity modulus and Poisson's ratio vs. temperature, (100Cr6)	108
A.2	Hardening modulus and yield strength vs. temperature, (100Cr6)	108
A.3	Heat conductivity and specific heat capacity vs. temperature, (100Cr6)	109
A.4	Density vs. temperature, (100Cr6)	109
A.5	Data sheet supplied by Saarlust AG, Germany (100Cr6)	110
A.6	Isothermal transformation diagram supplied by Saarlust AG, Germany (100Cr6)	110
A.7	Continuous cooling transformation diagram supplied by Saarlust AG, Germany (100Cr6)	111
A.8	Isothermal and continuous cooling transformation diagrams, (100Cr6)	112
A.9	Elasticity modulus and shear modulus vs. temperature, (C45) . .	113
A.10	Hardening modulus and yield strength vs. temperature, (C45) .	113
A.11	Heat conductivity and specific heat capacity vs. temperature, (C45)	114
A.12	Density vs. temperature, (C45)	114
A.13	Elasticity modulus and shear modulus vs. temperature, (C80) . .	115
A.14	Hardening modulus and yield strength vs. temperature, (C80) .	116
A.15	Heat conductivity and specific heat capacity vs. temperature, (C80)	116
A.16	Density vs. temperature, (C80)	117
A.17	Elasticity modulus and Poisson's ratio vs. temperature, (Aluminum)	118
A.18	Hardening modulus and yield strength vs. temperature, (Aluminum)	118
A.19	Heat conductivity and specific heat capacity vs. temperature, (Aluminum)	119
A.20	Density vs. temperature, (Aluminum)	119

Abbreviations

Tensor operations

a : 0^{th} order tensor is a scalar.

$\mathbf{a} \otimes \mathbf{b} = a_i b_j (\mathbf{e}_i \otimes \mathbf{e}_j) = \mathbf{A}$: tensor product of 1^{st} order tensors is a 2^{nd} order.

$\mathbf{A} \otimes \mathbf{B} = A_{ij} B_{kl} (\mathbf{e}_i \otimes \mathbf{e}_j \otimes \mathbf{e}_k \otimes \mathbf{e}_l) = \hat{\mathbf{C}}$: tensor product of 2^{nd} order tensors is a 4^{th} order.

$\mathbf{a} \cdot \mathbf{b} = a_i b_i$: scalar product of 1^{st} order tensors is a scalar.

$\mathbf{A} \cdot \mathbf{b} = A_{ij} b_j \mathbf{e}_i$: scalar product of 2^{nd} order tensor with 1^{st} order tensor is a 1^{st} order.

$\mathbf{A} \cdot \mathbf{B} = A_{ij} B_{ij}$: scalar product of 2^{nd} order tensors is a scalar.

$\hat{\mathbf{C}} \cdot \mathbf{A} = C_{ijkl} A_{kl} (\mathbf{e}_i \otimes \mathbf{e}_j)$: scalar product of 4^{th} order tensor with 2^{nd} order is a 2^{nd} order.

$\nabla \cdot \mathbf{A}$: divergence of a 2^{nd} order tensor is a 1^{st} order.

∇a : gradient of a scalar is a 1^{st} order tensor.

Matrix and vector operations

\mathbf{AB} : multiplication of matrices if sizes are compatible.

$\mathbf{A}\mathbf{b}$: matrix and vector multiplication for compatible size matrices and vector.

$\text{tr}(\mathbf{A})$: trace of a square matrix (or tensor) is the sum of diagonal elements.

$|\mathbf{A}|$: determinant of a square matrix.

$\mathbf{A}^T, \mathbf{a}^T$: transpose of matrix and vector.

$\mathbf{a} \cdot \mathbf{b} = \mathbf{a}^T \mathbf{b}$: dot product of two vectors is a scalar.

$\mathbf{A} : \mathbf{B} = \text{tr}(\mathbf{AB}^T)$: sum of all corresponding multiplied terms is a scalar.

Matrix, tensor and scalar field variables

α	Heat transfer coefficient [$W/m^2/K$]
ε^{pl}	Hardening state variable
$\varepsilon_{\text{eff}}^{pl}$	Effective plastic strain
l	Thickness of 2D elements [m]
σ_{eff}	Effective stress [$Pa = N/m^2$]
σ_m	Mean stress [$Pa = N/m^2$]
θ	Temperature [$^{\circ}C$]
θ_{∞}	Ambient temperature [$^{\circ}C$]
Θ	Nodal temperature vector [$^{\circ}C$]
\mathbf{B}, \mathbf{B}	Strain displacement relations [$1/m$]
$\mathbf{C}, \hat{\mathbf{C}}$	Constitutive relations [$Pa = N/m^2$]

$\hat{\mathbf{P}}_1, \hat{\mathbf{P}}_1$	Spherical projectors
$\hat{\mathbf{P}}_2, \hat{\mathbf{P}}_2$	Deviator projectors
\mathbf{E}, \mathbf{E}	Strain tensors
\mathbf{T}, \mathbf{T}	Stress tensors [$Pa = N/m^2$]
f	Volumetric phase fraction
x, y, z	Global coordinates [m]
r, s, t	Local coordinates
\mathbf{u}	Displacement field [m]
\mathbf{u}^S	Prescribed surface displacement [m]
S_n	Scheil's sum at n^{th} time step
\mathbf{f}^B	Body forces [N/m^3]
\mathbf{f}^S	Prescribed surface traction [$Pa = N/m^2$]
$\hat{\mathbf{I}}$	4^{th} order identity tensor
\mathbf{I}, \mathbf{I}	2^{nd} order identity tensors
$\mathbf{n}^S, \mathbf{n}^S$	Body surface unit normal
$\mathbf{n}'_T, \mathbf{n}'_T$	Flow surface normal and stress deviator direction
\mathbf{N}_e	Element interpolation functions' vector
\mathbf{H}_e	Element interpolation function derivatives' operator [$1/m$]
\mathbf{B}_e	Element strain-displacement operator [$1/m$]
\mathbf{J}_e	Element Jacobian matrix
\mathbf{C}_e	Element capacitance matrix [J/K]
\mathbf{F}_e	Element force vector (mechanical formulation) [N]
\mathbf{R}_e	Element response vector (mechanical formulation) [N]
\mathbf{Q}_e	Element force vector (thermal formulation) [J]
\mathbf{K}_e	Element stiffness matrix (mechanical formulations) [N/m]
\mathbf{K}_e	Element conductance matrix (thermal formulations) [J/K]
$\mathbf{X}_e, \mathbf{Y}_e, \mathbf{Z}_e$	Element x-, y-, z-coordinates [m]
q^V	Heat generation per unit volume [J/m^3]
q^S	Heat flux through the body surface [J/m^2]

Material properties

κ	Bulk modulus [$Pa = N/m^2$]
μ	Shear modulus [$Pa = N/m^2$]
ρ	Density [kg/m^3]
σ_y	Yield strength [$Pa = N/m^2$]
$a_{\sigma m}$	Mean stress coefficient in modified Koistinen-Marburger equation [$1/Pa = m^2/N$]
$a_{\sigma e}$	Effective stress coefficient in modified Koistinen-Marburger equation [$1/Pa = m^2/N$]
c_p	Specific heat capacity [$J/kg/K$]
e	Emissivity
H	Plastic (hardening) modulus [$Pa = N/m^2$]
k	Heat conductivity [$W/m/K$]
k_M	Stress-dependent martensitic transformation constant [$1/K$]
L_i	Latent heat of transformation [J/kg]
M_S	Martensitic transformation start temperature [K]
TTT	Matrix of isothermal transformation data, (θ, t_S, t_E)

Other variables

χ	Fraction of mechanical energy converted into heat
ψ	View factor for thermal radiation
λ	Plastic multiplier
σ	Stefan-Boltzmann constant [$J/s/m^2/K$]
dV	Infinitesimal volume element [m^3]
dA	Infinitesimal area element [m^2]
t_S, t_E	Transformation starting and ending times isothermal case [s]
t_{inc}	Incubation time (time necessary for transformation start in continuous cooling) [s]
S^f	Traction defined surface [m^2]
S^u	Displacement defined surface [m^2]

Chapter 1

Introduction

1.1 Motivation

Quenching or rapid cooling is the most important part in many heat treatment processes, which is performed to obtain the improved mechanical properties of metals. However, quenching provokes residual stresses, which also instigate distortion. A high residual stress state is detrimental since it initiates cracks and shortens the service life of the metal product. Therefore, after the cooling process the high residual stresses should be reduced by an additional process such as stretching or tempering. If the distortion after the cooling exceeds the specified tolerance, then this distortion should be removed with further methods such as straightening, grinding, surface polishing or cutting. The motivation of this thesis is to investigate and develop new cooling strategies for minimizing the residual stress and distortion by adjusting the local cooling. For this purpose a finite element code has been developed and implemented to calculate the coupled thermal, metallurgical and mechanical fields. Heat treatment is the controlled heating and cooling of metals or metal alloys in the solid state to alter their physical and mechanical properties. In micro scale, metallic materials are composed of small grains. Within these grains, the molecules are arranged in a uniform crystallographic pattern. The character of the grains, for instance grain size and composition, establishes the whole mechanical behavior of the metal.

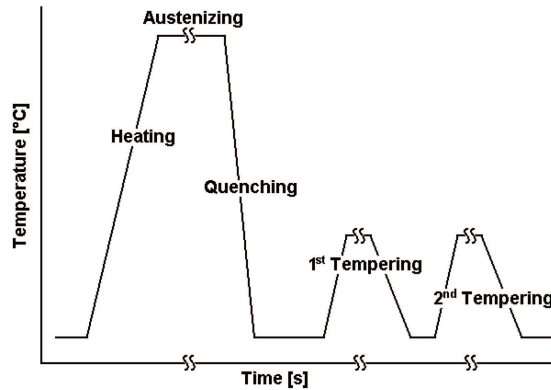


Figure 1.1: Variation of temperature in a typical heat treatment process

Heat treatment is an accomplished technique to influence the properties of the metal by controlling the rate of diffusion within the micro-structure. That means, the same alloy depending on the cooling rates ends up with different micro-structures. Upon being rapidly cooled, the austenite will transform into martensite, a hard brittle crystalline structure, in which the alloying elements are trapped and necessitate a tempering to precipitate inter-metallic particles, thereby achieving the maximum strength and hardness. The desired mechanical properties at room temperature for a specific alloy can be achieved by a designed heat treatment process which requires understanding of phase transformations within the metallic alloys. The variation of the temperature in a typical heat treatment process is shown in Fig. 1.1. The rate of temperature drop is maximized during the quenching. The temperature drop rate is much higher than the temperature increase rate during heating, which precedes the quenching process. Depending on the alloy type, the duration of austenization may vary from minutes to hours and usually tempering duration from hours to days. The heating and cooling rates are much small in the tempering stage to avoid the stresses and distortion.

Usually, a quenched metal is too brittle for further usage without tempering. Depending on the alloy used, it will be evenly heated between 90 and 260°C, held at that temperature for an appropriate time, and then cooled slowly. This heat treatment will ensure strength and ductility by balancing the amount of hard martensite with ductile ferrite and pearlite. In certain cases, different areas of an object may be heat treated differently. This is known as differential hardening, which is common in high quality knives and swords, e.g., the Chinese swords, Japanese katana, and Nepalese Khukuri, and many others.

Quenching induces high residual stresses due to several mechanisms like phase transformation, thermal shrinkage, transformation induced plasticity and yielding. The phase transformation is accompanied by a volume change owing to the rearrangement of the atoms in the crystal structures. The total strain field due to thermal shrinkage and phase transformation becomes non-uniform when the temperature field is non-uniform. Hence, the stress state may go beyond the yield strength of the metal resulting in an elasto-plastic behavior. On the other hand, the distortion is amplified by additional transformation induced plastic strains, which occur during the phase transformation, even when the

stress levels below the yield strength.

After quenching, the high residual stresses should be reduced by an additional process such as stretching and tempering. Stretching provides a uniform plastic strain field throughout the product and the internal stress state is equalized by this way. 2-5% strain is enough for this purpose. However, this method can be applicable to specific geometries such as plates and long profiles. Another method is tempering, which usually follows a quenching operation. Tempering relieves the internal stresses, lowers the hardness to a certain extent, and restores the ductility. Moreover it improves the toughness, refines grain size or changes the electromagnetic properties. Such a softening is a necessary operation when a large amount of cold working has to be performed, e.g., a cold-rolling operation or wire drawing. The stress relieve mechanism in tempering can be explained by the creep phenomena. Creep (stress relaxation) is actually defined as the tendency of a material to move or to deform permanently to relieve stresses in time. Although it takes very long time at room temperature, the effect of creep increases substantially as the temperature approaches to the melting point of the material.

At the end of many quenching processes, the distortion exceeds the specified tolerance. In general, this distortion can be removed with the help of polishing, machining, and straightening processes. Metal polishing, also termed *buffing*, is the process of smoothing and polishing the metals and metal alloys to a clear, mirror-like surface finish. As a general rule, coarse abrasives are used first and fine abrasives are applied later. Machining, which is a part of the manufacturing process of almost all metal products, is a class of metal cutting processes that involves using a power-driven device, such as a lathe, milling machine, drilling machine, etc., to shape the metals. For example, lathe generates circular sections by rotating a metal workpiece, so that a cutting tool can peel metal off, creating a smooth, round surface. Other tools, which may be used for various types of metal removal, are milling machines, saws, and grinding tools. A press is used to flatten a piece of metal into a desired shape. Advanced machining operations might use electrical discharge, electro-chemical erosion, or laser cutting to shape the metal work pieces.

Heat treatment is an indispensable method in many large scale manufacturing industries such as automotive, transportation, aerospace, construction, marine, military, material handling (casting, forging, machinery), and medical/pharmaceutical industries. Heat treatment provides great advantages for example reduced cost, weight, and noise, and also increased strength, durability, dependability, toughness, performance, wear and fatigue resistance. Hence, the metal components of powertrains, engines, turbines, farm/mining/forestry/construction equipments are heat treated. For instance, in aerospace industry the steel and aluminum alloys may undergo five or even more different heat treating operations to develop the desired properties. The most common heat treated metal geometries include profiles, shafts, disks, gears, plates, and so on. Long profiles of different cross-sections (T, L, U, etc.) are common in construction, rail, and other industries. High strength shafts, disks and gears are basic components of powertrains in automotive industry for transmission of the engine rotation to the wheels. Improving the heat treatment techniques for the elimination of associated problems is of great importance and value to the related industries, which makes it a precious challenge for the researchers and scientists.

This dissertation particularly deals with the quenching stage of heat treat-

ment where the high stresses and distortion are generated in common. Quenching may be performed with various fluids like forced air or other gas (such as nitrogen, helium, and argon), oil, polymer dissolved in water, water, brine, etc. The gas or atomized spray quenching in a nozzle field facilitates to alter the local cooling by adjusting the flow rates. It has been proved that the distortion of profiles can be avoided [Pie00, PBK⁺05, PBK⁺07, KS07, KBS05, KBS06], a uniform hardness and a reduced residual stress state in the shafts can be achieved [BSO⁺05, BSO⁺06, BKS05] by locally controlling the quenching. This dissertation discusses the further possibilities to reduce the residual stresses and distortion simultaneously.

1.2 Common cooling problems

Long profiles usually have distortion upon cooling due to the formation of a non-uniform temperature field. Distortion is mainly produced by the volume changes due to thermal shrinkage and solid state phase transformations. At the initial stages of the cooling before phase transitions begin, the low temperature regions shrink more and cause a bending in the profile. Distortion is described by the curvature which is constant throughout the length of the profile and defined as the reciprocal of the arc radius. Typical profile cross-sections and typical arc shaped distortion are shown in Fig. 1.2. The profile distortion should be eliminated as it means rework expenditure, problems with bearing and bundling. Methods to minimize the distortion of long steel profiles by controlled quenching have been discussed in [Pie00, PBK⁺05, PBK⁺07, KS07, KBS05, KBS06]. There have been also experimental researches for the cooling distortion of the railway profiles. An overview of the works can be found in the theses [Hin90, Pie00], where the experimental results for the residual stresses and the deformations after quenching are presented. The distortion and residual stresses in carburized thin strips are investigated by [PCL⁺03].

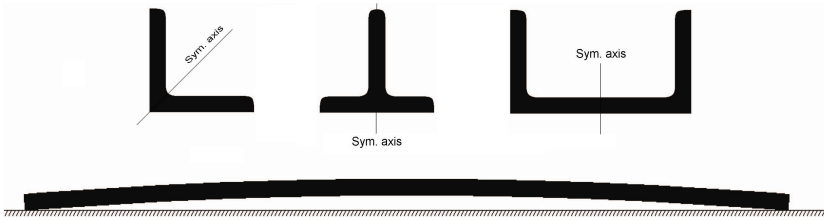


Figure 1.2: Typical distortion of an L, T or U profile after cooling

Some hot plates stacked and allowed to air-cool become warped during unstacking as seen in Fig. 1.3. The primary reason for plate buckling is the residual stresses generated during the heat treatment processes. When the top and bottom surfaces of a plate are cooled at the same cooling rate from a high initial temperature, the surface temperatures are much lower than that of the neutral plane. This produces compression in the neutral plane and tension on the surfaces. These stresses may exceed the yield limit and result in plastic deformations at high cooling rates. The residual stresses are inevitable after completion

of cooling if there are plastic deformations due to thermal and phase transition effects. However, because of the inherent symmetry, the plate may remain flat. When one surface is machined to a certain depth, the residual stresses are redistributed along the thickness, and the plate will warp up or down. For the plates that are hot rolled and then stacked hot, the cooling rates on the top and bottom surfaces are different. It is realized that there are tensile stresses on the top surface and compression stresses on the bottom surface in the length direction. The bending moment generated by the thermal stresses will act on the cross-sections. As a result, thermal stresses may lead to plate buckling.

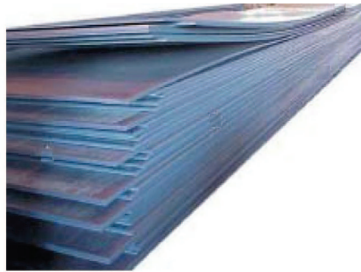


Figure 1.3: Typical distortion of plates after cooling [YM03]

A cutting saw is a long thin strip which has very hard teeth on one side. The strip material is softer than the teeth material in order to provide the necessary ductility. The desired micro-structure for the saw is to have a complete martensitic structure. The distortion of the saw which is schematically shown in Fig. 1.4 is produced up on martensitic transformation. Due to material, surface and quenching rate differences between the tooth region and strip region, martensitic transformation occurs with a time delay at strip region and this initiates the distortion.



Figure 1.4: Schematic description of cutting saw distortion

The quenching of the saw at is started with the radiation and convection in an oxygen free environment to prevent the oxidation. As the temperature drops, the convection becomes dominant since the radiation rate is proportional to the forth power of temperature. In the last stage of the cooling, the saw temperature is relatively low and the surface is hard enough to touch. Therefore, the cooling can be continued either by press-quenching, where cooling is provided by heat conduction through contact boundary, or by convection cooling. In either case the cooling must be controlled to avoid the distortion which is obvious as shown in Fig. 1.5.

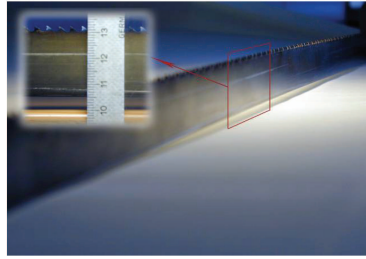


Figure 1.5: Typical distortion of steel cutting saw after cooling

The disk with a hole is similar to a CD shape, except that the the outer edge is sharp and a segment is straight as shown in Fig. 1.6. Upon uniform cooling, the central circular hole is distorted to form an oval like shape which may cause problems during the assemblage of the disk with other parts. The disk considered here is not radially symmetric because of the straight segment. Therefore, the temperature gradient and phase transformations produce a non uniform displacement field. As a result the hole is oval shaped instead of circle after the quenching. A radially symmetric disk will not have a distortion after the quenching. However, it would have high residual hoop-stresses.

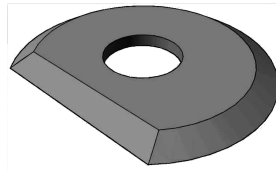


Figure 1.6: Geometry of the disk with a hole

A notched shaft is a long cylinder which has different diameters at different sections as shown in Fig. 1.7. Shafts are one of the basic components of a power train. Therefore, they need high strength, fatigue resistance, etc. which are provided by quenching. After the quenching, the shafts do not have distortion problems since their geometry is axially symmetric. However, if the quenching is uncontrolled, very high stresses and non-uniform hardness distribution occur. The high stress regions are mainly located at sharp edges and on the surface which may even cause cracks on the surface. The hardness distribution is directly related to the quenching rates which vary significantly when the quenching is uncontrolled.

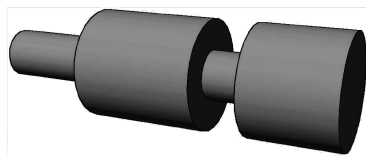


Figure 1.7: Geometry of the shaft with notches

Experiments have been performed in Bremen University, Germany on the disks and shafts. The temperature, distortion, residual stresses, and microstructure have been measured after the cooling. These results are also used in order to verify our mathematical model [BSO⁺05, BSO⁺06, BKS05].

Although metal quenching process is very beneficial, the above mentioned problems are common for the products mainly made up of aluminum and steel alloys. These problems in general occur upon quenching and originate from the high temperature gradients and phase transitions. In almost every case it is possible to resolve these problems by controlling the local quenching using a gas nozzle field or atomized sprays.

1.3 Common existing solutions

1.3.1 Press hardening

Press hardening is a modern and pollution free method in order to harden the flat products free of distortion. Quenching is performed by contact cooling between the two liquid-cooled metal dies, which prevent the distortion by a pressing force in vertical direction as shown in Fig. 1.8. The main disadvantage of this method is inconvenience of continuous production. Each quenching operation is performed separately, which diversely affect the production time and cost. Another disadvantage is that this process is limited to flat products such as plates and profiles. Moreover, if the surface of the product needs to be stretch free, then press hardening is not an applicable technique. If the quenching is performed in the forming dies without any additional external load, unlike press hardening, then the process is called plug/die quenching. However, this method does not guarantee that the work-piece remains straight after removed from the dies.

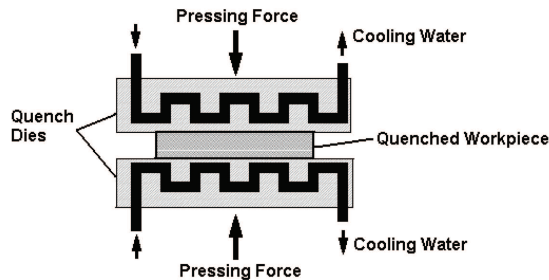


Figure 1.8: Mechanism of press hardening equipment

1.3.2 Straightening

A common method for reducing the distortion is the straightening technique, in which the metal entity is transported through a series of rollers which are arranged as shown in Fig. 1.9. The rollers plastically bend the profile in sequence several times to achieve a final straight geometry. Subsequent to such a straightening method, preferably a stress relieving procedure is applied.

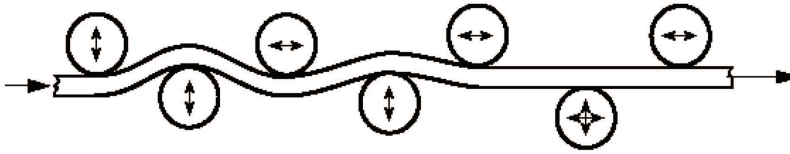


Figure 1.9: Schematic representation of a role arranging

Flame straightening is also common in welding processes as well as quenching where high temperature gradients leave stresses in the metal causing a distortion or warping. This method is an efficient and long-established technique of correcting the distorted parts. Flame straightening is based on the physical principle that metals expand when heated and contract when cooled. If the expansion is limited, compressive stresses build up, which result in plastic deformations at high temperatures. Upon cooling, since it contracts more than it could expand when heated, the additional plastic deformations cancel out the initial distortion. The choice of appropriate flame nozzles depends on the type and thickness of the material. Straightening of a plate with 3 flame nozzles is illustrated in Fig. 1.10.

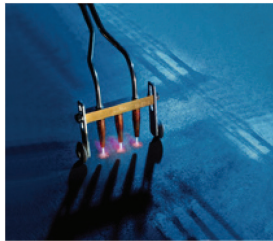


Figure 1.10: Flame straightening of a plate with 3 flame nozzles

Straightening methods can be applicable to the following products:

- Angles, I-beams and channels
- Axles
- Bars: round, hexagonal and square
- Crank Shafts
- Cylinders: shafts and tubes
- Dies
- Forklift: forks and carriages
- Molds
- Precision parts
- Plates: all shapes and sizes

- Tubes: round and square
- Weldments: aircraft and industrial

1.3.3 Stretching

Stretching by a few percent can reduce the residual stresses for some products such as plates and extrusions. A uniform plastic deformation is applied so that after the removal of external load, uniformly distributed stresses and strains remain over the entire body. Although, the warped plate can be corrected to a certain extent by the flattening and leveling processes, the flatness of the plates still may not meet the requirements of the customers. Moreover some warped plates remain unrecoverable because of the restrictions in the process and equipment capability [YM03].

1.4 Distortion engineering

The distortion controlling is one of the highest challenges in modern cost-effective production in the industry. Therefore, there have been also many scientific and industrial researches on the distortion caused by heat treatment. The 1st International Conference on Distortion Engineering was held in Bremen, Germany on 14-16. Nov. 2005. Although, the initial researches were on pure empirical investigations, with the tremendous growth of the computer technology and modeling, the realistic numerical simulations of complex problems are possible today. These recent advances have significantly enhanced the understanding of distortion mechanisms which is apparent from the recent research works.

During quenching of a metal, distortion, high residual stresses, cracking and inability of obtaining the desired micro-structure lead to defective products or service failure. The computation of the temperature evolution, cooling rates, residual stresses and distortion is indispensable to the industry. For this reason, the modeling of the cooling process has been the subject of many investigations [Yu77, HE79, Sjo84, LMDD85]. Simulation of heat treatment process provides a considerable reduction of the design time and cost with the optimum product properties. However, for the simulations nonlinear coupled partial differential equations of heat transfer, phase transformation, stress evolution must be solved simultaneously.

Numerical methods enable the calculation of the temperature, micro-structure, and displacement fields during quenching. In addition, the influence of individual parameters, which usually cannot be separated experimentally, can be analyzed. On the other hand, experiments are still essential not only to compare experimental and numerical results but also to obtain basic material data such as heat conductivity or elasticity modulus as well as heat transfer coefficients.

1.5 Summary

The motivation of the study was explained at the beginning of this chapter. It is followed by the review of the common problems encountered in the industrial

manufacturing process. Also, a short review of the known solutions of these problems was given. Finally, the chapter is concluded by some words taken from the 1st International Conference on Distortion Engineering as the importance of distortion controlling is getting more and more importance every day.

Chapter 2

Literature review

2.1 Introduction

Numerical methods are becoming more important since the computer technology is advancing continuously and the ratio of computational power to price is getting higher and higher. However, experiments are still necessary in order to obtain the material data and perform the benchmark tests of the mathematical models. Simulations are faster and cheaper to run, provide more detailed results and a better understanding of the quenching process as compared to the experiments. Mathematical modeling of the quenching process involves the solution of coupled temperature, micro-structure, and displacement fields which are the main subjects of the mechanics and metallurgy. In a quenching process simulation, the cooling conditions, which are expressed in terms of heat transfer boundary condition, are provided in order to compute the coupled temperature, micro-structure and stress/strain fields.

The couplings are of particular importance in some industrial processes such as quenching, tempering, welding, casting. Hence, there have been extensive research studies and literature on the mathematical modeling and numerical simulations of the fields as well as the coupling among them. There is a two-way coupling between each field as depicted in Fig. 2.1. The essential couplings are temperature dependency of phase transitions, the effect of latent heat on the temperature field, additional strains due to phase transition and thermal volume changes, and additional transformation induced plastic strains. The conversion of mechanical energy into heat during plastification is very small as compared to the latent heat effect. Usually, all material properties are assumed to be isotropic and function of temperature and phase fraction.

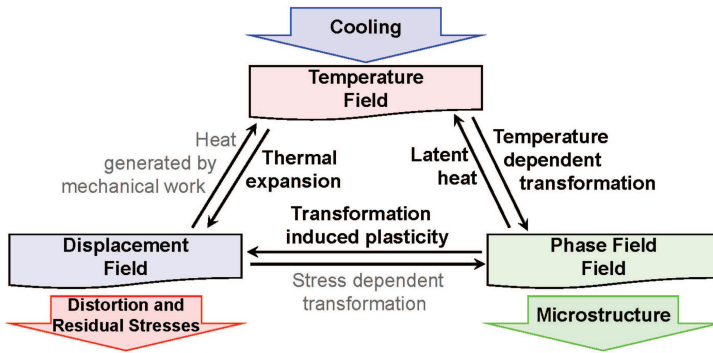


Figure 2.1: Couplings of temperature, micro-structure and displacement fields

The intensity of quenching is defined by the heat transfer coefficient on the boundaries. The recent studies [KS05b, KSP05, KS05a, Att05, PS04a, PS04b] have introduced the new quenching techniques where the local cooling is adjusted by using a gas nozzle field or by atomized sprays. The final micro-structure, residual stresses and distortion can be controlled by local adjustment of the heat transfer coefficient. In order to assess the effect of local cooling on the final micro-structure, residual stresses and distortion, a complete understanding of the mathematical model of each field is necessary. This research work is concentrated on the modeling of phase transitions and constitutive relation of thermo-elasto-plastic materials.

2.2 Phase transformation kinetics

The cooling rate of the steel has dominant effects on the final grain size and phase structures as well as on the phase morphology. For example, increasing the cooling rate leads to a higher nucleation rate of the new phase and a micro-structure with a finer grain size. If the cooling rate of the austenite exceeds a critical value, the transformation mechanism changes from diffusion-controlled to displacive. During the last decades the modeling of phase transformations of steel has been studied [SMA02, Ser03, AB81, VV87, WCY93, WCY97, Hoe96, LNMA98, JM99, FDS84, Hou90]. Most of the conducted investigations were concentrated on quenching of steel and resulting in thermal stresses, or calculation of Continuous Cooling Transformation (CCT) diagrams. The phase transformation kinetics is generally obtained from the dilatation data during a cooling process [ZMC02]. It was shown that the experimental and calculation results can be in excellent agreement.

Transformation Induced Plastic (TRIP) strains are limited to the range of a few percent. Therefore, all the TRIP models are formulated in the small strain domain. For most of the cases like quenching simulations, this assumption is acceptable. However, for the simulation of some cases like hot rolling process, the small strains must be extended to large strain domain in order to be compatible with the large plastic strains. The TRIP model presented in [Leb89] was reformulated in terms of the Lie time derivative by [BH02]. A non-additive transformation kinetics model for the cooling of low alloy steels

was presented by [LL99]. The model delivers the temperature, volume fractions (ferrite, pearlite, bainite, and martensite), residual stresses and distortion as functions of time. The martensitic phase transformation in inelastic materials was presented in [Lev98]. The bainitic transformation has the characteristics of both diffusional and displacive transformations. A conceptual framework of bainitic transformation is given in [MN02].

2.3 Constitutive relations

There are numerous references in the literature pertaining to the representation of the thermo-mechanical behavior of the elasto-plastic materials subjected to small deformations. An accurate knowledge about the true stress state and strength in metal products are crucial to be known in many applications. The manufacturing process involves the change of the mechanical state such as the evolution of residual stresses and the material properties due to work-hardening, recrystallization, phase transition, etc. The approach favored by most authors is an additive split of the strain tensor into elastic and inelastic parts. There exists a finite element-based algorithmic framework for thermo-plasticity in metals [SM92, Gla92, AS93]. The evolution of plastic strains is calculated by means of a predictor-corrector algorithm, also called return map algorithm which was established in the late eighties [Sim88a, Sim88b]. The temperature dependency of the yield stress has been taken into account.

Modeling the behavior of steel at higher temperatures requires the consideration of phase transformations, which is not considered in the above formulations. Although, the problems concerning calculation of the residual stresses from quenching without phase transformation are well understood, large discrepancies still exist regarding the calculation of transformation stresses. This can be attributed to the complex interrelation between the development of transformation stresses and phase transformation parameters [Tod99, HJ02].

2.4 Coupling phenomena

2.4.1 Dilatation due to temperature and phase changes

The inter-atomic bond energy of a metal is defined by its temperature and crystal structure state. When the stored energy increases, the length of the molecular bond also increases. Thus, the material expands or contracts due to these temperature and phase changes. This expansion or contraction can be measured by either volume or length changes, which are closely related. The volume changes can be measured for all substances of condensed matter (liquids and solid state). However, the length changes (coefficient of thermal expansion) can only be measured in the solid state and is common in engineering applications.

Metallurgical encyclopedias such as the ASM Metals Handbook [A.S79] and Metals Reference Book [Smi76] contain some high temperature thermal expansion data, but the most comprehensive source of thermal expansion data is included in Thermo-physical Properties of Matter series produced by Purdue University in the USA [Tou75]. Thermal expansion of many solids can be found in the book by [Tay98].

There are number of electronic databases available with materials property data, and many of these have coefficient of thermal expansion values. Some are available free of cost via the internet, while others are subscription-based CD-Rom services:

- CINDAS LLC <http://www.cindasdata.com>
- Matweb <http://www.matweb.com>
- Cambridge Engineering Selector <http://www.granta.co.uk>
- Metals and Materials Infobase <http://www.ili.co.uk>
- MAPP <http://www.esm-software.com/mapp>
- JAHM Software <http://jahm.com>

2.4.2 Transformation induced plastic strains (TRIP)

TRIP is described by [Mit87] as: *...Significantly increased plasticity during a phase change. Even under an externally applied load stress with the corresponding equivalent stress being small in relation to the yield stress of the material, plastic deformation occurs.* During a transformation, a micro-region may change its volume and occasionally its shape, too. To achieve the compatibility between the neighboring material and the micro-region under consideration, the misfit must be accommodated by an eigen-stress state which may vary within a grain of a polycrystalline material, but at least from grain to grain. In many cases the misfit leads to at least a plastification of the neighboring material of the micro-region, sometimes even to a plastification of the micro-regions themselves. It can be easily imagined that the development of this local eigen-stress state is influenced by an externally applied global stress state on a certain given specimen. The superposition of these two stressing or straining *mechanisms* may initiate or even promote plastification [FOTN98, FRW⁺00]. Comparison of main TRIP models with experimental results for the steel 16MND5 which composes vessels in French nuclear reactors was considered by [TCW01, TS03, CCC02]. The transformation plasticity coefficient, the kinetics as well as the dependence on the norm and the direction of the applied stress are particularly studied.

2.4.3 Dissipation of mechanical energy into heat

It is well known that the plastic deformation of metals is accompanied by the heat generation. This means that the energy balance equation that governs the temperature evolution, should involve several terms arising from thermo-mechanical coupling. The first term relates the heat production to the recoverable deformations. A second term defines heating arising from the dissipation of mechanical work during breaking of internal bonds in crystal lattice. The third term describes the stored energy of cold work, which is motivated by the re-arrangement of various defects in the structure during the plastic deformation. These effects are only important in some particular cases in the small strain regime and cannot be avoided in the most cases in finite strain regime [CB04]. In the modeling of quenching process, the heat generation due to mechanical energy dissipation is negligibly small compared to the heat transfer by cooling.

2.5 Estimation of mixture material properties

The micro-to-macro transition is defined as the averaging or homogenization to get the macroscopic overall response of heterogeneous materials with complex micro-structures [Mie03]. For homogenization methods, it is usually assumed that the internal energy per unit mass stored in the original heterogeneous and equivalent homogenized systems are to be equal. Probably the most widely-used estimate is that introduced by [Tay38]. This is obtained by assuming a uniform strain-rate field over the entire micro region and calculating the associated mean stress. The resulting estimate was proved to give an upper bound for the overall yield stress by [BH51]. A simple mechanical model was developed by [LSD99] to estimate the characteristics of fracture and yield strength of two-phase materials with fine particles. The upper and lower bounds depend on the ratio of strength and volume fraction of the constituent phases. Another averaging approach, which is a modified version of the Mori-Tanaka prediction, was suggested for two phase materials in [IK05]. The elastic properties of three-phase composites by means of closed-form analytical solutions, which do not require detailed knowledge of the micro-structure, are described in [AR05]. Another method for evaluation of the micro-mechanical properties of composite materials via incompatible multi variable FEM and homogenization theory was proposed in [SDZW01]. A micromechanical model was developed to capture the mechanical behavior of dual phase steel, which is a ferrite-martensite mixture, in [AAN03]. A method to determine the thermo-mechanical properties of composite parts was presented in [LPC⁺98]. The flow-induced fiber orientation was first calculated by numerical simulation, and the resulting orientation state was used as input in a micro-mechanical model that predicts the thermo-mechanical properties of the part.

2.6 Mathematical models for coupled field applications

2.6.1 Quenching

Quenching is a very common process in industry. Therefore, there have been many investigations on the modeling of quenching process. The mathematical model and numerical simulations of induction and flame hardening were presented in [BI98]. The couplings among the electromagnetic, thermal, stress and phase fields are considered in their model. Internal stresses are computed by an extended thermo-plasticity theory with isotropic hardening, temperature and phase fraction dependent material properties. Phase fractions are calculated by using TTT-heating and TTT-cooling diagrams in the model.

The internal micro-structures of heat treated steel bars were predicted by using a finite element method. A finite element code was developed in Fortran 77 in order to perform quenching simulations by [CTO00, GT96, GTS96]. The numerical results were compared with the experimental results for different quenching rates.

A new multiphase material model for simulating distortion and residual stresses in carburized and quenched gear steels was presented in [PCL⁺03].

Comparisons of the significant transverse quenching distortion predicted numerically showed agreement with those measured experimentally.

A model of finite thermo-plasticity with phase changes based on the concept of isomorphism of elastic ranges was presented by [DB04]. The restrictions due to the second law of thermodynamics were discussed in detail. Mass fractions were used as the internal variables to describe evolution of the phases. The described model is an extension of the thermo-plasticity theory developed by [Ber98] and rather general so that it can be applied to different materials.

2.6.2 Welding

Welding is an another common industrial process which is a coupled thermal, mechanical, and metallurgical process. Finite element modeling of such a coupled thermo-mechano-metallurgical process requires also the derivation of evolution equations for solid phase transformations as well as temperature and stress evolutions. General framework of the finite element modeling is described in detail by [RO00].

An efficient and systematic numerical implementation of the thermo-elasto-plastic constitutive equation, which accounts for the transformation plasticity in welding, was presented in [KIK05]. The thermo-elastic free energy with the temperature-dependent material constants has been employed together with the relation of the transformation plastic flow rule between the additive decomposition of the rate of deformation and the multiplicative decomposition of the deformation gradient. The tangent modulus is calculated consistent with the stress-update algorithm considering the transformation plasticity for fast convergence of the solution.

2.7 Summary

This chapter is devoted to the literature on the fundamentals of the mathematical modeling of the same or similar problems. Models on phase transformation kinetics and constitutive relations frequently addressed. Literature on the coupling phenomena such as temperature and transformation related volume changes, transformation induced plasticity and dissipation of mechanical energy are reviewed, existing mixture and homogenization models are studied. Coupling phenomena are occasionally studied in modeling of quenching and welding processes. Therefore, a short literature review on the modeling of these processes is also given in this chapter.

Chapter 3

Mathematical modeling

3.1 Temperature field

The temperature field in the body is modeled by the Fourier's law of heat conduction with two additional heat source terms. The first additional term accounts for the transformation enthalpies, and the second term includes the heat generation by mechanical energy dissipation. During the quenching processes, the heat generated due to the mechanical work is negligibly small as compared to the transformation enthalpies. Fourier's law is

$$\nabla \cdot (k \nabla \theta) + q^V = \rho c_p \dot{\theta}, \quad (3.1)$$

with boundary condition

$$\mathbf{n}^S \cdot (k \nabla \theta) + q^S = 0. \quad (3.2)$$

In Equations (3.1 and 3.2), k is the heat conductivity, q^V is the heat generation per unit volume, ρ the mass density, c_p the specific heat capacity, q^S the heat flux through the body surface due to heat convection and radiation, and \mathbf{n}^S the surface unit normal. All of the material constants are assumed to be functions of the temperature θ and the converted phase fractions f_i . The dependency of the material properties on the phase fractions f_i can be expressed by the arithmetic, geometric, harmonic, or other means.

The heat flux q^S through the boundary (outward direction is positive) and internal heat source q^V (heat generation is positive) are

$$\left. \begin{aligned} q^S &= \psi \cdot e \cdot \sigma (\theta^4 - \theta_\infty^4) + \bar{\alpha} (\theta - \theta_\infty) \\ q^V &= \chi \sigma_y \dot{\varepsilon}_{\text{eff}}^{\text{pl}} + \sum_{i=1}^N (L_i \dot{f}_i) \end{aligned} \right\}. \quad (3.3)$$

The heat flux q^S is due to thermal radiation and heat convection, where $\bar{\alpha}$ is the equivalent Heat Transfer Coefficient (HTC), θ the temperature of the body surface, θ_∞ the ambient temperature, ψ the view factor, e the emissivity, and σ the Stefan-Boltzmann constant. The internal heat source q^V is composed of latent heat generation and dissipation of mechanical energy into heat, where L_i are the latent heats of transformations, \dot{f}_i are the rates of converted phases, χ is fraction of mechanical energy converted into heat, σ_y is the yield strength, $\dot{\varepsilon}_{\text{eff}}^{\text{pl}}$ is the rate of effective plastic strain.

3.2 Micro-structure field

3.2.1 TTT charts and diffusive transformations

To predict the diffusive phase transformation, the Scheil additivity rule [Sch35] and Avrami-type equation are utilized [JM39, Kol37]. Steel has two crystal structures of the iron lattice. The solvability of carbon in iron is up to 2% in Face Centered Cubic (FCC) iron and only up to 0.2% in Body Centered Cubic (BCC) iron. The orientation of atoms in FCC iron and BCC iron are shown in Fig. 3.1.

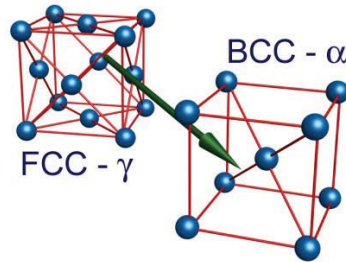


Figure 3.1: Crystallographic structure of Face centered cubic (FCC) iron and body centered cubic (BCC) iron lattice

The micro-structures in iron are austenite, ferrite, pearlite, bainite and martensite. Austenite is a solid interstitial solution of carbon in FCC iron lattice. Ferrite is solid interstitial solution of carbon in BCC iron lattice. Pearlite, which is soft and ductile, is a lamellar structure of ferrite and cementite (Fe_3C). Bainite is a mixture of ferrite and carbides, between pearlite and martensite. Martensite, which is hard and brittle, is a solid solution of carbon in tetragonally distorted BCC iron. The micro-structures depend on the cooling rate and steel characteristics, which are normally expressed by the Time-Temperature-Transformation (TTT) diagrams, (see Fig. 3.2).

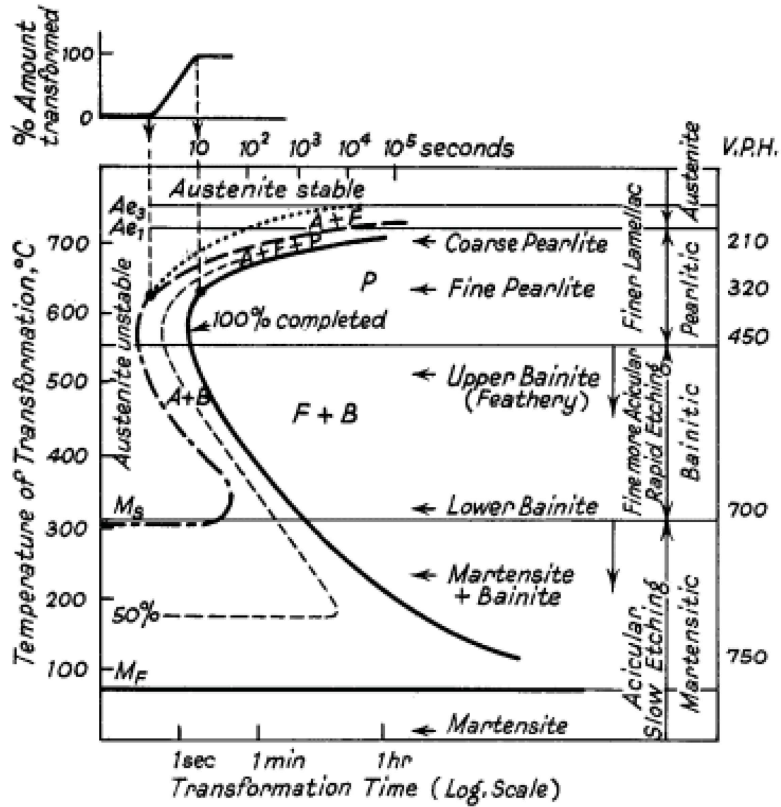


Figure 3.2: Typical TTT diagram for steel [Hoe96]

The evolution of the diffusive phase transitions is best described by TTT diagrams, which enables the metallurgist to interpret the response of steel to any specified heat-treatment. In the non-isothermal case, the phase evolutions are represented in Continuous-Cooling-Transformation (CCT) diagrams. The CCT diagrams can be derived from the Isothermal-Transformation (IT) diagram by superimposing several cooling curves and marking the transformation beginning and end. Then, the locus of the respective points defines the CCT diagram. Compared to an IT diagram the transformation curves in CCT diagrams are moved to later time and lower temperature. Pearlite forms above the nose of IT diagram and bainite forms below the nose. The formation of the new phase is described in this work by a very simple linear transformation rule,

$$df = \frac{dt}{t_E - t_S}. \quad (3.4)$$

where transformation start time t_S and transformation end time t_E are obtained from the IT diagram. The transformation limit curves in the IT diagrams contain two C-shaped curves as shown in Fig. 3.2 for a diffusional phase transition. One is for the beginning of the transformation and the other is for its end. The transformation beginning curve gives the transformation start time t_S and the other curve gives the transformation end time t_E at a constant temperature

θ . In the continuous cooling case, the transformation begins at the incubation time t_{inc} and it ends when phase fraction is unity or the temperature is out of transformation range. Incubation time t_{inc} is obtained by Scheil's sum,

$$\int_0^{t_{\text{inc}}} \frac{1}{t_S(\theta(t))} dt = 1. \quad (3.5)$$

3.2.2 Displacive transformation

The displacive transformation is a shear-dominant, time-independent, diffusion-less solid-state phase transformation. Displacive transformations occur when the temperature drops rapidly (through the interval in which nucleation could take place) to a low temperature at which the molecular mobility, i.e. diffusion, becomes too small for the formation of nuclei. The austenite changes incompletely into a distorted BCC structure, with little or no diffusion of the carbon into particles of cementite, to form martensite. This suggests that the mechanism of formation of martensitic structure is not nucleation and growth but a shearing process. The amount of martensite formed is practically independent of time and depends principally on the temperatures at which the steel is held. The temperature at which martensite begins to form is called as martensite start temperature M_S , which is progressively lowered as the carbon content of the steel increases. A detailed research work and overview of available models are given by [SGM05].

The martensitic transformation in solids provides extraordinary mechanical behaviors ranging from the super-elastic behavior of Shape Memory Alloys (SMA) to non-thermo-elastic behavior of steels with a good compromise between ductility and toughness. Martensitic transformation does not depend directly on the time but only on the temperature below the martensite start temperature M_S and is calculated in this work according to Koistinen-Marburger equation,

$$f_M = f_A \{1 - \exp(k_M(\theta - M_S))\}, \quad (3.6)$$

where f_M is the calculated martensite phase fraction, f_A is the austenite phase fraction at the beginning of martensitic transformation, and k_M is a stress-dependent transformation constant. The effects of the stress state on the transformation kinetics are discussed by [DGSS87].

The volumetric expansion associated with the formation of martensite combined with large temperature gradients and non-uniform cooling promotes high residual stresses that can induce distortion or even cracking in the quenched steels.

3.3 Displacement field

3.3.1 Plasticity formulation

An isotropic thermo-plastic material model with a temperature and phase fraction dependent constitutive relation is employed. The procedure described in the book [SH97] has been modified and adapted. The basic assumptions are as follows:

1. Total deformations are small so that the total strain tensor can be additively decomposed,

$$\mathbf{E} = \frac{1}{2} (\nabla \mathbf{u} + \nabla \mathbf{u}^T) = \mathbf{E}^{el} + \mathbf{E}^{pl} + \mathbf{E}^{tp} + \mathbf{E}^{trip}, \quad (3.7)$$

where \mathbf{u} is the displacement field, \mathbf{E}^{el} is elastic part of strain tensor, \mathbf{E}^{pl} is plastic part of strain tensor, \mathbf{E}^{trip} is for transformation induced plasticity and \mathbf{E}^{tp} is for the volume change due to temperature and phase changes. The prime over a tensor \mathbf{E}' represents its deviator.

2. The material is isotropic,

$$\mathbf{T} = \hat{\mathbf{C}}^{el} \cdot \mathbf{E}^{el} = \kappa \operatorname{tr}(\mathbf{E} - \mathbf{E}^{tp}) \mathbf{I} + 2\mu (\mathbf{E}' - \mathbf{E}^{trip} - \mathbf{E}^{pl}), \quad (3.8)$$

where \mathbf{T} is the stress tensor, $\hat{\mathbf{C}}^{el}$ elastic constitutive tensor, κ is the bulk modulus and μ is the shear modulus.

3. Plastic deformations are incompressible,

$$\operatorname{tr}(\mathbf{E}^{pl}) = 0. \quad (3.9)$$

$\operatorname{tr}(\mathbf{E})$ is the trace operator.

4. The material behavior is rate-independent.
5. The *flow criterion* is of von-Mises type,

$$\phi(\mathbf{T}', \varepsilon^{pl}, \theta, f_i) = \|\mathbf{T}'\| - \sqrt{\frac{2}{3}} \sigma_y(\varepsilon^{pl}, \theta, f_i), \quad (3.10)$$

where the yield strength σ_y is a function of hardening state variable ε^{pl} , temperature θ and phase fractions f_i .

6. An *associative flow* rule is used,

$$\dot{\mathbf{E}}^{pl} = \lambda \frac{\partial \phi}{\partial \mathbf{T}} = \lambda \frac{\mathbf{T}'}{\|\mathbf{T}'\|} = \lambda \mathbf{N}', \quad (3.11)$$

where λ is the plastic multiplier and \mathbf{N}' is the flow surface normal direction.

7. Linear *isotropic hardening* behavior is assumed for the yield strength,

$$\sigma_y(\varepsilon^{pl}, \theta, f_i) = \sigma_{yv}(\theta, f_i) + H(\theta, f_i) \varepsilon^{pl}, \quad (3.12)$$

where σ_{yv} is the yield strength at virgin state and $H(\theta, f_i) = \frac{d\sigma}{d\varepsilon^{pl}}$ is the plastic (hardening) modulus. The hardening state variable is integrated from the plastic multiplier,

$$\varepsilon^{pl} = \int \dot{\varepsilon}^{pl} dt = \sqrt{\frac{2}{3}} \int \lambda. \quad (3.13)$$

A load increment might be elastic or plastic depending on the flow criteria,

$$\phi = \begin{cases} < 0, & \text{elastic} \\ = 0, & \text{elastic or plastic} \end{cases} \quad (3.14)$$

If $\phi = 0$, then the loading is identified by *loading condition*:

$$\dot{\phi} \Big|_{\varepsilon^{pl}=\text{const.}} = \frac{\partial \phi}{\partial \mathbf{T}'} \cdot \dot{\mathbf{T}}' + \frac{\partial \phi}{\partial \theta} \dot{\theta} + \sum_{i=1}^n \frac{\partial \phi}{\partial f_i} \dot{f}_i = \begin{cases} > 0 & \text{plastic loading} \\ = 0 & \text{neutral loading} \\ < 0 & \text{elastic unloading} \end{cases} \quad (3.15)$$

A typical plastic loading increment in stress space is explained in Fig. 3.3 with a simplified 2D-sketch.

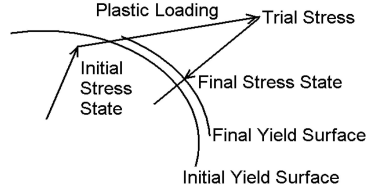


Figure 3.3: Typical plastic loading increment in stress space

For a plastic loading increment, the unknown plastic multiplier λ can be obtained from the *consistency condition*:

$$\dot{\phi} = \frac{\partial \phi}{\partial \mathbf{T}'} \cdot \dot{\mathbf{T}}' + \frac{\partial \phi}{\partial \varepsilon^{pl}} \dot{\varepsilon}^{pl} + \frac{\partial \phi}{\partial \theta} \dot{\theta} + \sum_{i=1}^n \frac{\partial \phi}{\partial f_i} \dot{f}_i = 0, \quad (3.16)$$

and flow rule. The first term in the consistency condition is computed from the elastic constitutive law,

$$\frac{\partial \phi}{\partial \mathbf{T}'} \cdot \dot{\mathbf{T}}' = \mathbf{N}' \cdot \left\{ 2\dot{\mu} \left(\mathbf{E} - \mathbf{E}^{trip} - \mathbf{E}^{pl} \right) + 2\mu \left(\dot{\mathbf{E}} - \dot{\mathbf{E}}^{trip} - \dot{\mathbf{E}}^{pl} \right) \right\}. \quad (3.17)$$

Equations (3.10, 3.11 and 3.12) are used to calculate the last three terms in the consistency condition Eq. (3.16). Finally, the unknown plastic multiplier is

$$\lambda = \frac{2\dot{\mu} \mathbf{N}' \cdot \left(\mathbf{E} - \mathbf{E}^{trip} \right) + 2\mu \mathbf{N}' \cdot \left(\dot{\mathbf{E}} - \dot{\mathbf{E}}^{trip} \right) - \sqrt{\frac{2}{3}} \left(\frac{\partial \sigma_y}{\partial \theta} \dot{\theta} + \sum_{i=1}^n \frac{\partial \sigma_y}{\partial f_i} \dot{f}_i \right)}{2\mu + \frac{2}{3}H}. \quad (3.18)$$

The relationship between the stress tensor \mathbf{T} and the elastic strain tensor \mathbf{E}^{el} is given by the elastic constitutive law. The continuum tangential elasto-plastic material operator is

$$\begin{aligned} \hat{\mathbf{C}}^{ep} &= \frac{\partial \dot{\mathbf{T}}}{\partial \dot{\mathbf{E}}^{ep}} \Big|_{T,f=\text{const.}} = \dots \\ \hat{\mathbf{C}}^{el} &- \frac{2\mu}{1 + \frac{H}{3\mu}} \mathbf{n}'_T \otimes \mathbf{n}'_T = \kappa \mathbf{I} \otimes \mathbf{I} + 2\mu \left(\hat{\mathbf{I}} - \frac{1}{3} \mathbf{I} \otimes \mathbf{I} \right) - \frac{2\mu}{1 + \frac{H}{3\mu}} \mathbf{n}'_T \otimes \mathbf{n}'_T, \end{aligned} \quad (3.19)$$

where $\hat{\mathbf{I}}$ is 4^{th} order identity tensor and $\mathbf{I} \otimes \mathbf{I}$ is the dyadic product of 2^{nd} order identity tensors. Quadratic convergence is provided for plastic deformations with the elasto-plastic tangential operator.

3.3.2 Dilatation due to temperature and phase changes

The coefficient of thermal expansion is used in general for solids for computation of thermal strains. However, this method contains a linearization and sometimes requires a conversion of the reference temperatures. An alternative method is based on the temperature dependency of the density. The strains due to temperature and phase changes are combined in

$$\mathbf{E}^{tp} = \left(\sqrt[3]{\frac{\rho_R}{\rho}} - 1 \right) \mathbf{I}, \quad (3.20)$$

where ρ_R denotes the reference density and ρ the mixture density. For an n -phase mixture, the thermal and transformation induced strain rate becomes

$$\dot{\mathbf{E}}^{tp} = \frac{d\mathbf{E}^{tp}}{d\rho} \left(\frac{\partial \rho}{\partial \theta} \dot{\theta} + \sum_{i=1}^n \frac{\partial \rho}{\partial f_i} \dot{f}_i \right). \quad (3.21)$$

3.3.3 Transformation induced plasticity (TRIP)

The transformation induced plastic strain rate is proportional to the applied stress deviator and phase transformation rates. The transformation induced plastic strain is

$$\dot{\mathbf{E}}^{trip} = -\frac{3}{2} \mathbf{T}' \sum_{i=1}^n \left\{ \Lambda_i \ln(f_i) \dot{f}_i \right\}. \quad (3.22)$$

This equation characterizes the macroscopic material behavior, which is determined by the micro-mechanical processes. Moreover, the proportionality factor depends on the fraction of the transformed phase and Greenwood Johnson coefficients Λ_i [GJ65], which must be determined experimentally. An approximation for the factor is given by

$$\Lambda_i = \frac{5}{6} \frac{(\rho_A - \rho_i)}{\rho_A \sigma_{yA}}, \quad (3.23)$$

where the relative density difference is a measure for the volume ratio of the converting phases (e.g. austenite→pearlite), and σ_{yA} the yield limit of the softer phase (mostly austenite) at transformation temperature.

3.4 Generalized mixture rule for material properties

The material properties of the mixture are calculated by using the phase fractions and material properties of constituting phases. Different mixture rules are applied for different material properties. The generalized mixture rule is given by

$$X_{\text{mix}} = \sqrt[N]{\sum_{i=0}^n f_i X_i^N}, \quad (3.24)$$

where n is the number of phases (including parent phase) and N defines the type of mixture rule (i.e., arithmetic, geometric, harmonic, or any other mixture rule). The partial derivatives with respect to temperature and phase fractions are also necessary to compute the time rate of change of the material property. So, these partial derivatives are given by

$$\left. \begin{aligned} \frac{\partial X_{\text{mix}}}{\partial T} &= \frac{X_{\text{mix}}^{1-N}}{N} \left(\sum_i f_i X_i^{N-1} \frac{dX_i}{dT} \right), & i = \text{including parent phase} \\ \frac{\partial X_{\text{mix}}}{\partial f_i} &= \frac{X_{\text{mix}}^{1-N}}{N} (X_i^N - X_A^N), & i = \text{excluding parent phase} \end{aligned} \right\}. \quad (3.25)$$

In Equations (3.23 and 3.24), X_{mix} stands for the mixture material property estimate and X_i for the material property of i^{th} phase (A: parent phase, i.e., austenite). The arithmetic mean is assumed for the density ρ , heat conductivity k , or specific heat capacity c_p with a value of $N = 1$. The harmonic mean is assumed for the flow stress σ_y with a value of $N = -1$. The geometric mean is assumed for the bulk modulus κ or the shear modulus μ with a value of $N = 0$, which cannot be used in the general equation due to singularity. Therefore, the general equation is modified for this specific case as

$$\left. \begin{aligned} X_{\text{mix}}^{\text{GM}} &= \exp \left\{ \sum_i f_i \cdot \ln(X_i) \right\}, & i = \text{including parent phase} \\ \frac{\partial X_{\text{mix}}^{\text{GM}}}{\partial T} &= X_{\text{mix}}^{\text{GM}} \cdot \sum_i \frac{f_i}{X_i} \frac{dX_i}{dT}, & i = \text{including parent phase} \\ \frac{\partial X_{\text{mix}}^{\text{GM}}}{\partial f_i} &= X_{\text{mix}}^{\text{GM}} \cdot \ln \left(\frac{X_i}{X_A} \right), & i = \text{excluding parent phase} \end{aligned} \right\}. \quad (3.26)$$

The overall behavior of the mixture material is greatly influenced by the local distribution of the phases. Consider a micro region in a two phase mixture where the phases are located as shown in Fig. 3.4. This micro-region apparently has an orthotropic behavior since the material properties such as heat conductivity and elasticity modulus are different in two mutually perpendicular directions 1 and 2. On the other hand, it is obvious that some other material properties such as heat capacity and density are direction independent properties. In this particular example, let the red color represent the phase 1 and blue color represent the phase 2. If each phase has its own heat conductivity, elasticity modulus and density, then the mixture properties can be computed depending on the phase volume fraction and direction in the following way.

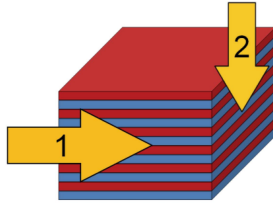


Figure 3.4: Micro regional orthotropy due to effect of phase distribution

Elasticity modulus in the 1st direction can be obtained by using the force equilibrium condition because the displacements are equal for both phases,

$$\left. \begin{aligned} F &= F_1 + F_2 = \frac{u}{L} E_1 A_1 + \frac{u}{L} E_2 A_2 = \frac{u}{L} E_{\text{mix}} A \\ E_{\text{mix}} &= f_1 E_1 + f_2 E_2 \end{aligned} \right\}. \quad (3.27)$$

The strain terms $\frac{u}{L}$ cancel out and the ratio of the phase area to total area is equal the volumetric phase fraction. Hence, for the 1st direction the elasticity modulus is obtained by arithmetic mean.

Elasticity modulus in the 2nd direction can be obtained by using the displacement equilibrium condition because this time, the forces are equal for both phases. Equation (3.28) summarizes the calculations. So for the 2nd direction the elasticity modulus is obtained by harmonic mean,

$$\left. \begin{aligned} u &= u_1 + u_2 = \frac{FL_1}{E_1A} + \frac{FL_2}{E_2A} = \frac{FL}{E_{\text{mix}}A} \\ \frac{1}{E_{\text{mix}}} &= \frac{f_1}{E_1} + \frac{f_2}{E_2}. \end{aligned} \right\}. \quad (3.28)$$

The mixture elasticity modulus obtained by arithmetic and harmonic mean define the upper and lower bounds. If the distribution of the phase fractions is not regular as in Fig. 3.4, then a geometric approximation for the mixture elasticity modulus would be a reasonable estimate which lies in between these two bounds.

Similar calculations can also be performed for heat transfer calculation in order to estimate the heat conductivities in the 1st and 2nd directions. In the 1st direction the heat flux equilibrium condition is used since the temperature difference is same for both phases,

$$\left. \begin{aligned} q &= q_1 + q_2 = \frac{\Delta\theta}{L} K_1 A_1 + \frac{\Delta\theta}{L} K_2 A_2 = \frac{\Delta\theta}{L} K_{\text{mix}} A \\ K_{\text{mix}} &= f_1 K_1 + f_2 K_2. \end{aligned} \right\}. \quad (3.29)$$

The temperature gradient terms $\frac{\Delta\theta}{L}$ cancel out and area ratios are equal to phase fractions. It is clear that in the 1st direction, the heat conductivity is obtained by arithmetic mean.

In the 2nd direction the Temperature equilibrium condition is used since the flux is same through both phases

$$\left. \begin{aligned} \Delta\theta &= \Delta\theta_1 + \Delta\theta_2 = \frac{qL_1}{K_1A} + \frac{qL_2}{K_2A} = \frac{qL}{K_{\text{mix}}A} \\ \frac{1}{K_{\text{mix}}} &= \frac{f_1}{K_1} + \frac{f_2}{K_2}. \end{aligned} \right\}. \quad (3.30)$$

Heat flux q and area A cancel out in Eq. (3.30), the ratio of the phase length to total length is equal to the phase fraction. Hence, in the 2nd direction the heat conductivity is obtained by harmonic mean. The heat conductivities in these two directions define the upper and lower bounds for the mixture conductivity. If the distributions of the phase fractions are not regular as in Fig. 3.4, then a geometric approximation would be a reasonable estimate which lies in between these bounds.

On the other hand, some other material properties such as heat capacity and density are direction-independent. One can easily prove this for the density by writing the total mass in the volume as

$$\left. \begin{aligned} m &= m_1 + m_2 = \rho_1 V_1 + \rho_2 V_2 = \rho_{\text{mix}} V \\ \rho_{\text{mix}} &= f_1 \rho_1 + f_2 \rho_2. \end{aligned} \right\}. \quad (3.31)$$

3.5 Description of the distortion

The definition of distortion should be a scalar value representing the deformation which is critical for the quenching process. A uniform deformation field

is usually not detrimental whereas a deflection or non-uniform radial displacements might be quite detrimental. In this sense, the proper description of the profile distortion can be explained by the deflection but the deflection is length dependent. A better description for the distortion is the curvature of profile. If the profile is bent to a circular arc shape then the reciprocal of the radius gives the curvature (independent of profile length) as described in Fig. 3.5. Fortunately, the curvature is a direct output of the finite element simulations of profiles.

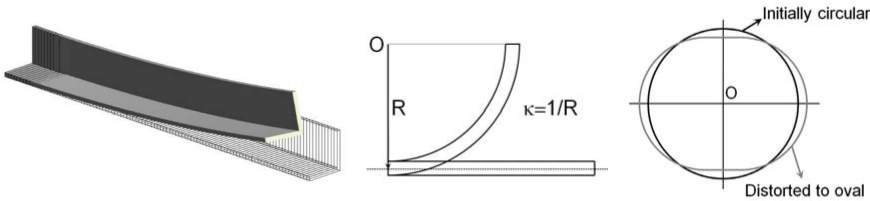


Figure 3.5: Deflection of an L profile, definition of the distortion by curvature, and central hole of the cutting disk before and after the cooling

The distortion of the steel disc with a hole is described by the radial displacement of the hole. The hole is initially circular but after the quenching, it becomes oval as shown in Fig. 3.5. A scalar value should be defined that expresses the ovalisation of the hole. From the finite element solution, the final nodal coordinates of the nodes that are located on the hole are known. The radius of the best circle fit is computed. The distance of the nodal points to the circle is then calculated. The standard deviation of these distance values is a measure for distortion. If the standard deviation is zero it means there is no distortion and hole is circular. As the standard deviation gets larger the hole becomes more oval.

3.6 Summary

The mathematical model for the quenching process was introduced in this chapter. Transient temperature field, solid state phase transitions and displacement field models are separately discussed but coupling terms are addressed during the explanations. Different material properties of the mixture was estimated by using different mixture rules. So, a generalized mixture rule also introduced. Finally, the descriptions of the distortion were stated for the geometries considered in this study.

Chapter 4

Finite element modeling

4.1 Reasons to choose finite element method

In this chapter the finite element formulation of the described mathematical model and its implementation will be discussed. The Partial Differential Equations (PDE) that have been already introduced in chapter 3 for describing the heat flow and deformation processes are too complex, coupled and highly non-linear to be solved analytically. Therefore, the finite element method, which is the most common and powerful method to handle such engineering problems, is chosen to obtain the approximate solutions. The material body of concern is approximated by an assemblage of finite elements, over which the fields are interpolated from the values of nodal field variables. Once the element formulation is implemented to calculate the element matrices, the system matrices can be assembled by using the element connectivity data, and the unknown field variables can be solved from the system of linear algebraic equations. In the following sections of this chapter, details of the element formulations for computing the heat transfer, phase transitions and mechanical processes will be discussed.

4.2 Solution algorithm

A time integration scheme that involves equilibrium iterations is applied to solve the described coupled field problem. In each time step, first the temperature field is solved iteratively, then the phase transitions are computed, and finally displacement field is computed iteratively. The phase transitions are calculated by using the current temperature and previous time step data. In the computation of displacement field, the current temperature, phase fractions and their rates are used. After the convergence of displacement field, the next time step is started. This solution algorithm is summarized as:

START

<p>Preprocess (set input parameters)</p>	$\left\{ \begin{array}{l} \text{Material properties} \\ \text{FE mesh and boundary conditions} \\ \text{Initial database} \end{array} \right.$
<p>Solve (solve coupled fields at each time step)</p>	$\left\{ \begin{array}{l} \text{Iteratively solve temperature field} \\ \text{Calculate phase fractions} \\ \text{Iteratively solve displacement field} \\ \text{Save integration point variables to database} \end{array} \right.$
<p>Postprocess (analyze output)</p>	$\left\{ \begin{array}{l} \text{Point tracking (for a time range)} \\ \text{Results through a line between two points (at a time)} \\ \text{Contour results (at a time)} \end{array} \right.$

END

4.3 Temperature field formulation

4.3.1 Preliminaries

The heat conduction equation has to be put in a more convenient form before using it in the finite element formulations. For an arbitrarily chosen temperature distribution $\tilde{\theta}$ (with $\tilde{\theta} = 0$ on the boundary with prescribed temperature), the heat conduction equation can be expressed in the integral form. For the solution θ , the equation

$$\int_V \left[\nabla \cdot (k \nabla \theta) + q^V - \rho c_p \dot{\theta} \right] \tilde{\theta} dV = 0 \quad (4.1)$$

is apparently satisfied because the bracket in the integral is zero. This method is named virtual temperature method and stated in the following way: *the principle of virtual temperatures is an equation of heat flow equilibrium: for θ to be the solution of the temperature in the body under consideration, must hold for arbitrary virtual (continuous) temperature distributions that are zero on the temperature described boundary.* in [Bat96].

By using the property of the divergence operator,

$$\nabla \cdot (\tilde{\theta} k \nabla \theta) = (k \nabla \theta) \cdot \nabla \tilde{\theta} + \nabla \cdot (k \nabla \theta) \tilde{\theta}, \quad (4.2)$$

Eq. (4.1) can be written as

$$\int_V \left[\nabla \cdot (\tilde{\theta} k \nabla \theta) - (k \nabla \theta) \cdot \nabla \tilde{\theta} + q^V \tilde{\theta} - \rho c_p \dot{\theta} \tilde{\theta} \right] dV = 0, \quad (4.3)$$

the first term of which is suitable for the application of the divergence theorem. After applying the divergence theorem and the imposition of the boundary conditions, the first term becomes

$$\int_V \left[\nabla \cdot (\tilde{\theta} k \nabla \theta) \right] dV = \int_S \left[\mathbf{n}^S \cdot (\tilde{\theta} k \nabla \theta) \right] dS = - \int_S \left[q^S \tilde{\theta} \right] dS. \quad (4.4)$$

After the replacement of the first term in Eq. (4.3) by Eq. (4.4) and the imposition of the boundary conditions and some rearrangement,

$$\int_V [\nabla \tilde{\theta} \cdot (k \nabla \theta)] dV + \int_S [\tilde{\theta} \bar{\alpha} \theta] dS + \int_V [\tilde{\theta} \rho c_p \dot{\theta}] dV = \dots \\ \int_V [\tilde{\theta} q^V] dV + \int_S [\tilde{\theta} \bar{\alpha} \theta_\infty] dS, \quad (4.5)$$

which is almost ready to be used in the finite element formulations. Eq. (4.5) is satisfied over the whole domain and sub-domains (i.e. each element) for an arbitrary temperature distribution $\tilde{\theta}$.

As it has been already stated before, the complete body under consideration can be approximated as an assemblage of finite elements. Over each element, the temperature field is interpolated from the nodal temperatures. So, for the e^{th} element, the temperature field and its gradient are

$$\left. \begin{aligned} \theta_e &= \mathbf{N}_e^T \Theta_e \\ \frac{\partial \theta_e}{\partial x_i} &= \frac{\partial \mathbf{N}_e^T}{\partial x_i} \Theta_e = \mathbf{H}_e \Theta_e \end{aligned} \right\}, \quad (4.6)$$

where the subscript e denotes the e^{th} element and Θ_e is the vector of all nodal point temperatures of the e^{th} element with n -nodes

$$\Theta_e = [\theta_1 \quad \theta_2 \quad \dots \quad \theta_n]^T. \quad (4.7)$$

The operators \mathbf{N}_e and $\mathbf{H}_e = [\frac{\partial \mathbf{N}_e}{\partial x} \quad \frac{\partial \mathbf{N}_e}{\partial y}]^T$ are the element temperature and temperature-gradient interpolation operators, respectively. With the help of these descriptions, the integral equation can be put in the following form

$$\sum_e \int_{V_e} [\tilde{\Theta}_e^T \mathbf{H}_e^T k \mathbf{H}_e \Theta_e] dV + \sum_e \int_{S_e} [\tilde{\Theta}_e^T \mathbf{N}_e^S \bar{\alpha} (\mathbf{N}_e^S)^T \Theta_e] dS + \dots \\ \sum_e \int_{V_e} [\tilde{\Theta}_e^T \mathbf{N}_e \rho c_p \mathbf{N}_e^T \dot{\Theta}_e] dV = \dots \\ \sum_e \int_{V_e} [\tilde{\Theta}_e^T \mathbf{N}_e q^V] dV + \sum_e \int_{S_e} [\tilde{\Theta}_e^T \mathbf{N}_e^S \bar{\alpha} \theta_\infty] dS, \quad (4.8)$$

where \mathbf{N}_e^S is the interpolation functions on the element surface and $\tilde{\Theta}_e$ is an arbitrary vector of virtual nodal temperatures that is common on both sides, so it cancel outs, and after the assemblage, a linear system of equation is obtained with unknown nodal temperatures. Newton-Raphson iterations are used for the solution at current time $t + \Delta t$. The nodal temperature vector and its derivative (Euler backward approximation) for the current i^{th} iteration are

$$\left. \begin{aligned} {}^{t+\Delta t}_i \Theta &= {}^{t+\Delta t}_{i-1} \Theta + \Delta \Theta \\ {}^{t+\Delta t}_i \dot{\Theta} &= \frac{{}^{t+\Delta t}_{i-1} \Theta + \Delta \Theta - {}^t \Theta}{\Delta t} \end{aligned} \right\}. \quad (4.9)$$

When these two terms are inserted in the final form of the integral equation

(Eq. (4.8)), we get

$$\left\{ \sum_e \int_{V_e} [\mathbf{H}_e^T \ ^{t+\Delta t} k \ \mathbf{H}_e] dV + \sum_e \int_{S_e} [\mathbf{N}_e \ ^{t+\Delta t} \bar{\alpha} (\mathbf{N}_e^S)^T] dS \right\} ({}^{t+\Delta t} \boldsymbol{\Theta} + \Delta \boldsymbol{\Theta}) + \dots$$

$$\left\{ \sum_e \int_{V_e} [\mathbf{N}_e \ ^{t+\Delta t} \rho \ ^{t+\Delta t} c_p \ \mathbf{N}_e^T] dV \right\} \left(\frac{{}^{t+\Delta t} \boldsymbol{\Theta} + \Delta \boldsymbol{\Theta} - {}^t \boldsymbol{\Theta}}{\Delta t} \right) = \dots$$

$$\sum_e \int_{V_e} [\mathbf{N}_e \ ^{t+\Delta t} q^V] dV + \sum_e \int_{S_e} [\mathbf{N}_e \ ^{t+\Delta t} \bar{\alpha} \theta_\infty] dS. \quad (4.10)$$

Now the nodal temperature increment is the only unknown vector and it is kept on the left-hand-side, all other terms are moved to right-hand-side,

$$\left\{ \sum_e \int_{V_e} [\mathbf{H}_e^T \ ^{t+\Delta t} k \ \mathbf{H}_e] dV + \sum_e \int_{S_e} [\mathbf{N}_e^S \ ^{t+\Delta t} \bar{\alpha} (\mathbf{N}_e^S)^T] dS \right\} (\Delta \boldsymbol{\Theta}) + \dots$$

$$\left\{ \sum_e \int_{V_e} [\mathbf{N}_e \ ^{t+\Delta t} \rho \ ^{t+\Delta t} c_p \ \mathbf{N}_e^T] dV \right\} \left(\frac{\Delta \boldsymbol{\Theta}}{\Delta t} \right) = \dots$$

$$\sum_e \int_{V_e} [\mathbf{N}_e \ ^{t+\Delta t} q^V] dV + \sum_e \int_{S^{(m)}} [\mathbf{N}_e^S \ ^{t+\Delta t} \bar{\alpha} \theta_\infty] dS - \dots$$

$$\left\{ \sum_e \int_{V_e} [\mathbf{H}_e^T \ ^{t+\Delta t} k \ \mathbf{H}_e] dV + \sum_e \int_{S_e} [\mathbf{N}_e^S \ ^{t+\Delta t} \bar{\alpha} (\mathbf{N}_e^S)^T] dS \right\} ({}^{t+\Delta t} \boldsymbol{\Theta}) - \dots$$

$$\left\{ \sum_e \int_{V_e} [\mathbf{N}_e \ ^{t+\Delta t} \rho \ ^{t+\Delta t} c_p \ \mathbf{N}_e^T] dV \right\} \left(\frac{{}^{t+\Delta t} \boldsymbol{\Theta} - {}^t \boldsymbol{\Theta}}{\Delta t} \right), \quad (4.11)$$

or if the matrices are given specific names,

$$\left\{ {}^{t+\Delta t} \mathbf{K}^k + {}^{t+\Delta t} \mathbf{K}^c + \frac{1}{\Delta t} \ ^{t+\Delta t} \mathbf{C} \right\} (\Delta \boldsymbol{\Theta}) = {}^{t+\Delta t} \mathbf{Q} + {}^{t+\Delta t} \mathbf{Q}^c - {}^{t+\Delta t} \mathbf{Q}^k - {}^{t+\Delta t} \mathbf{Q}^{cp}. \quad (4.12)$$

These global matrices are assembled from the numerically integrated element matrices by using the element connectivity. The finite element matrices used in nonlinear heat transfer analysis are:

$$\left. \begin{aligned} {}^{t+\Delta t} \mathbf{K}^k &= \sum_e \int_{V_e} [\mathbf{H}_e^T \ ^{t+\Delta t} k \ \mathbf{H}_e] dV \\ {}^{t+\Delta t} \mathbf{K}^c &= \sum_e \int_{S_e} [\mathbf{N}_e^S \ ^{t+\Delta t} \bar{\alpha} (\mathbf{N}_e^S)^T] dS \\ {}^{t+\Delta t} \mathbf{C} &= \sum_e \int_{V_e} [\mathbf{N}_e \ ^{t+\Delta t} \rho \ ^{t+\Delta t} c_p \ \mathbf{N}_e^T] dV \\ {}^{t+\Delta t} \mathbf{Q} &= \sum_e \int_{V_e} [\mathbf{N}_e \ ^{t+\Delta t} q^V] dV \\ {}^{t+\Delta t} \mathbf{Q}^c &= \sum_e \int_{S_e} [\mathbf{N}_e \ ^{t+\Delta t} \bar{\alpha} \theta_\infty] dS \\ {}^{t+\Delta t} \mathbf{Q}^k &= \left\{ \sum_e \int_{V_e} [\mathbf{H}_e^T \ ^{t+\Delta t} k \ \mathbf{H}_e] dV \right\} ({}^{t+\Delta t} \boldsymbol{\Theta}) \\ {}^{t+\Delta t} \mathbf{Q}^{cp} &= \left\{ \sum_e \int_{V_e} [\mathbf{N}_e \ ^{t+\Delta t} \rho \ ^{t+\Delta t} c_p \ \mathbf{N}_e^T] dV \right\} \left(\frac{{}^{t+\Delta t} \boldsymbol{\Theta} - {}^t \boldsymbol{\Theta}}{\Delta t} \right) \end{aligned} \right\}. \quad (4.13)$$

The integrals are calculated numerically by Gauss-Quadrature rule. Three points are selected in each coordinate axis direction. Therefore, 2D elements have nine integration points in the area and three integration points on each side. 3D elements have twenty-seven integration points in the volume and nine integration points on each face.

4.3.2 Two-dimensional elements

It is assumed that the temperature and cooling conditions are constant in the axial direction of the long profiles. This assumption leads to all of the other fields also to be constant. Consequently, the mathematical model of the profile problems reduces from three dimension to two dimension with much fewer degrees of freedoms. This reduction of the dimension, simplifies not only the visualization of the fields, but also the determination of optimal cooling conditions.

In finite element implementations, usually plane stress, plane strain and axis symmetric elements are combined in a single routine. In this work, an additional *beam cross-section element* type is introduced in addition to these three elements. The finite element calculations for these four types of elements are very similar to each others. There are only minor differences while performing the numerical integrations to form the element matrices and vectors. These minor differences do not change the general structure of the formulation. Only, the volume dV and area dA terms in the integrals differ from each other, which is obvious from the 3D geometry described by typical 2D element geometry. Quadrilateral parent element and its typical mapping to the global coordinates are shown in Fig. 4.1 together with element node numbering.

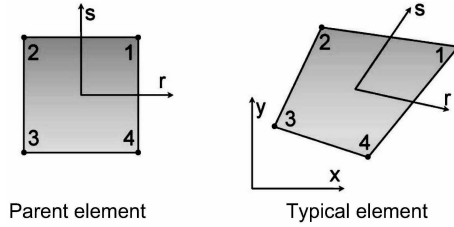


Figure 4.1: Quadrilateral parent element and its typical mapping to global coordinates

In 2D-finite elements, the infinitesimal volume for the volume integrals is obtained by multiplying the area with the thickness in the perpendicular direction,

$$dV = \ell |\mathbf{J}| dr ds. \quad (4.14)$$

Similarly, the infinitesimal area for the surface integrals is

$$dA = \begin{cases} \ell |\mathbf{J}^{(2)}| ds & \text{on faces 1\&2} \\ \ell |\mathbf{J}^{(1)}| dr & \text{on faces 3\&4} \end{cases}, \quad (4.15)$$

where $\mathbf{J}^{(i)}$ represents the i^{th} column vector of the Jacobian matrix, $\mathbf{J}^{(1)}dr$ and $\mathbf{J}^{(2)}ds$ are the mapping of the infinitesimal vectors dr and ds to global coordinates, and t is the thickness in the perpendicular direction. For plane strain, plane stress, beam cross-section and axis symmetric element formulations, the values of thickness ℓ are:

$$\ell = \begin{cases} 1 & \text{unit length} & \text{if plane strain or beam cross-section} \\ \ell & \text{real thickness} & \text{if plane stress} \\ x & \text{the radius} & \text{if axis symmetric (1 rad is considered)} \end{cases}. \quad (4.16)$$

The faces define the four boundaries of the element. According to node numbering in Fig. 4.1, the left and right sides are called faces 1-2, and top and bottom sides are called faces 3-4, respectively.

The same interpolation functions are used to map the element geometry and temperature field for isoparametric elements. Hence, the global coordinates and temperature in terms of nodal coordinates and nodal temperatures at a given local coordinates (r, s) are interpolated by

$$\left. \begin{aligned} x(r, s) &= \mathbf{N}^T \mathbf{X} \\ y(r, s) &= \mathbf{N}^T \mathbf{Y} \end{aligned} \right\} \quad \text{and} \quad \theta(r, s) = \mathbf{N}^T \boldsymbol{\Theta}, \quad (4.17)$$

where the vectors, \mathbf{X} and \mathbf{Y} , are the coordinates of the nodes. Vector $\boldsymbol{\Theta}$ is the nodal temperatures and \mathbf{N} is the interpolation functions,

$$\mathbf{N} = \frac{1}{4} \begin{bmatrix} (1+r)(1+s) \\ (1-r)(1+s) \\ (1-r)(1-s) \\ (1+r)(1-s) \end{bmatrix}. \quad (4.18)$$

The calculations of element matrices require the derivatives of the temperature with respect to global coordinates. The gradient operator \mathbf{H} , which performs this derivative operation, can be obtained by the chain rule in the following manner,

$$\begin{bmatrix} \frac{\partial}{\partial r} \\ \frac{\partial}{\partial s} \end{bmatrix} = \begin{bmatrix} \frac{\partial x}{\partial r} & \frac{\partial y}{\partial r} \\ \frac{\partial x}{\partial s} & \frac{\partial y}{\partial s} \end{bmatrix} \begin{bmatrix} \frac{\partial}{\partial x} \\ \frac{\partial}{\partial y} \end{bmatrix} = \mathbf{J}^T \begin{bmatrix} \frac{\partial}{\partial x} \\ \frac{\partial}{\partial y} \end{bmatrix}. \quad (4.19)$$

From Eq. (4.19), the Jacobian can be calculated as

$$\mathbf{J} = \begin{bmatrix} \frac{\partial x}{\partial r} & \frac{\partial x}{\partial s} \\ \frac{\partial y}{\partial r} & \frac{\partial y}{\partial s} \end{bmatrix} = \begin{bmatrix} \frac{\partial \mathbf{N}^T \mathbf{X}}{\partial r} & \frac{\partial \mathbf{N}^T \mathbf{X}}{\partial s} \\ \frac{\partial \mathbf{N}^T \mathbf{Y}}{\partial r} & \frac{\partial \mathbf{N}^T \mathbf{Y}}{\partial s} \end{bmatrix}, \quad \text{or} \quad \mathbf{J}^T = \left[\frac{\partial \mathbf{N}}{\partial r} \quad \frac{\partial \mathbf{N}}{\partial s} \right]^T [\mathbf{X} \quad \mathbf{Y}]. \quad (4.20)$$

The derivatives of the interpolation functions with respect to local coordinates are required for calculation of the Jacobian,

$$\frac{\partial \mathbf{N}}{\partial r} = \frac{1}{4} \begin{bmatrix} +(1+s) \\ -(1+s) \\ -(1-s) \\ +(1-s) \end{bmatrix}, \quad \frac{\partial \mathbf{N}}{\partial s} = \frac{1}{4} \begin{bmatrix} +(1+r) \\ +(1-r) \\ -(1-r) \\ -(1+r) \end{bmatrix}. \quad (4.21)$$

The derivative operator \mathbf{H} is of size 2×4 by definition and given by

$$\mathbf{H} = \begin{bmatrix} \frac{\partial}{\partial x} \\ \frac{\partial}{\partial y} \end{bmatrix} \mathbf{N}^T = \mathbf{J}^{-T} \begin{bmatrix} \frac{\partial}{\partial r} \\ \frac{\partial}{\partial s} \end{bmatrix} \mathbf{N}^T. \quad (4.22)$$

4.3.3 Three-dimensional element

For the modeling of the heat transfer in 3D geometries, an 8-node isoparametric brick element is introduced. The 3D element formulation is relatively simple as compared to the general 2D element formulation which is described in the previous section. Typical 3D parent element geometry and its node numbering are shown in Fig. 4.2.

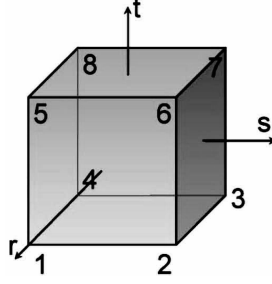


Figure 4.2: 3D parent element and its node numbering for temperature field calculations

The infinitesimal volume for volume integral computations is

$$dV = |\mathbf{J}| dr ds dt. \quad (4.23)$$

The infinitesimal area for surface integral computations is

$$dA = \begin{cases} \left| \mathbf{J}^{(2)} \times \mathbf{J}^{(3)} \right| ds dt & \text{on face 1\&2} \\ \left| \mathbf{J}^{(1)} \times \mathbf{J}^{(3)} \right| dr dt & \text{on face 3\&4} \\ \left| \mathbf{J}^{(1)} \times \mathbf{J}^{(2)} \right| dr ds & \text{on face 5\&6} \end{cases}, \quad (4.24)$$

where $\mathbf{J}^{(i)}$ represents the i^{th} column vector of the Jacobian matrix, $\mathbf{J}^{(1)} dr$, $\mathbf{J}^{(2)} ds$ and $\mathbf{J}^{(3)} dt$ are the mapping of infinitesimal vectors dr , ds and dt to global coordinates, respectively. So, the cross product simply gives the infinitesimal area dA .

The faces define the six boundary of the element. According to node numbering in Fig. 4.2, the front and back faces are called faces 1-2, left and right faces are called faces 3-4, and top and bottom faces are called faces 5-6, all respectively.

The same interpolation functions are used to map the element geometry and temperature field (i.e., isoparametric element formulation). Hence, for a given local coordinates (r, s, t) , the global coordinates (x, y, z) and temperature θ are

$$\left. \begin{aligned} x(r, s, t) &= \mathbf{N}^T \mathbf{X} \\ y(r, s, t) &= \mathbf{N}^T \mathbf{Y} \\ z(r, s, t) &= \mathbf{N}^T \mathbf{Z} \end{aligned} \right\} \text{ and } \theta(r, s, t) = \mathbf{N}^T \Theta, \quad (4.25)$$

where the vectors, \mathbf{X} , \mathbf{Y} and \mathbf{Z} , are the coordinates of the nodes, vector Θ is the nodal temperatures and \mathbf{N} is the interpolation functions,

$$\mathbf{N} = \frac{1}{8} \begin{bmatrix} (1+r)(1-s)(1-t) \\ (1+r)(1+s)(1-t) \\ (1-r)(1+s)(1-t) \\ (1-r)(1-s)(1-t) \\ (1+r)(1-s)(1+t) \\ (1+r)(1+s)(1+t) \\ (1-r)(1+s)(1+t) \\ (1-r)(1-s)(1+t) \end{bmatrix}. \quad (4.26)$$

The calculations of element matrices require the derivatives of temperature with respect to global coordinates. The operator \mathbf{H} performs this operation.

The chain rule can be applied to obtain the derivative operator in the following manner

$$\begin{bmatrix} \frac{\partial}{\partial r} \\ \frac{\partial}{\partial s} \\ \frac{\partial}{\partial t} \end{bmatrix} = \begin{bmatrix} \frac{\partial x}{\partial r} & \frac{\partial y}{\partial r} & \frac{\partial z}{\partial r} \\ \frac{\partial x}{\partial s} & \frac{\partial y}{\partial s} & \frac{\partial z}{\partial s} \\ \frac{\partial x}{\partial t} & \frac{\partial y}{\partial t} & \frac{\partial z}{\partial t} \end{bmatrix} \begin{bmatrix} \frac{\partial}{\partial x} \\ \frac{\partial}{\partial y} \\ \frac{\partial}{\partial z} \end{bmatrix} = \mathbf{J}^T \begin{bmatrix} \frac{\partial}{\partial x} \\ \frac{\partial}{\partial y} \\ \frac{\partial}{\partial z} \end{bmatrix}. \quad (4.27)$$

From Eq. (4.27), the Jacobian is obtained as

$$\left. \begin{aligned} \mathbf{J} &= \begin{bmatrix} \frac{\partial x}{\partial r} & \frac{\partial x}{\partial s} & \frac{\partial x}{\partial t} \\ \frac{\partial y}{\partial r} & \frac{\partial y}{\partial s} & \frac{\partial y}{\partial t} \\ \frac{\partial z}{\partial r} & \frac{\partial z}{\partial s} & \frac{\partial z}{\partial t} \end{bmatrix} = \begin{bmatrix} \frac{\partial \mathbf{N}^T}{\partial r} \mathbf{X} & \frac{\partial \mathbf{N}^T}{\partial s} \mathbf{X} & \frac{\partial \mathbf{N}^T}{\partial t} \mathbf{X} \\ \frac{\partial \mathbf{N}^T}{\partial r} \mathbf{Y} & \frac{\partial \mathbf{N}^T}{\partial s} \mathbf{Y} & \frac{\partial \mathbf{N}^T}{\partial t} \mathbf{Y} \\ \frac{\partial \mathbf{N}^T}{\partial r} \mathbf{Z} & \frac{\partial \mathbf{N}^T}{\partial s} \mathbf{Z} & \frac{\partial \mathbf{N}^T}{\partial t} \mathbf{Z} \end{bmatrix} \\ \mathbf{J}^T &= \begin{bmatrix} \frac{\partial \mathbf{N}}{\partial r} & \frac{\partial \mathbf{N}}{\partial s} & \frac{\partial \mathbf{N}}{\partial t} \end{bmatrix}^T \begin{bmatrix} \mathbf{X} & \mathbf{Y} & \mathbf{Z} \end{bmatrix} \end{aligned} \right\}. \quad (4.28)$$

The derivatives with respect to local coordinates are required for the calculation the Jacobian,

$$\frac{\partial \mathbf{N}}{\partial r} = \frac{1}{8} \begin{bmatrix} +(1-s)(1-t) \\ +(1+s)(1-t) \\ -(1+s)(1-t) \\ -(1-s)(1-t) \\ +(1-s)(1+t) \\ +(1+s)(1+t) \\ -(1+s)(1+t) \\ -(1-s)(1+t) \end{bmatrix}, \quad \frac{\partial \mathbf{N}}{\partial s} = \frac{1}{8} \begin{bmatrix} -(1+r)(1-t) \\ +(1+r)(1-t) \\ +(1-r)(1-t) \\ -(1-r)(1-t) \\ -(1+r)(1+t) \\ +(1+r)(1+t) \\ +(1-r)(1+t) \\ -(1-r)(1+t) \end{bmatrix}, \quad \frac{\partial \mathbf{N}}{\partial t} = \frac{1}{8} \begin{bmatrix} -(1+r)(1-s) \\ -(1+r)(1+s) \\ -(1-r)(1+s) \\ -(1-r)(1-s) \\ +(1+r)(1-s) \\ +(1+r)(1+s) \\ +(1-r)(1+s) \\ +(1-r)(1-s) \end{bmatrix}. \quad (4.29)$$

The derivatives operator, whose size is 3×8 , is by definition

$$\mathbf{H} = \begin{bmatrix} \frac{\partial}{\partial x} \\ \frac{\partial}{\partial y} \\ \frac{\partial}{\partial z} \end{bmatrix} \mathbf{N}^T = \mathbf{J}^{-T} \begin{bmatrix} \frac{\partial}{\partial r} \\ \frac{\partial}{\partial s} \\ \frac{\partial}{\partial t} \end{bmatrix} \mathbf{N}^T. \quad (4.30)$$

4.4 Phase field formulation

4.4.1 Computation of diffusional phase fractions

The isothermal transformation (IT) diagrams are used to describe the phase transformation for an arbitrary cooling curve by using Scheil's additivity rule. The TTT chart data is provided numerically in an array form for the implemented algorithm,

$$\mathbf{TTT} = \begin{bmatrix} \theta & t_S & t_E \\ \vdots & \vdots & \vdots \end{bmatrix}. \quad (4.31)$$

If temperature is out of the transition range (i.e., $\theta > \theta_N$ or $\theta < \theta_1$) then the transformation start and end times are $t_S = t_E = \infty$. At an integration point, the current temperature ${}^{t+\Delta t}\theta$, last temperature increment $\Delta\theta = {}^{t+\Delta t}\theta - {}^t\theta$ and global time increment Δt are known. Therefore, Scheil's sum can be computed. If the diffusive phase fraction is less than one, then the increment for the Scheil's sum [Sch35] is computed by

$$\Delta S = \frac{\Delta t}{t_S ({}^{t+\Delta t}\theta - \frac{1}{2}\Delta\theta)}. \quad (4.32)$$

If the Scheil's sum reaches one (i.e., ${}^tS < 1$ and ${}^tS + \Delta S > 1$), then only a fraction of temperature increment $\Delta\theta$ causes the phase transition. If the incubation is already completed, the complete temperature $\Delta\theta$ increment causes the transition. Hence, the increment of the diffusive phase fraction is simply

$$\Delta f = \frac{\Delta t}{t_E ({}^{t+\Delta t}\theta - \frac{1}{2}\Delta\theta) - t_S ({}^{t+\Delta t}\theta - \frac{1}{2}\Delta\theta)} \quad (4.33)$$

The Scheil's sum algorithm is schematically illustrated in Fig. 4.3 for a typical time step. The cooling curve is shown on the left side and on the right side is the TTT-diagram.

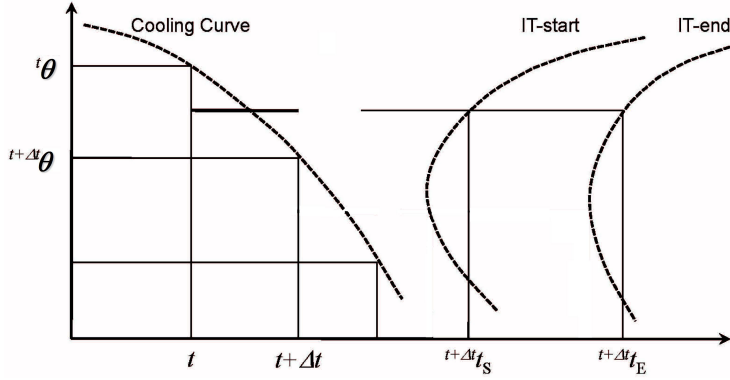


Figure 4.3: Illustration of the Scheil's sum algorithm

For the time step $[t, t + \Delta t]$, Scheil's sum is updated at each integration point by

$${}^{t+\Delta t}S = {}^tS + \frac{\Delta t}{t+\Delta t t_S}. \quad (4.34)$$

If the updated sum is less than 1, it means the transformation has not started yet. Therefore, the phase increment is zero

$$\text{if } {}^{t+\Delta t}S < 1, \text{ then } \Delta f = 0. \quad (4.35)$$

If the updated sum is greater than 1, the previous sum is controlled to decide whether the transformation is started in this time step or has already started before. If the transformation has already started, then the whole time step contributes to the transformation,

$$\text{if } {}^tS > 1, \text{ then } \Delta f = \frac{\Delta t}{t+\Delta t t_E - t+\Delta t t_S} \quad (4.36)$$

Otherwise (i.e., ${}^tS < 1$ and ${}^tS + \Delta S > 1$), only a part of the time step after t^{inc} , which can be calculated explicitly from IT start and cooling curves, contributes to the transformation.

Remark: the stress-dependency of the diffusional transformations is not considered in this study. However, it is known that the IT curves are shifted at high stresses.

4.4.2 Computation of displacive phase fractions

The displacive phase transformations are not time-dependent but only temperature-dependent. Once the temperature drops below the martensite start temperature M_S , the retained austenite starts to convert into martensite. The stress dependency of martensitic transformations can be included in the model by introducing additional stress coefficients in the Koistinen-Marburger equation,

$${}^{t+\Delta t}f_M = {}^t f_A \left\{ 1 - \exp \left[k_M \left({}^{t+\Delta t}\theta - M_S \right) + a_{\sigma_m} {}^t\sigma_m + a_{\sigma_e} {}^t\sigma_{\text{eff}} \right] \right\}, \quad (4.37)$$

where M_S is the martensite start temperature, k_M , a_{σ_m} and a_{σ_e} are material parameters for martensitic transformation, σ_m is the mean stress and σ_{eff} is the effective stress. The current temperature and previous time step stress data used in the computation.

4.5 Displacement field formulation

4.5.1 Preliminaries

Consider a material body which is deforming under some loads. This material body has internal stresses which satisfy the stress equilibrium condition at current configuration. The stress equilibrium equation is

$$\nabla \cdot \mathbf{T} + \mathbf{f}^B = \mathbf{0}. \quad (4.38)$$

The traction \mathbf{f}^S must satisfy boundary conditions $\mathbf{n}^S \cdot \mathbf{T} = \mathbf{f}^S$ on S^f , and the displacement field must conform $\mathbf{u} = \mathbf{u}^S$ on S^u .

The stress equilibrium equation has to be put in a more convenient form before using it in finite element formulations. For an arbitrary chosen displacement field $\tilde{\mathbf{u}}$ (with $\tilde{\mathbf{u}} = \mathbf{0}$ on displacement described boundary), the stress equilibrium equation can be expressed differently. For the solution, the equation

$$\int_V \left[\nabla \cdot \mathbf{T} + \mathbf{f}^B \right] \cdot \tilde{\mathbf{u}} \, dV = 0 \quad (4.39)$$

is apparently satisfied because the bracket in the integral is zero vector. This method is named virtual displacement method. By using the property of divergence operator

$$\nabla \cdot (\mathbf{T} \cdot \tilde{\mathbf{u}}) = (\nabla \cdot \mathbf{T}) \cdot \tilde{\mathbf{u}} + \mathbf{T} : \nabla \tilde{\mathbf{u}} \quad (4.40)$$

the integral in Eq. (4.39) can be written as

$$\int_V \left[\nabla \cdot (\mathbf{T} \cdot \tilde{\mathbf{u}}) - \mathbf{T} : \nabla \tilde{\mathbf{u}} + \mathbf{f}^B \cdot \tilde{\mathbf{u}} \right] dV = 0, \quad (4.41)$$

the first term of which is suitable for the application of divergence theorem. After applying the divergence theorem and the imposition of boundary conditions to Eq. (4.41), the first term becomes

$$\int_V \nabla \cdot (\mathbf{T} \cdot \tilde{\mathbf{u}}) dV = \int_{S^f} [\mathbf{n}^S \cdot (\mathbf{T} \cdot \tilde{\mathbf{u}})] dS = \int_{S^f} [\mathbf{f}^S \cdot \tilde{\mathbf{u}}] dS \quad (4.42)$$

The second term of Eq. (4.41) is a inner product between tensors. Recall the property of tensor inner product that the inner product with a symmetric tensor regards only the symmetric part of the other tensor

$$\mathbf{T} : \nabla \tilde{\mathbf{u}} = \mathbf{T} : \text{sym}(\nabla \tilde{\mathbf{u}}) = \mathbf{T} : \tilde{\mathbf{E}} \quad (4.43)$$

which is equal to the virtual work. After the replacement of the 1st and 2nd terms in Eq. (4.41) with their equivalences in Eqs. (4.42 and 4.43) and some rearrangement,

$$\int_V [\mathbf{T} : \tilde{\mathbf{E}}] dV = \int_{S_f} [\mathbf{f}^S \cdot \tilde{\mathbf{u}}] dS + \int_V [\mathbf{f}^B \cdot \tilde{\mathbf{u}}] dV, \quad (4.44)$$

which is almost ready to be used in the finite element formulations. This equality must be satisfied in the whole domain and sub-domains (i.e., each element) for an arbitrary displacement field $\tilde{\mathbf{u}}$. Recall that the complete domain under consideration can be approximated as an assemblage of finite elements. Over each element, the displacement field is interpolated from the nodal displacements. So, for the e^{th} element, the displacement field is

$$\left. \begin{aligned} u_e &= \mathbf{N}_e^T \mathbf{U}_e \\ v_e &= \mathbf{N}_e^T \mathbf{V}_e \\ w_e &= \mathbf{N}_e^T \mathbf{W}_e \end{aligned} \right\}. \quad (4.45)$$

The strain field is just the gradient of the displacement field,

$$\mathbf{E}_e = \left[\left(\frac{\partial u_e}{\partial x} \right) \quad \left(\frac{\partial v_e}{\partial y} \right) \quad \left(\frac{\partial w_e}{\partial z} \right) \quad \left(\frac{\partial u_e}{\partial y} + \frac{\partial v_e}{\partial x} \right) \quad \left(\frac{\partial u_e}{\partial z} + \frac{\partial w_e}{\partial x} \right) \quad \left(\frac{\partial v_e}{\partial z} + \frac{\partial w_e}{\partial y} \right) \right]^T = \dots \mathbf{B}_e \hat{\mathbf{U}}_e, \quad (4.46)$$

where $\hat{\mathbf{U}}$ is the nodal point displacement vector for the e^{th} element and expressed by

$$\hat{\mathbf{U}}_e = [U_{e1} \quad V_{e1} \quad W_{e1} \quad \dots \quad U_{en} \quad V_{en} \quad W_{en}]^T. \quad (4.47)$$

The matrices \mathbf{N}_e and \mathbf{B}_e are called the element interpolation and strain-displacement matrices, respectively. The number of nodes per element is designated by n . With these descriptions, the integral in Eq. (4.44) can be converted into the following form

$$\sum_e \int_{V_e} [\tilde{\mathbf{U}}_e^T \mathbf{B}_e^T \mathbf{T}_e] dV = \sum_e \int_{S_e} [\tilde{\mathbf{U}}_e^T \mathbf{N}_e^S \mathbf{f}_e^S] dS + \sum_e \int_{V_e} [\tilde{\mathbf{U}}_e^T \mathbf{N}_e \mathbf{f}_e^B] dV, \quad (4.48)$$

where $\tilde{\mathbf{U}}$ is an arbitrary displacement vector that is common on both sides. After the assemblage, $\tilde{\mathbf{U}}$ cancel outs, and a linear system of equation remains to be solved for the unknown nodal displacements. The Newton-Raphson iteration scheme is used to compute the equilibrium state displacements at time $t + \Delta t$. The strain-displacement operator \mathbf{B} relates the displacement increment to the total strain increment, and the tangential stress-strain operator \mathbf{C} relates total strain increment to stress increment for the i^{th} iteration

$$\left. \begin{aligned} \Delta \mathbf{E} &= \mathbf{B}^T \Delta \hat{\mathbf{U}} \\ \Delta \mathbf{T} &= {}^{t+\Delta t}_{i-1} \mathbf{C} \Delta \mathbf{E} \end{aligned} \right\}. \quad (4.49)$$

The incremental forms of nodal displacement vector, integration point strains, and stresses for i^{th} iteration are:

$$\left. \begin{aligned} {}^{t+\Delta t}_i \hat{\mathbf{U}} &= {}^{t+\Delta t}_{i-1} \hat{\mathbf{U}} + \Delta \hat{\mathbf{U}} \\ {}^{t+\Delta t}_0 \mathbf{E} &= {}^t \mathbf{E} + \Delta \mathbf{E}^{tp} + \Delta \mathbf{E}^{trip} \\ {}^{t+\Delta t}_i \mathbf{E} &= {}^{t+\Delta t}_{i-1} \mathbf{E} + \Delta \mathbf{E} = {}^{t+\Delta t}_{i-1} \mathbf{E} + \mathbf{B}^T \Delta \hat{\mathbf{U}} \\ {}^{t+\Delta t}_0 \mathbf{T} &= {}^t \mathbf{T} \\ {}^{t+\Delta t}_i \mathbf{T} &= {}^{t+\Delta t}_{i-1} \mathbf{T} + \Delta \mathbf{T} = {}^{t+\Delta t}_{i-1} \mathbf{T} + {}^{t+\Delta t}_{i-1} \mathbf{C} \Delta \mathbf{E} \end{aligned} \right\}, \quad (4.50)$$

where $\Delta \mathbf{E}^{tp}$ is the spherical strain increment due to temperature and phase changes, and $\Delta \mathbf{E}^{trip}$ is the transformation induced plastic strains occurred in time interval $[t, t + \Delta t]$.

After simplifying Eq. (4.48) and rewriting it at the current time $[t + \Delta t]$, the expression for the stress tensor ${}^{t+\Delta t}_i \mathbf{T}$ as given in Eq. (4.50) is substituted to it. The integral with unknown displacement increment $\Delta \hat{\mathbf{U}}$ is kept on the left-hand-side and all known terms are moved to right-hand-side,

$$\begin{aligned} & \sum_e \int_{V_e} \left[\mathbf{B}_e^T {}^{t+\Delta t}_{i-1} \mathbf{C}_e \mathbf{B}_e \Delta \hat{\mathbf{U}}_e \right] dV = \\ & \sum_e \int_{S_e^f} [\mathbf{N}_e^S {}^{t+\Delta t} \mathbf{f}_e^S] dS + \sum_e \int_{V_e} [\mathbf{N}_e {}^{t+\Delta t} \mathbf{f}_e^B] dV - \sum_e \int_{V_e} [\mathbf{B}_e^T {}^{t+\Delta t}_{i-1} \mathbf{T}_e] dV, \end{aligned} \quad (4.51)$$

or if the matrices are given specific names,

$${}^{t+\Delta t}_{i-1} \mathbf{K} \Delta \hat{\mathbf{U}} = {}^{t+\Delta t} \mathbf{F} - {}^{t+\Delta t}_{i-1} \mathbf{R}, \quad (4.52)$$

where \mathbf{F} is the equivalent nodal load vector for externally applied surface traction \mathbf{f}^S and body forces \mathbf{f}^B . The internal reaction vector \mathbf{R} is taken from the previous iteration. The unbalanced forces produce the additional displacement increment $\Delta \hat{\mathbf{U}}$.

Global finite element matrices are assembled from element matrices by using the connectivity data. Element matrices are obtained by numerical integration. The stiffness matrix, force and response vectors are:

$$\left. \begin{aligned} {}^{t+\Delta t}_{i-1} \mathbf{K} &= \sum_e \int_{V_e} [\mathbf{B}_e^T {}^{t+\Delta t}_{i-1} \mathbf{C}_e \mathbf{B}_e] dV \\ {}^{t+\Delta t} \mathbf{F} &= \sum_e \int_{S_e^f} [\mathbf{N}_e^S {}^{t+\Delta t} \mathbf{f}_e^S] dS + \sum_e \int_{V_e} [\mathbf{N}_e {}^{t+\Delta t} \mathbf{f}_e^B] dV \\ {}^{t+\Delta t}_{i-1} \mathbf{R} &= \sum_e \int_{V_e} [\mathbf{B}_e^T {}^{t+\Delta t}_{i-1} \mathbf{T}_e] dV \end{aligned} \right\}. \quad (4.53)$$

The integrals are calculated numerically by Gauss-Quadrature rule. Three points are selected in each coordinate axis direction. Therefore, 2D elements have nine integration points in the area and three integration points on each side, 3D elements have twenty-seven integration points in the volume and nine integration points on each face.

4.5.2 Two-dimensional elements

It has been already stated that the mathematical model of the profile problem can be reduced to a two dimensional problem with much fewer degrees of freedom. In 2D finite element implementations, usually plane stress, plane strain, and axis symmetric elements are combined in a single routine. In this work, an additional beam cross-section element type is introduced in addition to these three elements. For the *beam cross-section*, three additional degrees of freedom have to be considered to account the beam elongation, bending about the x-axis and about the y-axis. These beam degrees of freedom are common to all the elements in a beam cross-section following the famous Bernoulli-Euler slender beam assumption (i.e., plane sections before bending remain plane after bending). The finite element calculations for these four types of elements are very similar to each others. There are only minor differences while performing the numerical integrations to form the element matrices and vectors. These differences do not change the general formulation. The infinitesimal volume dV , infinitesimal area dA , stress-strain operator \mathbf{C} , and strain-displacement operator \mathbf{B} which frequently appear in the integrals slightly differ from each others. This is obvious from the modeled actual 3D geometry and boundary conditions in the perpendicular direction. A typical 2D element and its node numbering in local and global coordinates are shown in Fig. 4.4.

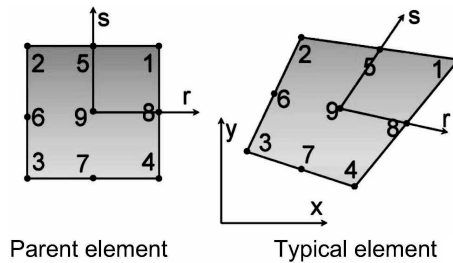


Figure 4.4: Typical 2D element for displacement calculation

The infinitesimal volume for volume integral computations is

$$dV = \ell |\mathbf{J}| dr ds. \quad (4.54)$$

The infinitesimal area for surface integral computations is

$$dA = \begin{cases} \ell |\mathbf{J}^{(2)}| ds & \text{on faces 1\&2} \\ \ell |\mathbf{J}^{(1)}| dr & \text{on faces 3\&4} \end{cases}, \quad (4.55)$$

where $\mathbf{J}^{(i)}$ represents the i^{th} column vector of the Jacobian matrix, $\mathbf{J}^{(1)}dr$ and $\mathbf{J}^{(2)}ds$ are the mapping of the infinitesimal vectors dr and ds to global coordinates, and ℓ is the thickness in the perpendicular direction. For plane strain, plane stress, beam cross-section and axis symmetric element formulations, the values of thickness ℓ are:

$$\ell = \begin{cases} 1 & \text{unit length} & \text{if plane strain or beam cross-section} \\ \ell & \text{real thickness} & \text{if plane stress} \\ x & \text{the radius} & \text{if axis symmetric (1 rad is considered)} \end{cases}. \quad (4.56)$$

The faces of the elements are used for evaluation of the natural boundary conditions. According to node numbering in Fig. 4.1, the left and right sides are called faces 1&2, and top and bottom sides are called faces 3&4, respectively.

An isoparametric element formulation has been performed. That is, the same interpolation functions are used to map the element geometry and displacement field. Hence, for a given local coordinates (r, s) , the global coordinates and displacements are

$$\left. \begin{array}{l} x(r, s) = \mathbf{N}^T \mathbf{X} \\ y(r, s) = \mathbf{N}^T \mathbf{Y} \end{array} \right\} \quad \text{and} \quad \left. \begin{array}{l} u(r, s) = \mathbf{N}^T \mathbf{U} \\ v(r, s) = \mathbf{N}^T \mathbf{V} \end{array} \right\}, \quad (4.57)$$

where the vectors \mathbf{X} and \mathbf{Y} are the coordinates of the nodes, vectors \mathbf{U} and \mathbf{V} are the nodal displacements and \mathbf{N} is the interpolation functions,

$$\mathbf{N} = \begin{bmatrix} 0.25(r^2+r)(s^2+s) \\ 0.25(r^2-r)(s^2+s) \\ 0.25(r^2-r)(s^2-s) \\ 0.25(r^2+r)(s^2-s) \\ 0.5(1-r^2)(s^2+s) \\ 0.5(r^2-r)(1-s^2) \\ 0.5(1-r^2)(s^2-s) \\ 0.5(r^2+r)(1-s^2) \\ (1-r^2)(1-s^2) \end{bmatrix}. \quad (4.58)$$

The calculations of element matrices require the derivatives of displacements u and v with respect to global coordinates x and y . The operator \mathbf{H} performs this operation. For obtaining operator \mathbf{H} , the chain rule can be applied in the following manner,

$$\begin{bmatrix} \frac{\partial}{\partial r} \\ \frac{\partial}{\partial s} \end{bmatrix} = \begin{bmatrix} \frac{\partial x}{\partial r} & \frac{\partial y}{\partial r} \\ \frac{\partial x}{\partial s} & \frac{\partial y}{\partial s} \end{bmatrix} \begin{bmatrix} \frac{\partial}{\partial x} \\ \frac{\partial}{\partial y} \end{bmatrix} = \mathbf{J}^T \begin{bmatrix} \frac{\partial}{\partial x} \\ \frac{\partial}{\partial y} \end{bmatrix}. \quad (4.59)$$

Therefore, the Jacobian is defined as

$$\mathbf{J} = \begin{bmatrix} \frac{\partial x}{\partial r} & \frac{\partial x}{\partial s} \\ \frac{\partial y}{\partial r} & \frac{\partial y}{\partial s} \end{bmatrix} = \begin{bmatrix} \frac{\partial \mathbf{N}^T \mathbf{X}}{\partial r} & \frac{\partial \mathbf{N}^T \mathbf{X}}{\partial s} \\ \frac{\partial \mathbf{N}^T \mathbf{Y}}{\partial r} & \frac{\partial \mathbf{N}^T \mathbf{Y}}{\partial s} \end{bmatrix}, \quad \text{or} \quad \mathbf{J}^T = \begin{bmatrix} \frac{\partial \mathbf{N}}{\partial r} & \frac{\partial \mathbf{N}}{\partial s} \end{bmatrix}^T \begin{bmatrix} \mathbf{X} & \mathbf{Y} \end{bmatrix}. \quad (4.60)$$

To calculate the Jacobian, the derivatives with respect to local coordinates $\frac{\partial \mathbf{N}}{\partial r}$ and $\frac{\partial \mathbf{N}}{\partial s}$ are required. The derivatives with respect to global coordinates $\frac{\partial}{\partial x}$ and $\frac{\partial}{\partial y}$ can be obtained by inverting Eq. (4.59). So, the derivative operator \mathbf{H} , which has the size of 2×9 , is by definition,

$$\mathbf{H} = \begin{bmatrix} \frac{\partial}{\partial x} \\ \frac{\partial}{\partial y} \end{bmatrix} \mathbf{N}^T = \mathbf{J}^{-T} \begin{bmatrix} \frac{\partial}{\partial r} \\ \frac{\partial}{\partial s} \end{bmatrix} \mathbf{N}^T. \quad (4.61)$$

After these preliminary definitions, now the strain-displacement operators can be written for plane stress, plane strain, axis-symmetric and beam cross-section elements.

The strain-displacement operator for the plane stress case is the simplest one and it is referred in this text as standard strain-displacement operator with size 3×18 ,

$$\mathbf{B} = \mathbf{B}_{\text{std}} = \begin{bmatrix} H_{1i} & 0 & \cdots \\ 0 & H_{2i} & \cdots \\ H_{2i} & H_{1i} & \cdots \end{bmatrix}, \quad (4.62)$$

where H_{1i} and H_{2i} are the elements of the first and second rows of derivative operator \mathbf{H} .

The strain-displacement operator for the axis-symmetric case has an additional row. Therefore, its size is 4×18

$$\mathbf{B} = \begin{bmatrix} \mathbf{B}_{\text{std}} \\ \mathbf{B}_{\text{axs}} \end{bmatrix}, \text{ where } \mathbf{B}_{\text{axs}} = \begin{bmatrix} \frac{N_i}{x} & 0 & \dots \end{bmatrix}, \quad (4.63)$$

where N_i are the elements of the interpolation vector \mathbf{N} , and x is the global radial coordinate.

The strain-displacement matrix for the beam case has size 4×21 . There is one additional row and three additional columns. The introduced addition is named \mathbf{B}_{beam} and

$$\mathbf{B} = \begin{bmatrix} \mathbf{B}_{\text{std}} & \mathbf{0} \\ \mathbf{0} & \mathbf{B}_{\text{beam}} \end{bmatrix}, \text{ where } \mathbf{B}_{\text{beam}} = \frac{1}{L} \begin{bmatrix} 1 & y & -x \end{bmatrix}. \quad (4.64)$$

The additional operator \mathbf{B}_{beam} is used for computing the strain in the axial direction, which is just related to axial elongation and bending curvatures.

The stress-strain operator (constitutive matrix, the derivation is discussed in section 3.3.1),

$$\mathbf{C}_{\text{std}}^{\text{ep}} = 3\kappa\hat{\mathbf{P}}_1 + 2\mu\hat{\mathbf{P}}_2 - \frac{2\mu}{1 + \frac{H}{3\mu}}\hat{\mathbf{n}}'_T - \lambda \frac{4\mu^2}{\|(\mathbf{T}')^{\text{trial}}\|} \left(\hat{\mathbf{P}}_2 - \hat{\mathbf{n}}'_T \right) \quad (4.65)$$

where $\hat{\mathbf{P}}_1$ is the spherical projector, $\hat{\mathbf{P}}_2$ is the deviator projector and $\hat{\mathbf{n}}'_T$ is the plastic flow direction projector. Since in the case of plane stress case the stress in the perpendicular direction is zero, the projectors are of size 3×3 ,

$$\hat{\mathbf{P}}_1 = \frac{1}{3} \begin{bmatrix} 1 & 1 & 0 \\ 1 & 1 & 0 \\ 0 & 0 & 0 \end{bmatrix}, \quad \hat{\mathbf{P}}_2 = \frac{1}{2} \begin{bmatrix} +\frac{4}{3} & -\frac{2}{3} & 0 \\ -\frac{2}{3} & +\frac{4}{3} & 0 \\ 0 & 0 & 1 \end{bmatrix}, \quad \hat{\mathbf{n}}'_T = \mathbf{n}'_T (\mathbf{n}'_T)^T = \frac{\mathbf{T}' (\mathbf{T}')^T}{\|\mathbf{T}'\|^2}. \quad (4.66)$$

For all other cases (plane strain, axis-symmetric and beam cases), projectors are of size 4×4 ,

$$\hat{\mathbf{P}}_1 = \frac{1}{3} \begin{bmatrix} 1 & 1 & 0 & 1 \\ 1 & 1 & 0 & 1 \\ 0 & 0 & 0 & 0 \\ 1 & 1 & 0 & 1 \end{bmatrix}, \quad \hat{\mathbf{P}}_2 = \frac{1}{2} \begin{bmatrix} +\frac{4}{3} & -\frac{2}{3} & 0 & -\frac{2}{3} \\ -\frac{2}{3} & +\frac{4}{3} & 0 & -\frac{2}{3} \\ 0 & 0 & 1 & 0 \\ -\frac{2}{3} & -\frac{2}{3} & 0 & +\frac{4}{3} \end{bmatrix}. \quad (4.67)$$

4.5.3 Three-dimensional element

For the modeling of general 3D models, a 27-node isoparametric brick element is introduced. Formulation of the 3D element is straight forward and special considerations are not required as in the case of 2D elements. A typical 3D parent element and its node numbering is shown in Fig. 4.5

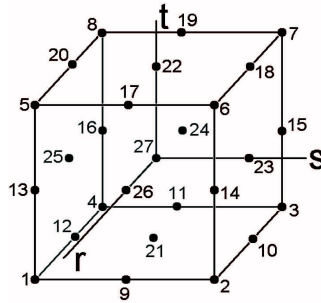


Figure 4.5: Typical 3D parent element and its node numbering

The infinitesimal volume for volume integral computations is

$$dV = |\mathbf{J}| dr ds dt. \quad (4.68)$$

The infinitesimal area for surface integral computations is

$$dA = \begin{cases} |\mathbf{J}^{(2)} \times \mathbf{J}^{(3)}| ds dt & \text{for face 1\&2} \\ |\mathbf{J}^{(1)} \times \mathbf{J}^{(3)}| dr dt & \text{for face 3\&4} \\ |\mathbf{J}^{(1)} \times \mathbf{J}^{(2)}| dr ds & \text{for face 5\&6} \end{cases}, \quad (4.69)$$

where $\mathbf{J}^{(i)}$ represents the i^{th} column vector of the Jacobian matrix, $\mathbf{J}^{(1)}dr$, $\mathbf{J}^{(2)}ds$ and $\mathbf{J}^{(3)}dt$ are the mapping of infinitesimal vectors dr , ds and dt to global coordinates, respectively. So, the cross product simply gives the infinitesimal area dA .

The faces define the six boundary of the element. According to node numbering in Fig. 4.5, the front and back faces are called faces 1-2, left and right faces are called faces 3-4, and top and bottom faces are called faces 5-6, all respectively.

An isoparametric element formulation has been performed. That is, the same interpolation functions are used to map the element geometry and displacement field. Hence, for a given local coordinates (r, s, t) , the global coordinates (x, y, z) and displacements (u, v, w) are

$$\left. \begin{aligned} x(r, s, t) &= \mathbf{N}^T \mathbf{X} \\ y(r, s, t) &= \mathbf{N}^T \mathbf{Y} \\ z(r, s, t) &= \mathbf{N}^T \mathbf{Z} \end{aligned} \right\} \text{ and } \left. \begin{aligned} u(r, s, t) &= \mathbf{N}^T \mathbf{U} \\ v(r, s, t) &= \mathbf{N}^T \mathbf{V} \\ w(r, s, t) &= \mathbf{N}^T \mathbf{W} \end{aligned} \right\}, \quad (4.70)$$

where the vectors, \mathbf{X} , \mathbf{Y} and \mathbf{Z} , are coordinates of the nodes, vectors \mathbf{U} , \mathbf{V} and

\mathbf{W} , are the nodal displacements and \mathbf{N} is the interpolation functions,

$$\mathbf{N} = \begin{bmatrix} +0.125(r+r^2)(s-s^2)(t-t^2) \\ -0.125(r+r^2)(s+s^2)(t-t^2) \\ +0.125(r-r^2)(s+s^2)(t-t^2) \\ -0.125(r-r^2)(s-s^2)(t-t^2) \\ -0.125(r+r^2)(s-s^2)(t+t^2) \\ +0.125(r+r^2)(s+s^2)(t+t^2) \\ -0.125(r-r^2)(s+s^2)(t+t^2) \\ +0.125(r-r^2)(s-s^2)(t+t^2) \\ -0.25(r+r^2)(1-s^2)(t-t^2) \\ -0.25(1-r^2)(s+s^2)(t-t^2) \\ +0.25(r-r^2)(1-s^2)(t-t^2) \\ +0.25(1-r^2)(s-s^2)(t-t^2) \\ -0.25(r+r^2)(s-s^2)(1-t^2) \\ +0.25(r+r^2)(s+s^2)(1-t^2) \\ -0.25(r-r^2)(s+s^2)(1-t^2) \\ +0.25(r-r^2)(s-s^2)(1-t^2) \\ +0.25(r+r^2)(1-s^2)(t+t^2) \\ +0.25(1-r^2)(s+s^2)(t+t^2) \\ -0.25(r-r^2)(1-s^2)(t+t^2) \\ -0.25(1-r^2)(s-s^2)(t+t^2) \\ -0.5(1-r^2)(1-s^2)(t-t^2) \\ +0.5(r+r^2)(1-s^2)(1-t^2) \\ +0.5(1-r^2)(s+s^2)(1-t^2) \\ -0.5(r-r^2)(1+s^2)(1-t^2) \\ -0.5(1-r^2)(s-s^2)(1-t^2) \\ +0.5(1-r^2)(1-s^2)(t+t^2) \\ (1-r^2)(1-s^2)(1-t^2) \end{bmatrix}. \quad (4.71)$$

The calculations of element matrices require the derivatives with respect to global coordinates. The operator \mathbf{H} performs this operation. For obtaining the operator \mathbf{H} , the chain rule can be applied in the following manner,

$$\begin{bmatrix} \frac{\partial}{\partial r} \\ \frac{\partial}{\partial s} \\ \frac{\partial}{\partial t} \end{bmatrix} = \begin{bmatrix} \frac{\partial x}{\partial r} & \frac{\partial y}{\partial r} & \frac{\partial z}{\partial r} \\ \frac{\partial x}{\partial s} & \frac{\partial y}{\partial s} & \frac{\partial z}{\partial s} \\ \frac{\partial x}{\partial t} & \frac{\partial y}{\partial t} & \frac{\partial z}{\partial t} \end{bmatrix} \begin{bmatrix} \frac{\partial}{\partial x} \\ \frac{\partial}{\partial y} \\ \frac{\partial}{\partial z} \end{bmatrix} = \mathbf{J}^T \begin{bmatrix} \frac{\partial}{\partial x} \\ \frac{\partial}{\partial y} \\ \frac{\partial}{\partial z} \end{bmatrix}. \quad (4.72)$$

Therefore, the Jacobian is defined as

$$\mathbf{J} = \left. \begin{aligned} & \begin{bmatrix} \frac{\partial x}{\partial r} & \frac{\partial x}{\partial s} & \frac{\partial x}{\partial t} \\ \frac{\partial y}{\partial r} & \frac{\partial y}{\partial s} & \frac{\partial y}{\partial t} \\ \frac{\partial z}{\partial r} & \frac{\partial z}{\partial s} & \frac{\partial z}{\partial t} \end{bmatrix} = \begin{bmatrix} \frac{\partial \mathbf{N}^T}{\partial r} \mathbf{X} & \frac{\partial \mathbf{N}^T}{\partial s} \mathbf{X} & \frac{\partial \mathbf{N}^T}{\partial t} \mathbf{X} \\ \frac{\partial \mathbf{N}^T}{\partial r} \mathbf{Y} & \frac{\partial \mathbf{N}^T}{\partial s} \mathbf{Y} & \frac{\partial \mathbf{N}^T}{\partial t} \mathbf{Y} \\ \frac{\partial \mathbf{N}^T}{\partial r} \mathbf{Z} & \frac{\partial \mathbf{N}^T}{\partial s} \mathbf{Z} & \frac{\partial \mathbf{N}^T}{\partial t} \mathbf{Z} \end{bmatrix} \\ & \mathbf{J}^T = \left[\frac{\partial \mathbf{N}}{\partial r} \quad \frac{\partial \mathbf{N}}{\partial s} \quad \frac{\partial \mathbf{N}}{\partial t} \right]^T \left[\mathbf{X} \quad \mathbf{Y} \quad \mathbf{Z} \right] \end{aligned} \right\}. \quad (4.73)$$

To calculate the Jacobian, the derivatives with respect to local coordinates, $\frac{\partial \mathbf{N}}{\partial r}$ and $\frac{\partial \mathbf{N}}{\partial s}$ are required. The derivative operator \mathbf{H} , whose size is 3×27 , is by definition:

$$\mathbf{H} = \begin{bmatrix} \frac{\partial}{\partial x} \\ \frac{\partial}{\partial y} \\ \frac{\partial}{\partial z} \end{bmatrix} \mathbf{N}^T = \mathbf{J}^{-T} \begin{bmatrix} \frac{\partial}{\partial r} \\ \frac{\partial}{\partial s} \\ \frac{\partial}{\partial t} \end{bmatrix} \mathbf{N}^T. \quad (4.74)$$

Now the strain-displacement relation, which has a size 6×81 , can be written as

$$\mathbf{B} = \begin{bmatrix} H_{1i} & 0 & 0 & \cdots \\ 0 & H_{2i} & 0 & \cdots \\ 0 & 0 & H_{3i} & \cdots \\ H_{2i} & H_{1i} & 0 & \cdots \\ H_{3i} & 0 & H_{1i} & \cdots \\ 0 & H_{3i} & H_{2i} & \cdots \end{bmatrix}, \quad (4.75)$$

where H_{1i} , H_{2i} and H_{3i} are the elements of the first second and third row of derivative operator \mathbf{H} .

The formulation of the stress-strain operator was performed in section 3.3.1

$$\hat{\mathbf{C}}_{std}^{ep} = 3\kappa\hat{\mathbf{P}}_1 + 2\mu\hat{\mathbf{P}}_2 - \frac{2\mu}{1 + \frac{H}{3\mu}}\hat{\mathbf{n}}'_T - \lambda \frac{4\mu^2}{\|\mathbf{T}'^{trial}\|} \left(\hat{\mathbf{P}}_2 - \hat{\mathbf{n}}'_T \right), \quad (4.76)$$

where the projectors are:

$$\hat{\mathbf{P}}_1 = \frac{1}{3} \begin{bmatrix} 1 & 1 & 1 & 0 & 0 & 0 \\ 1 & 1 & 1 & 0 & 0 & 0 \\ 1 & 1 & 1 & 0 & 0 & 0 \\ 0 & 0 & 0 & 0 & 0 & 0 \\ 0 & 0 & 0 & 0 & 0 & 0 \\ 0 & 0 & 0 & 0 & 0 & 0 \end{bmatrix}, \quad \hat{\mathbf{P}}_2 = \frac{1}{2} \begin{bmatrix} +\frac{4}{3} & -\frac{2}{3} & -\frac{2}{3} & 0 & 0 & 0 \\ -\frac{2}{3} & +\frac{4}{3} & -\frac{2}{3} & 0 & 0 & 0 \\ -\frac{2}{3} & -\frac{2}{3} & +\frac{4}{3} & 0 & 0 & 0 \\ 0 & 0 & 0 & 1 & 0 & 0 \\ 0 & 0 & 0 & 0 & 1 & 0 \\ 0 & 0 & 0 & 0 & 0 & 1 \end{bmatrix}$$

$$\hat{\mathbf{n}}'_T = \mathbf{n}'_T (\mathbf{n}'_T)^T = \frac{\mathbf{T}' (\mathbf{T}')^T}{\|\mathbf{T}'\|^2}. \quad (4.77)$$

4.5.4 Integration scheme for the plastic strains

The equilibrium iterations for the stress-strain calculations require an integration algorithm for the plastic strains at time $t + \Delta t$. The calculation of plastic strain is one of the major steps in the solution of plasticity problems. In this subsection the integration algorithm for the plastic strains will be explained. The most commonly used and most simple method is the Euler backward method for the total plastic strain tensor and the hardening parameter,

$$\left. \begin{aligned} {}^{t+\Delta t}_i \mathbf{E}^{pl} &= {}^{t+\Delta t}_{i-1} \mathbf{E}^{pl} + \lambda \frac{{}^{t+\Delta t}_i \mathbf{n}'_T}{\sqrt{\frac{2}{3}}} \\ {}^{t+\Delta t}_i \varepsilon^{pl} &= {}^{t+\Delta t}_{i-1} \varepsilon^{pl} + \sqrt{\frac{2}{3}} \lambda \end{aligned} \right\}, \quad (4.78)$$

where \mathbf{E} (i.e., $\mathbf{E} = [\varepsilon_{xx} \ \varepsilon_{yy} \ \varepsilon_{zz} \ \varepsilon_{xy} \ \varepsilon_{xz} \ \varepsilon_{yz}]^T$) is the vector form of the strain tensor, \mathbf{n}'_T is the unit direction vector for the stress deviator, ε^{pl} is the plastic hardening state variable, λ is the plastic multiplier, and i is the current equilibrium iteration number. Similar to the strain tensor, \mathbf{T} (i.e., $\mathbf{T} = [\sigma_{xx} \ \sigma_{yy} \ \sigma_{zz} \ \sigma_{xy} \ \sigma_{xz} \ \sigma_{yz}]^T$) is the vector form of the stress tensor. The stress state at the end of time increment is

$$\begin{aligned} {}^{t+\Delta t}_i \mathbf{T} &= {}^{t+\Delta t}_i \mathbf{C}^{el} \ {}^{t+\Delta t}_i \mathbf{E}^{el} = \dots \\ &= {}^{t+\Delta t}_i \kappa \operatorname{tr} \left({}^{t+\Delta t}_i \mathbf{E} - {}^{t+\Delta t}_i \mathbf{E}^{tp} \right) \mathbf{I} + 2 \ {}^{t+\Delta t}_i \mu \left({}^{t+\Delta t}_i \mathbf{E}' - {}^{t+\Delta t}_i \mathbf{E}^{trip} - {}^{t+\Delta t}_i \mathbf{E}^{pl} \right). \end{aligned} \quad (4.79)$$

The deviatoric part of the stress tensor is

$$\|{}^{t+\Delta t}_i \mathbf{T}'\| \ {}^{t+\Delta t}_i \mathbf{n}'_T = 2 \ {}^{t+\Delta t}_i \mu \left({}^{t+\Delta t}_i \mathbf{E}' - {}^{t+\Delta t}_i \mathbf{E}^{trip} - {}^{t+\Delta t}_{i-1} \mathbf{E}^{pl} - \lambda \ {}^{t+\Delta t}_i \mathbf{n}'_T \right). \quad (4.80)$$

The trial deviatoric stress is defined as

$$\left. \begin{aligned} & \left({}^{t+\Delta t} \mathbf{T}' \right)^{trial} = 2 \left({}^{t+\Delta t} \mu \left({}^{t+\Delta t} \mathbf{E}' - {}^{t+\Delta t} \mathbf{E}^{trip} - {}^{t+\Delta t} \mathbf{E}^{pl} \right) \right) \\ & \left\| \left({}^{t+\Delta t} \mathbf{T}' \right)^{trial} \right\| \left({}^{t+\Delta t} \mathbf{n}'_{\mathbf{T}} \right)^{trial} = \left\| {}^{t+\Delta t} \mathbf{T}' \right\| {}^{t+\Delta t} \mathbf{n}'_{\mathbf{T}} + 2 \left({}^{t+\Delta t} \mu \lambda \right) {}^{t+\Delta t} \mathbf{n}'_{\mathbf{T}} \end{aligned} \right\} \quad (4.81)$$

From the last equation, the following expression can easily be derived,

$${}^{t+\Delta t} \mathbf{n}'_{\mathbf{T}} = \left({}^{t+\Delta t} \mathbf{n}'_{\mathbf{T}} \right)^{trial} = \frac{\left({}^{t+\Delta t} \mathbf{T}' \right)^{trial}}{\left\| \left({}^{t+\Delta t} \mathbf{T}' \right)^{trial} \right\|} \quad (4.82)$$

The value of $\left\| \left({}^{t+\Delta t} \mathbf{T}' \right)^{trial} \right\|$ is already known from the flow criterion,

$$\left. \begin{aligned} \sqrt{\frac{2}{3}} \left({}^{t+\Delta t} \sigma_y \right) &= \sqrt{\frac{2}{3}} \left({}^{t+\Delta t} \sigma_y + \sqrt{\frac{2}{3}} \lambda \left({}^{t+\Delta t} H \right) \right) = \left\| \left({}^{t+\Delta t} \mathbf{T}' \right)^{trial} \right\| - 2 \left({}^{t+\Delta t} \mu \lambda \right) \\ \lambda &= \frac{\left\| \left({}^{t+\Delta t} \mathbf{T}' \right)^{trial} \right\| - \sqrt{\frac{2}{3}} \left({}^{t+\Delta t} \sigma_y \right)}{2 \left({}^{t+\Delta t} \mu + \frac{2}{3} \left({}^{t+\Delta t} H \right) \right)} = \frac{\left({}^{t+\Delta t} \phi \right)^{trial}}{2 \left({}^{t+\Delta t} \mu + \frac{2}{3} \left({}^{t+\Delta t} H \right) \right)} \end{aligned} \right\} \quad (4.83)$$

The relationship, ${}^{t+\Delta t} \mathbf{C}^{alg}$, which is the partial derivative of the stress increment $\Delta \mathbf{T}$ with respect to total strain increment $\Delta \mathbf{E} = \Delta \mathbf{E}^{el} + \Delta \mathbf{E}^{pl}$, is called algorithmic stress-strain operator at time $t + \Delta t$,

$$\begin{aligned} {}^{t+\Delta t} \mathbf{C}^{alg} &= \frac{\partial \Delta \mathbf{T}}{\partial \Delta \mathbf{E}} = \dots \\ 3 \left({}^{t+\Delta t} \kappa \hat{\mathbf{P}}_1 + 2 \left({}^{t+\Delta t} \mu \hat{\mathbf{P}}_2 - \frac{2 \left({}^{t+\Delta t} \mu \right)}{1 + \frac{t+\Delta t}{3} \frac{H}{t+\Delta t} \mu} \left({}^{t+\Delta t} \hat{\mathbf{n}}'_{\mathbf{T}} - \lambda \frac{4 \left({}^{t+\Delta t} \mu \right)^2}{\left\| \left({}^{t+\Delta t} \mathbf{T}' \right)^{trial} \right\|} \left(\hat{\mathbf{P}}_2 - {}^{t+\Delta t} \hat{\mathbf{n}}'_{\mathbf{T}} \right) \right) \right) \end{aligned} \quad (4.84)$$

4.6 Summary

The mathematical model for the quenching process was introduced in this chapter. Transient temperature field, solid state phase transitions, and displacement field models are separately discussed but coupling terms are addressed during the explanations. Different material properties of the mixture are estimated by using different mixture rules. So, a generalized mixture rule is also introduced. Finally, the descriptions of the distortion was stated for the geometries considered in this study.

Chapter 5

Validation of mathematical model

5.1 Introduction

The simulation results are compared with the known analytical solutions for simple geometries in order to test the correctness of the individual parts of the mathematical model and their computational implementations. The complete coupled model is tested by comparing the simulation results with experimental measurements. Fourier's heat conduction equation has analytical solutions only for simple geometries such as rectangular, circular, prismatic, cylindrical or spherical domains. These analytical solutions are represented by the sum of an infinite series, which is truncated for the approximation. The phase transformation model is established on the basis of Time-Temperature-Transformation (TTT) diagrams, which are experimentally determined. The Continuous-Cooling-Transformation (CCT) diagrams can be obtained from Isothermal Transformation (IT), or TTT diagrams by using the Scheil's additivity rule for a range of different cooling rates. The displacement and stress-strain state can be analytically computed only for simple geometries and simple boundary conditions, which usually produce a uniform stress-strain field. Such problems are called patch tests in the literature [Bat96]. Although, the individual fields can be computed analytically for simple boundary conditions and over simple domains, it is not possible to obtain an analytical solution for the coupled problem. Therefore, experimental results, which are available in the literature [BSO⁺05, BSO⁺06, BKS05], for the shaft and disk geometries are compared with the simulation results.

5.2 Validation of temperature field formulation

The linear heat conduction equation can be solved for very simple geometries. However, it is not possible to find out such analytical solutions for complex geometries and for nonlinear cases. Numerical methods are applicable to both linear and nonlinear cases. The correctness of the implementation of the temperature field formulation is controlled by comparing the known analytical solution

for a very simple prismatic geometry, which is shown in Fig. 5.1 and subjected to an equal cooling over all the boundaries. Even for this simple geometry the analytical solution equations have very complex forms. The derivation of these equations can be found in heat transfer handbooks such as [CJ96]. Because of the symmetry of the geometry and boundary conditions, only the positive octant is considered.

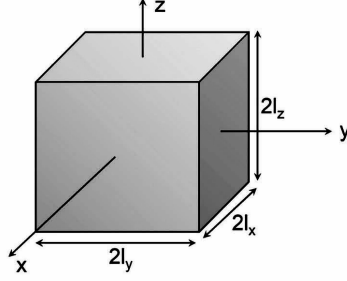


Figure 5.1: Geometry of the solid prism for analytical solution of convective cooling

In order to avoid the repetitions, the solution equations are directly given here. Some dimensionless numbers, i.e., the thermal diffusivity, Fourier number, Biot number, are used to get the results. Thermal diffusivity is defined as

$$a = \frac{k}{\rho c_p}, \quad (5.1)$$

where k is the heat conductivity, ρ is the density and c_p is the specific heat. Fourier numbers are:

$$Fo_x = \frac{at}{l_x^2}, \quad Fo_y = \frac{at}{l_y^2}, \quad Fo_z = \frac{at}{l_z^2}, \quad (5.2)$$

where t is the time, l_x , l_y and l_z are dimensions of the prism. Biot numbers are:

$$Bi_x = \frac{\alpha_x l_x}{k}, \quad Bi_y = \frac{\alpha_y l_y}{k}, \quad Bi_z = \frac{\alpha_z l_z}{k}, \quad (5.3)$$

where α_x , α_y and α_z are the heat transfer coefficients on the corresponding surfaces. The solution equations (see Eq. (5.6)) involve the eigenvalues, which are obtained by solving

$$q_x \tan(q_x) = Bi_x, \quad q_y \tan(q_y) = Bi_y, \quad q_z \tan(q_z) = Bi_z. \quad (5.4)$$

The positive roots of the eigenvalue problems are

$$q_{xi}, \quad q_{yi}, \quad q_{zi}, \quad i = (1, 2, 3, \dots). \quad (5.5)$$

Then, the normalized temperature fractions in each direction are computed by the infinite sums

$$\left. \begin{aligned} \theta_x &= \sum_{i=1}^{\infty} \frac{2 \sin(q_{xi})}{q_{xi} + \sin(q_{xi}) \cos(q_{xi})} \cos(q_{xi} \frac{x}{l_x}) \exp(-q_{xi}^2 Fo_x) \\ \theta_y &= \sum_{i=1}^{\infty} \frac{2 \sin(q_{yi})}{q_{yi} + \sin(q_{yi}) \cos(q_{yi})} \cos(q_{yi} \frac{y}{l_y}) \exp(-q_{yi}^2 Fo_y) \\ \theta_z &= \sum_{i=1}^{\infty} \frac{2 \sin(q_{zi})}{q_{zi} + \sin(q_{zi}) \cos(q_{zi})} \cos(q_{zi} \frac{z}{l_z}) \exp(-q_{zi}^2 Fo_z) \end{aligned} \right\}. \quad (5.6)$$

Although, these temperatures are obtained from an infinite series sum, usually first few terms of the series are enough because of exponentially decaying term to approximate the sum with adequate accuracy.

The normalized temperature at point (x,y,z) at time t is

$$\theta_{xyz} = \theta_x \theta_y \theta_z = \frac{\theta - \theta_g}{\theta_0 - \theta_g}. \quad (5.7)$$

In the case of 2D computations, the parameters with indices x and y are only used, those with z index are all not involved in calculations.

Example : An imaginary material is considered with density $\rho = 1000 \text{ kg/m}^3$, heat capacity $c_p = 1000 \text{ J/kg/K}$, and conductivity $k = 100 \text{ W/m/K}$. The heat transfer coefficient is $\alpha = 1000 \text{ W/m}^2/\text{K}$, initial temperature is $\theta_0 = 1000 \text{ K}$ and the surrounding temperature $\theta_g = 300 \text{ K}$. Cross-section of a continuous beam with $l_x = l_y = 0.1 \text{ m}$ is considered for simplicity. The performance of the numerical method is evaluated by varying the time increment and the mesh density. The temperatures at the corner, middle of the surface and center are represented by θ_1 , θ_2 and θ_3 respectively. The errors in the finite element calculations are plotted in Fig. 5.2, Fig. 5.3 and Fig. 5.4 for temperatures θ_1 , θ_2 and θ_3 , respectively. Two different meshes and two different time step sizes have been used. For the coarse mesh dashed lines and for the fine mesh solid lines are used. For the small time stepping red light and for the big time stepping dark color is used in the figures. The analytical results and finite element results are also listed in Table. 5.1 for convenience. The errors are zero when $t = 1000 \text{ s}$ because the cooling is completed (the material and environment temperatures are equal). For big time steps, the error is very high when $t = 100 \text{ s}$ since the time increments are very big as they are logarithmically increased. In Fig. 5.4, the error is zero until $t = 3 \text{ s}$ since the core temperature θ_3 start reducing only after 3 s . According to the results, it is essential to use small time steps to obtain a good accuracy. On the other hand, the mesh refinement has relatively less effect on the accuracy.

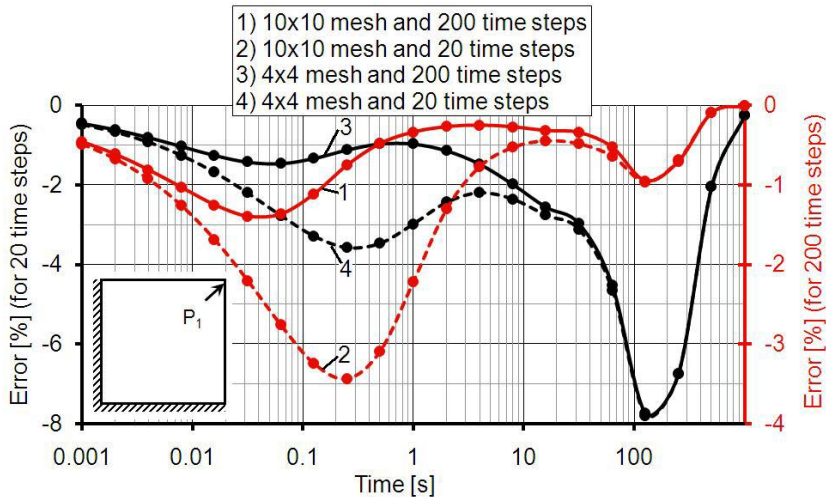


Figure 5.2: Error in computed temperature θ_1 at the corner vs. time

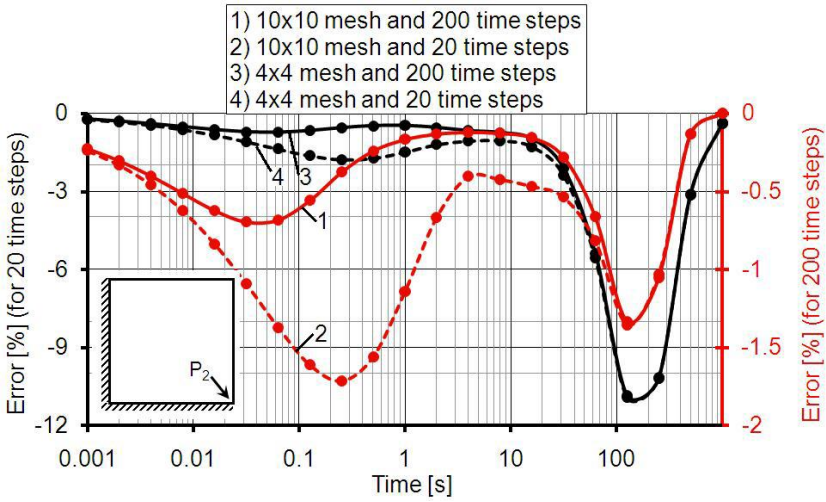
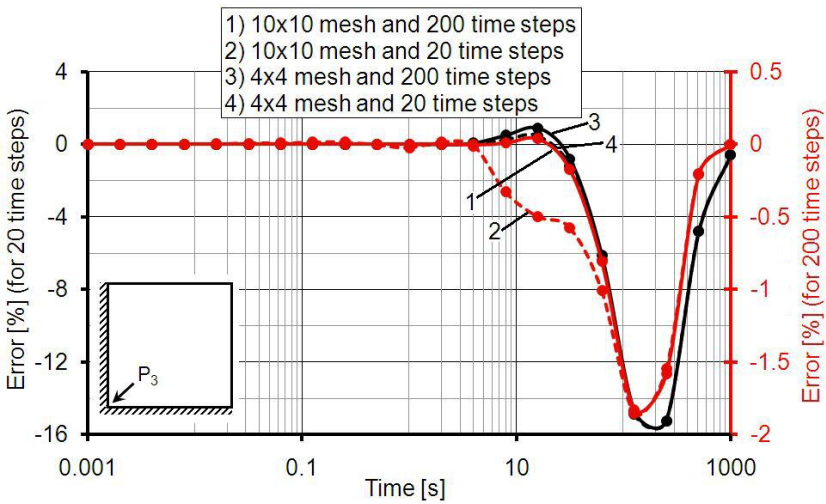
Figure 5.3: Error in computed temperature θ_2 on the mid-surface vs. timeFigure 5.4: Error in computed temperature θ_3 in the core vs. time

Table 5.1: Numerical values of temperature from analytical and numerical solutions in time

log(t)	Analytical Solution			Mesh=4x4, nt=20			Mesh=4x4, nt=200			Mesh=10x10, nt=20			Mesh=10x10, nt=200		
	θ_1	θ_2	θ_3	θ_1	θ_2	θ_3	θ_1	θ_2	θ_3	θ_1	θ_2	θ_3	θ_1	θ_2	θ_3
-3.0	995.0	997.5	1000.0	999.8	999.9	1000.0	999.8	999.9	1000.0	999.5	999.8	1000.0	999.5	999.8	1000.0
-2.4	990.1	995.0	1000.0	999.2	999.6	1000.0	999.2	999.6	1000.0	998.1	999.1	1000.0	998.1	999.0	1000.0
-1.8	980.5	990.2	1000.0	997.0	998.5	1000.0	997.0	998.5	1000.0	992.8	996.4	1000.0	992.7	996.3	1000.0
-1.2	961.7	980.6	1000.0	988.4	994.1	999.9	988.2	994.0	999.9	975.8	987.8	1000.0	974.9	987.3	1000.0
-0.6	926.3	962.1	1000.0	959.4	979.3	999.9	958.0	978.6	999.9	936.6	967.5	1000.0	935.2	965.7	1000.0
0.0	862.5	927.5	1000.0	888.2	941.4	1000.1	881.6	938.1	1000.2	870.9	931.9	1000.0	865.4	929.1	1000.0
0.6	758.8	866.8	999.9	775.2	875.8	999.8	784.4	870.1	1000.0	769.8	872.4	999.2	760.4	867.6	999.9
1.2	615.9	757.0	960.9	633.0	766.7	956.5	618.7	760.5	965.7	631.7	764.4	952.3	617.9	758.2	960.8
1.8	446.6	524.7	644.4	467.3	553.9	685.6	449.4	529.0	650.9	466.8	552.9	683.7	448.9	528.2	649.8
2.4	309.1	313.9	321.3	328.9	345.8	370.2	311.2	317.1	326.2	329.9	345.8	370.2	311.2	317.2	326.4
3.0	300.0	300.0	300.0	300.8	301.2	301.8	300.0	300.0	300.0	300.8	301.2	301.8	300.0	300.0	300.0

The temperature variation between center P_3 and middle of the surface P_2 after 100.6 s is discussed in Fig. 5.5 for different mesh densities and time step sizes. The analytical results and finite element results are also listed in Table. 5.2 for convenience. In the coarse mesh, the positions of the observation points are located inside the element, and the temperature values are interpolated from the nodal values. Therefore, the dashed lines are sinusoidal. For the fine mesh, the position of observation points match to finite element node positions and no interpolation is necessary. Therefore, the solid lines are smooth.

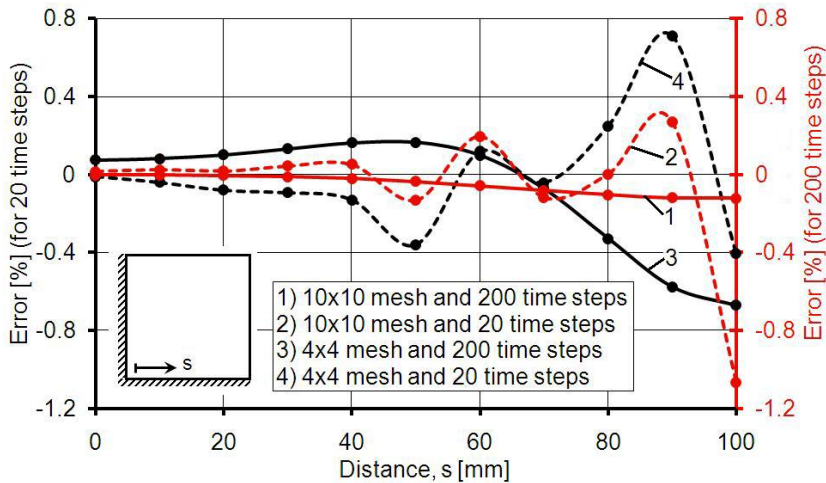
Figure 5.5: Error in computed temperature θ between the core and mid-surface

Table 5.2: Numerical values of temperature from analytical and numerical solutions in space

s [mm]	Temperature [K] when $\log(t)=0.6$					Error [%] in computation			
	Anal. Soln.	4x4 n=20	10x10 n=20	4x4 n=200	10x10 n=200	4x4 n=20	10x10 n=20	4x4 n=200	10x10 n=200
0	999.9	999.8	999.2	1000.0	999.9	0.01	0.07	-0.01	0.00
10	999.9	999.7	999.1	1000.3	999.9	0.02	0.08	-0.04	0.00
20	999.7	999.5	998.7	1000.5	999.8	0.02	0.10	-0.08	-0.01
30	999.2	998.7	997.9	1000.1	999.3	0.04	0.13	-0.09	-0.01
40	997.8	997.3	996.2	999.1	998.0	0.05	0.16	-0.13	-0.02
50	994.5	995.8	992.8	998.1	994.8	-0.13	0.16	-0.36	-0.04
60	987.5	985.5	986.5	986.3	988.0	0.19	0.10	0.12	-0.06
70	974.1	975.3	974.8	974.5	974.9	-0.12	-0.07	-0.04	-0.08
80	951.3	951.3	954.4	948.9	952.3	0.00	-0.33	0.25	-0.10
90	916.0	913.5	921.3	909.5	917.1	0.27	-0.58	0.71	-0.12
100	866.6	875.8	872.4	870.1	867.6	-1.07	-0.67	-0.41	-0.12

5.3 Validation of phase transformation formulation

Both diffusional and martensitic transformations are considered in this formulation. At higher temperatures, austenite converts into ferrite/pearlite/bainite by diffusional phase transformation. However, below the martensite start temperature, the martensitic transformation takes place and retained austenite is converted into martensite. For the computation of diffusional transformations, a simple approximation is chosen which assumes that the new phase evolves linearly proportional to the time in the transformation range. The martensitic phase fractions are computed according to [KM59]. The described models are tested on a 100Cr6 steel, the IT curve and CCT curves of which are given as shown in Fig. 5.6. As expected, the CCT curve is shifted to later times and lower temperatures. However, the computed CCT curve is quite different from the data sheet CCT curve.

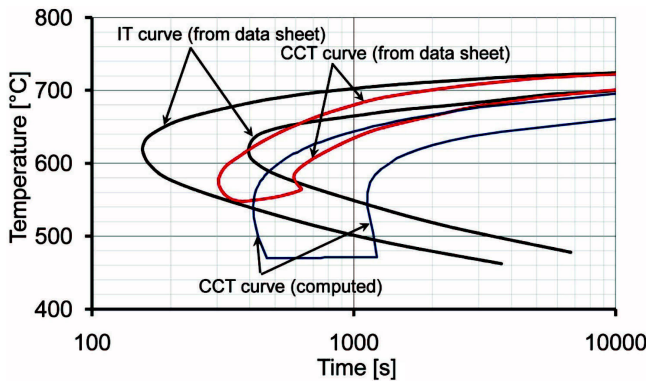


Figure 5.6: Comparison of IT diagram, computed CCT diagram and CCT diagram from the data sheet (provided by Saarlstahl [Fig. A.6 and Fig. A.7]), for the pearlitic transformation of a typical steel

Unlike diffusive transformations, the martensitic transformation depends

only on the temperature. The austenite is converted into martensite as the temperature drops below the martensite start temperature. The martensite start temperature M_S is $220\text{ }^\circ\text{C}$ and the transformation equation is assumed as

$$f_M = f_A (1 - \exp \{0.011 (\theta - M_S)\}) \quad (5.8)$$

where f_M is the martensite fraction at temperature θ and f_A is the austenite fraction at the beginning of transformation (it is cooled to $0\text{ }^\circ\text{C}$ temperature). Depending on the cooling rate, the final micro-structure becomes either diffusive or martensitic, or a mixture of them. It is shown in Fig. 5.7 that the variation of the final micro structure depends on the cooling rate. The black line represents the retained austenite. The blue line shows the martensite and red line shows the pearlite phase fraction. For slow cooling only pearlite forms, and for very high cooling only martensite occur and some of the austenite remains.

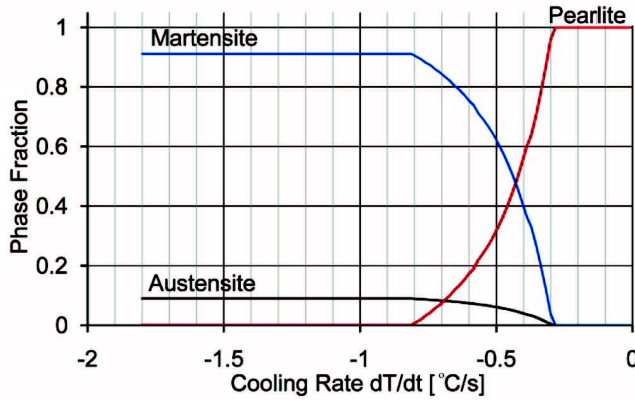


Figure 5.7: Variation of martensite fraction after the cooling depending on cooling time

5.4 Validation of displacement field formulation

Analytical solutions of stress equilibrium equation are known only for simple geometries and simple boundary conditions. The simplest case is a uniform stress-strain field in a rectangular domain. A simple patch tests is suggested in [Bat96]. Consider a $10\text{ m} \times 10\text{ m}$ plate with 1 m thickness which is shown on the left side of Fig. 5.10. The x -displacement on the left boundary is restricted and a uniform traction, which is increased up to 1.5 Pa , is applied on the right boundary. Such boundary conditions produce a uniform stress distribution in the x -direction over the domain. A bilinear elasto-plastic material model with isotropic hardening is assumed as shown on the right side of Fig. 5.8. The finite element computation result of this 2D-patch test is compatible with the analytical results and the finite element code has a good convergence characteristic for the plastic loading. It converges to solution only after 4 iterations.

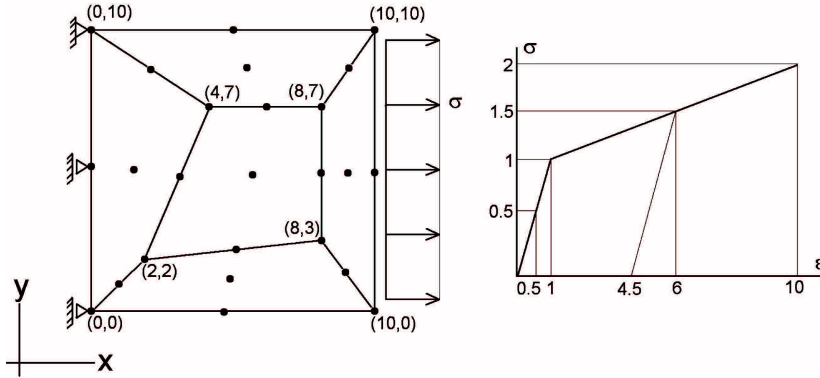


Figure 5.8: Patch test problem with its mesh and material model

5.5 Comparison with experimental results

5.5.1 Necessity of experiments

The system of coupled differential equations is too complicated to have an analytical solution. It is only possible to solve it by using numerical methods. The correctness of the developed numerical method can be tested by comparing the numerical results with experimental results or by comparing them with numerical results from commercial software, the correctness of which has already been tested. The correctness of the mathematical model described in chapter 3 and its finite element implementation is validated by experimental results from cooling of shafts and disks which are shown in Fig. 5.9. The experiments have been carried out in Bremen University, Germany and published in [BSO⁺05, BSO⁺06].

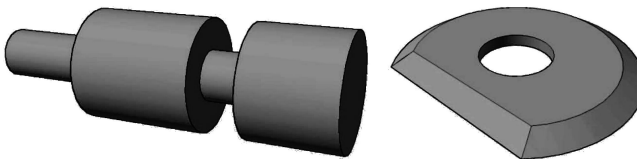


Figure 5.9: Geometry of notched shaft and disk

The phase fractions were measured by the point analysis method [EH86] with an accuracy of 1% fraction. As a material, 100Cr6 was used because its material properties are well known and available with high accuracy as given in Tab. A.1 in appendix. Further details of the experiments can be found in [BSO⁺05, BSO⁺06].

5.5.2 Shaft with notches

Two sample geometries of the shafts have been used in the experiments. The geometrical dimensions of the samples are shown in Fig. 5.10. The samples

were heated up to austenization temperature $850\text{ }^{\circ}\text{C}$ and then quenched in a nozzle field. The heat transfer coefficient is known from Computational Fluid Dynamics (CFD) analysis.

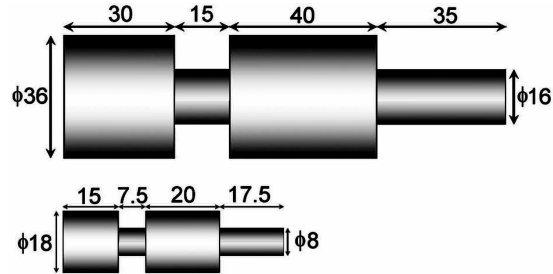


Figure 5.10: Geometrical dimensions [in mm] of big and small shaft

The calculated principal stresses are compared with the measured stresses for the bigger shaft in Fig. 5.11. The measurements were taken at 5 sampling points in longitudinal direction with a computer-controlled diffractometer.

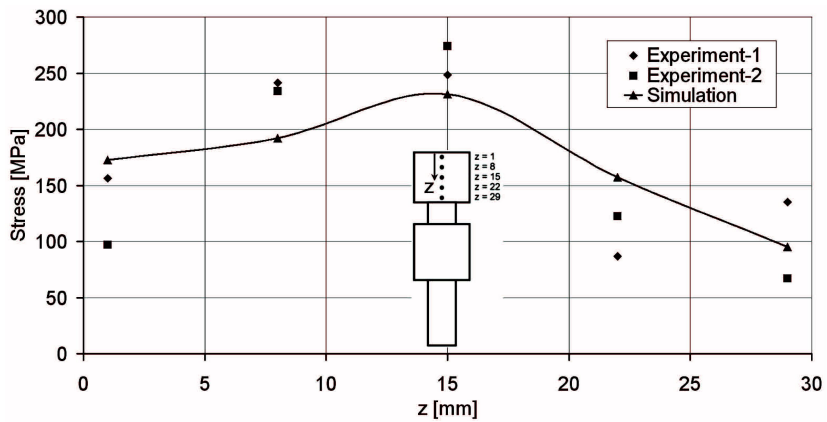
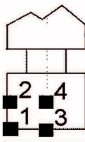


Figure 5.11: Calculated and measured values of stress at different positions [BSO+05, BSO+06]

The calculated and measured phase fractions for the shafts are presented in Table. 5.3 at 4 positions. There is no pearlite and mostly martensite formed in the small shaft since the cooling is faster for small pieces.

Table 5.3: Calculated and measured phase fractions for the shafts

	small shaft						big shaft					
	P [%]		B [%]		M [%]		P [%]		B [%]		M [%]	
	m	s	m	s	m	s	m	s	m	s	m	s
 p1	-	-	33	31	67	69	94	86	-	5	6	9
p2	-	-	33	31	67	69	97	86	-	9	3	5
p3	-	-	22	18	78	82	100	90	-	10	-	-
p4	-	-	26	22	74	78	100	89	-	11	-	-

P: pearlite, B: bainite, M: martensite, m:measured, s: simulated

The discrepancies with the computed and experimental phase fraction measurements are less than 10 %, which is acceptable for such simulations.

5.5.3 Disk with a hole

The disk has sharp edges and a hole as shown in Fig. 5.9. In the experiments two different sizes of cuttings disks were used: 90 mm and 120 mm of outer diameter. The dimension of the big disk is shown in Fig. 5.12. For the plane stress type of mathematical modeling, an equivalent disk is defined where the sharp edges are removed and corresponding boundary conditions are modified accordingly.

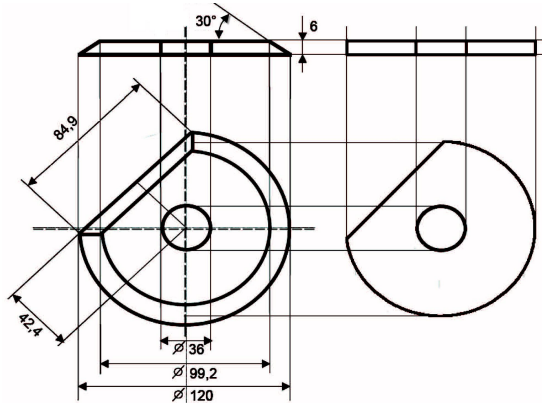


Figure 5.12: Actual dimensions of the disk with a hole and its idealization for modeling

The radial displacement of the hole in the center is measured. Since the geometry is not symmetric because of the linear edge of the disk, the central hole becomes oval after the cooling. This distortion behavior is very well captured by the simulations as well. The diameter from 0° to 180° is the minimum and the diameter from 90° to 270° is the maximum after the cooling. Note that the experimental measurements scatter more for the small disk since the measurements contains more relative error when the geometry is small (see Fig. 5.13). The measured phase fractions are given in Table. 5.4. For both disks, the austenite converts into bainite and martensite. The simulation overestimates the bainite fraction and underestimates the martensite fraction.

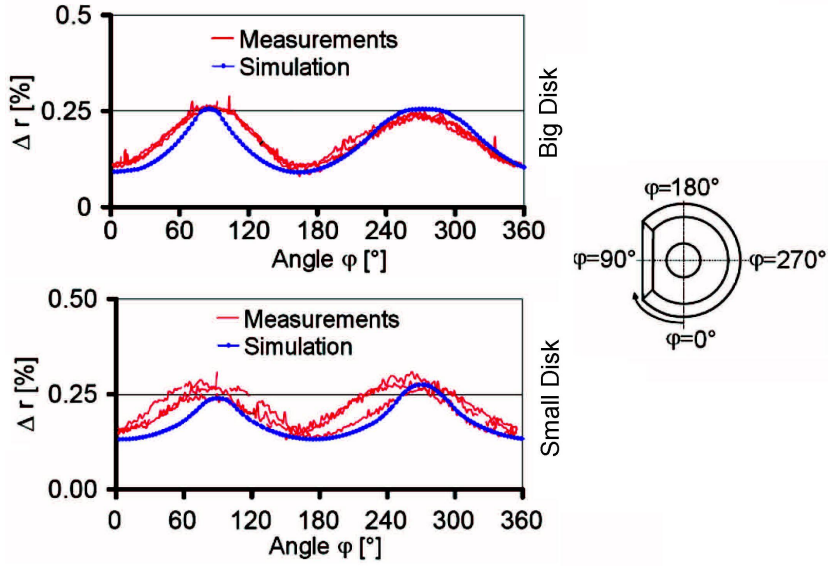



Figure 5.13: Comparison of experimental and calculated radial displacement of the hole for the big disk on the top and small disc on the bottom

Table 5.4: Calculated and measured phase fraction for the cutting disks

	small disk						big disk					
	P [%]		B [%]		M [%]		P [%]		B [%]		M [%]	
	m	s	m	s	m	s	m	s	m	s	m	s
p1	-	-	4	12	96	88	-	-	12	22	88	78
p2	-	-	5	18	95	82	-	-	16	30	84	70

P: pearlite, B: bainite, M: martensite, m: measured, s: simulated

5.6 Summary and conclusions

The correctness of the finite element formulations and their convergence characteristics were tested in this chapter. The individual parts of the model is tested by comparing the numerical results with the analytical solutions for very simple geometries and boundary conditions. The complete coupled field formulation was validated by comparing simulation results with experimental results. The developed model and its finite element implementation were proved to be correct. Hence, this tool can be used to find the optimum cooling strategy by performing simulations of quenching processes for varied boundary conditions which represent different cooling strategies.

Chapter 6

Simulation results

6.1 Introduction

This chapter is devoted to present all the obtained results of the simulation. Most of the simulations are carried out for long profiles which are made of different materials such as 100Cr6, C45, C80 and aluminum. Many simulations have been conducted to characterize the cooling behavior of the L120×12 profiles which are made of 100Cr6, C45, C80 and aluminum. The size effect has also been investigated by comparing the result from L60×6 and L180×18 aluminum profiles. A cooling range from 10 $W/m^2/K$ (i.e., free/furnace air cooling) to 4500 $W/m^2/K$ (i.e., water spray quenching) has been considered to figure out the effect of cooling intensity. The optimization study is performed only for the cooling regime with the highest distortion. Interestingly, it has been observed that the maximum distortion usually does not occur for the highest cooling.

There are also some simulation results for the disk with a hole which is made of 100Cr6. All the material properties used for the simulations are given in appendix A.1, A.2 A.3 and A.4. The main purpose of the simulations is to minimize the stresses and distortion simultaneously. In such an optimization process, the distortion and stress states should be both described by scalars. The distortion of the profiles is defined by its curvature. The distortion of the disk is indicated by the deviation of the central hole from the perfect circle. Expressing the whole stress state by a scalar value is quite difficult as the stress state is a tensor field quantity which is changing with position and cooling time. To overcome this difficulty, the stress tensor field is replaced by the effective stress field in order to reduce the tensor field to a scalar field. The volume average value and the maximum value of this effective stress field are used to characterize the total stress field. Lower average stress values are desirable with a maximum value which is small enough to prevent from crack formations. Different cooling strategies which lead to the optimum cooling, different material behaviors, the effect of size and geometry have been discussed in detail in the following sections. Also, the sensitivity of the computed distortion and stresses with respect to the material properties will be discussed at the end.

6.2 L profiles made of 100Cr6

Initially a series of simulations with equal Heat Transfer Coefficients (HTC) ranging from $10 \text{ W/m}^2/\text{K}$ to $4500 \text{ W/m}^2/\text{K}$ has been performed to find out the critical cooling regions. The L profile investigations are started with an $L120 \times 12$ profile made of 100Cr6 steel. The computed final distortion, average effective stress and the maximum effective stress are plotted against the equal HTC α in Fig. 6.1. The highest distortion occurs for a HTC value of $700 \text{ W/m}^2/\text{K}$. The highest value of stresses occurs for the most intensive cooling.

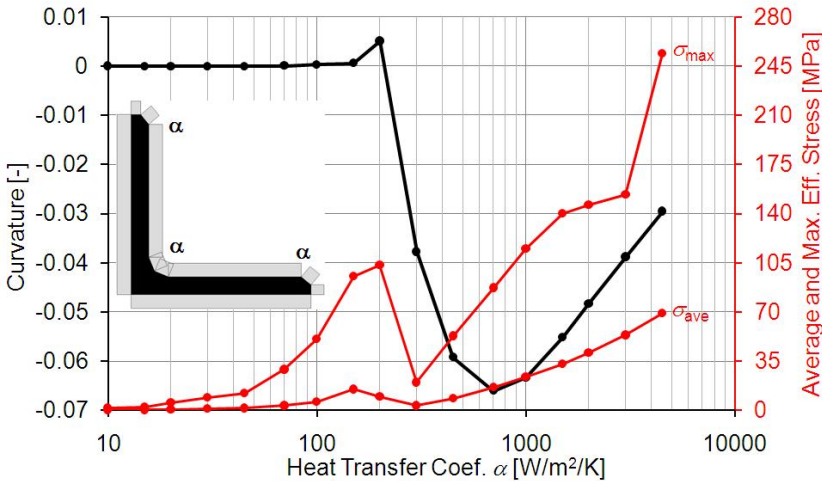


Figure 6.1: Distortion, average and max. residual stress vs. HTC α (100Cr6, L profile)

The average temperatures and the temperature difference between the hottest and coldest point is very important in a heat treatment process. There is usually a limitation for the maximum temperature difference value to control the micro-structure distribution, limit the maximum stress values and to prevent the formation of cracks. The variation of the average temperatures and the maximum temperature difference in time is plotted in Fig. 6.2, for the lowest cooling by $10 \text{ W/m}^2/\text{K}$, the highest distortion cooling by $700 \text{ W/m}^2/\text{K}$ and the highest cooling $4500 \text{ W/m}^2/\text{K}$. The latent heat generation effect cannot be clearly observed in the highest cooling regime. However, it is obvious from the stationary temperature region during the phase transitions for the lowest cooling regime. As expected, the maximum temperature difference occurs in the highest cooling regime. The temperature difference is much smaller for the lowest cooling regime. During the phase transformations the temperature difference values get even smaller due to the latent heat effect.

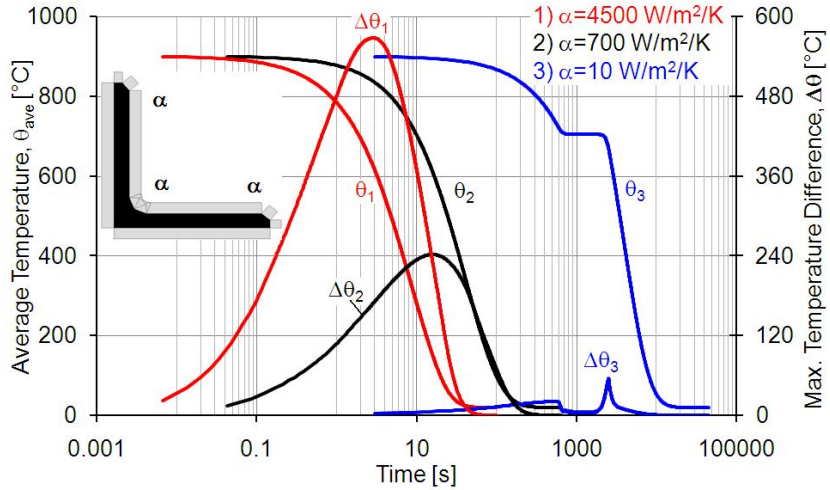


Figure 6.2: Average temperature and max. temperature difference vs. time for different HTC α (100Cr6, L profile)

The phase evolutions are also important since the final micro-structure identifies the material properties such as strength and ductility. The simulation results provide the fractions of each phase at each integration points. This phase field is replaced by a scalar which is just the fraction of the phase for the whole volume like the volume averaged effective stress. Three phases have been considered. Austenite is the parent phase. Pearlite and martensite are the product phases. The phase transition time ranges can be observed in Fig. 6.3. During low cooling, the austenite completely converts into pearlite as shown in Fig. 6.3. However, in the case of intensive cooling austenite may also convert into martensite, which provides the strength and hardness to the quenched steel.

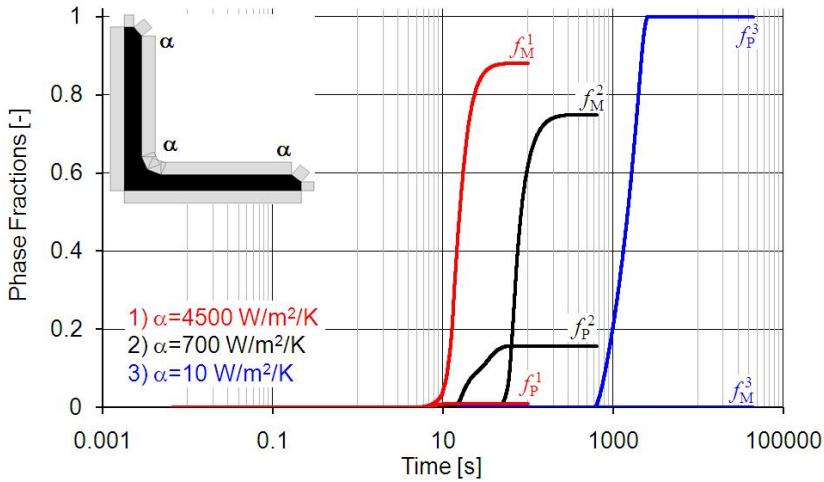


Figure 6.3: Phase fractions vs. time for different HTC α (100Cr6, L profile)

Figure 6.4 shows the evolution of the distortion during different cooling regimes as a function of time for 100Cr6 steel L profile. There is almost no distortion for the low cooling with $\alpha = 10 \text{ W/m}^2/\text{K}$. It is interesting to notice that the distortion when $\alpha = 700 \text{ W/m}^2/\text{K}$ is almost the double of that when $\alpha = 4500 \text{ W/m}^2/\text{K}$.

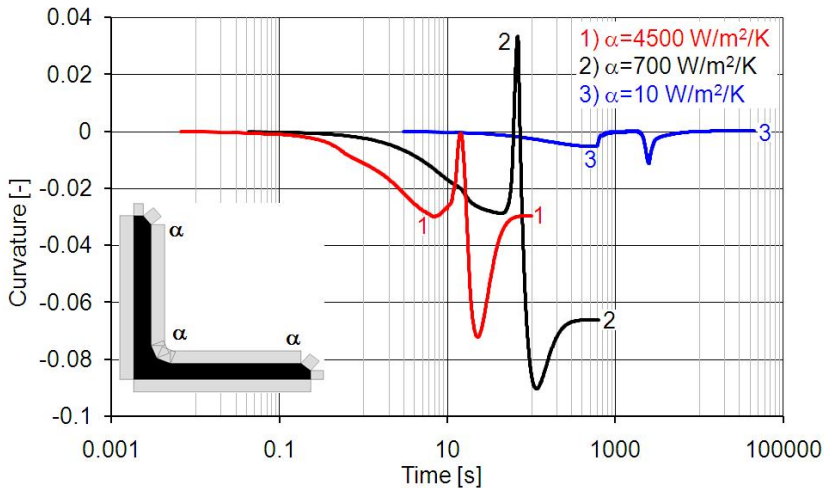


Figure 6.4: Distortion vs. time for different HTC α (100Cr6, L profile)

The distortion of the L profile can be better understood from Fig. 6.5, where the distorted shape of the profile is shown at different stages of cooling. Initially due to higher thermal shrinkage at the ends of the legs, the profile bends toward the legs. However, the ends of the legs soon undergo the phase transition which is also accompanied by a volume increase. Hence, the distortion

changes its direction. As the phase transition penetrates through the legs, the distortion again changes its direction and the profile bends toward the legs one more time. Finally, the phase transition is completed throughout the profile and the distortion gradually decreases as the temperature becomes uniform. However, a permanent deformation remains due to the mechanical yielding and transformation induced plasticity.

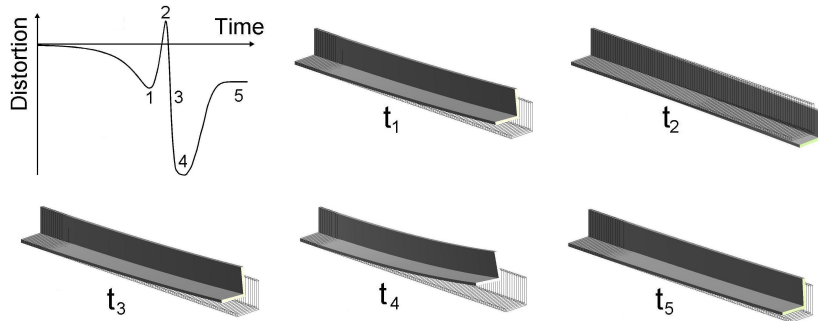


Figure 6.5: Distortion of L profile at different stages of cooling

Figure 6.6 shows the evolution of the average and the maximum effective stress during different cooling regimes as a function of time for the 100Cr6 steel L profile. The stresses have fluctuations during the phase transformations. The maximum stresses are observed in the intensive cooling range.

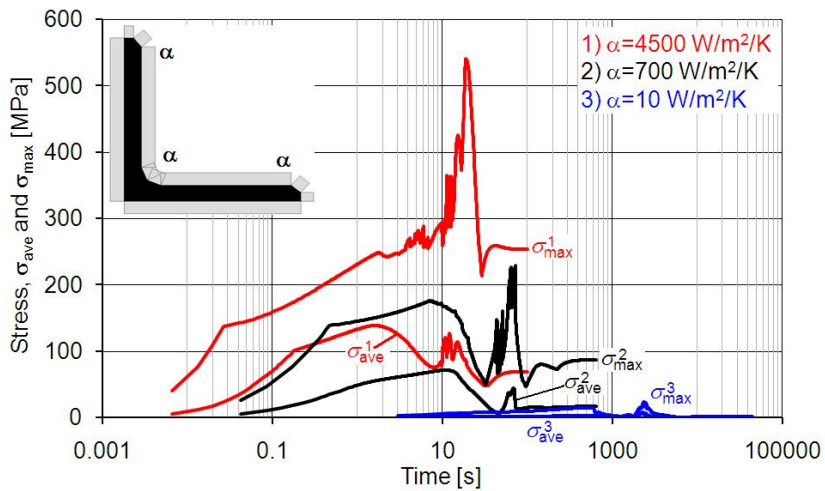


Figure 6.6: Average residual stress and maximum residual stress vs. time for different HTC α (100Cr6, L profile)

The highest distortion occurs for a homogeneous cooling with HTC $\alpha = 700 \text{ W/m}^2/\text{K}$ in the case of the 100Cr6 L120 \times 12 profile. In order to reduce the distortion and stresses, the cooling can be optimized by increasing the cooling

at mass-lumped regions of the profile and by reducing the cooling at the ends of the legs. The HTC at the mass-lumped regions is designated by α_1 , and it is designated by α_2 at ends of the legs. By increasing the value of α_1 and reducing the α_2 , it is intended to avoid the distortion and at the same time it is tried to reduce the average and maximum effective stress values. Fig. 6.7 shows the variation of the distortion and the average effective stresses for varying HTC α_1 .

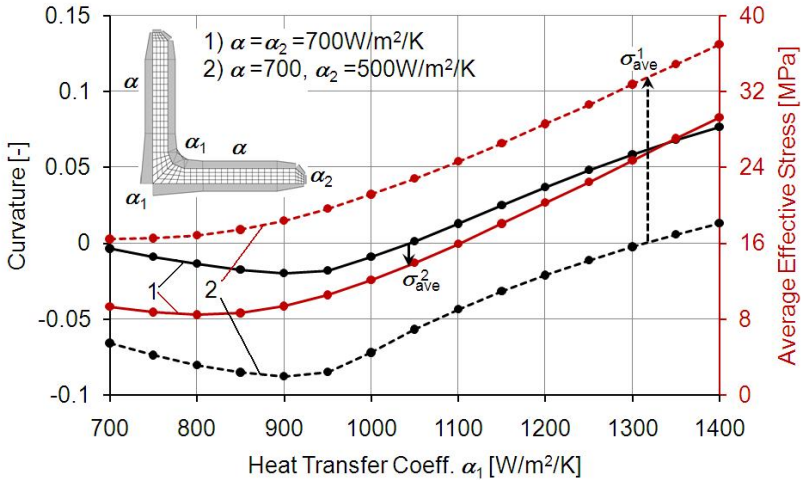


Figure 6.7: Distortion and average residual stress vs. HTC α_1 at mass lumped region (100Cr6, L profile)

The evolution of the average temperature and the maximum temperature difference for the equal cooling and optimum cooling is plotted in Fig. 6.8 to evaluate the characteristics of the optimum cooling as compared to equal cooling. Although the average temperature evolutions are almost the same for both types of cooling, the maximum temperature difference is lower in the case of optimum cooling. The lower temperature difference provides less thermal stresses and the occurrence of a more uniform phase transition with less transformation stresses. Similar to the average temperature evolution, the martensite and pearlite phase evolutions are also almost the same as shown in Fig. 6.9. Only in the case of optimum cooling, the phase transition time range is a little bit smaller than that of equal cooling.

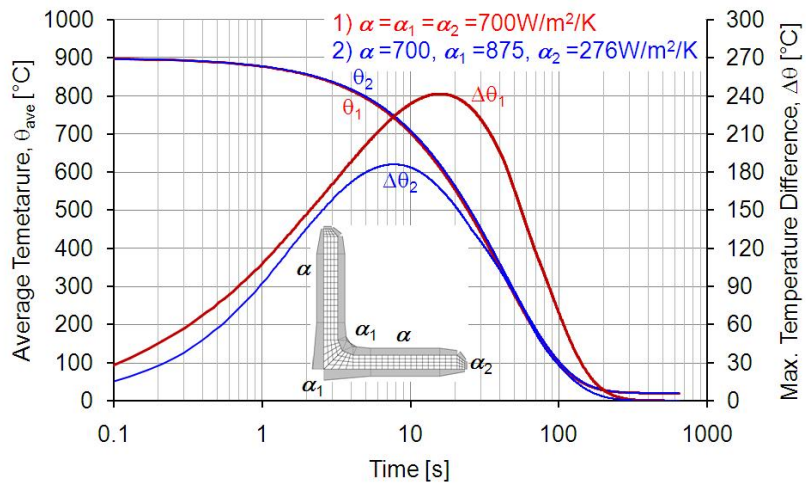


Figure 6.8: Average temperature and max. temperature difference vs. time for different cooling strategies (100Cr6, L profile)

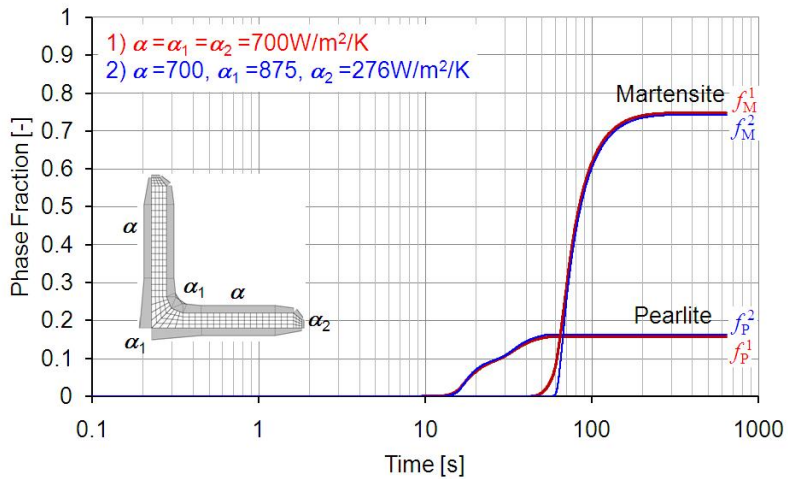


Figure 6.9: Phase fractions vs. time for different cooling strategies (100Cr6, L profile)

Although, the average temperature and phase fraction evolutions are very similar for the equal and optimized cooling, the evolutions of stresses and distortions are completely different. In the case of optimized cooling, the distortion is much smaller during the cooling and it is finally eliminated as shown in Fig. 6.10.

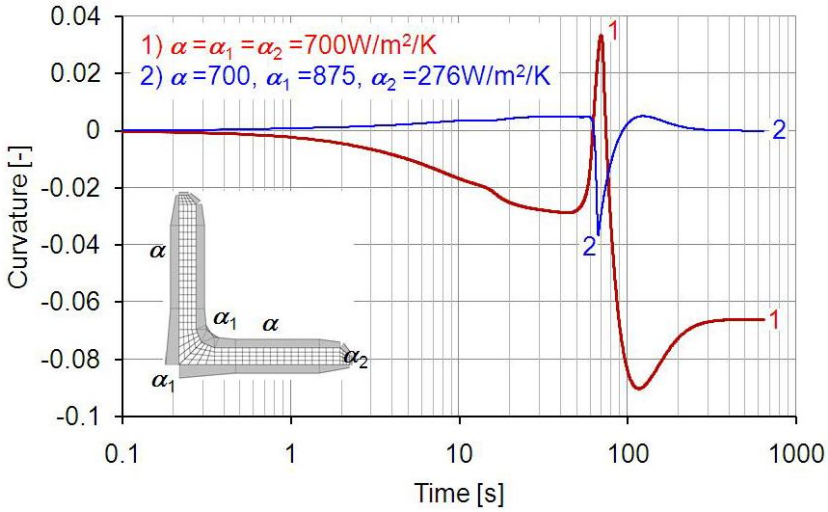


Figure 6.10: Distortion vs. time for different cooling strategies (100Cr6, L profile)

The evolutions of the average and maximum effective stresses for the equal cooling and optimum cooling are plotted in Fig. 6.11. The final maximum effective stress is reduced approximately from 87.2 MPa to 24 MPa. Similarly, the average effective stress is reduced from 16.4 MPa to 10.1 MPa. During the phase transformation the maximum effective stress fluctuates a lot due to the transformation induced plasticity.

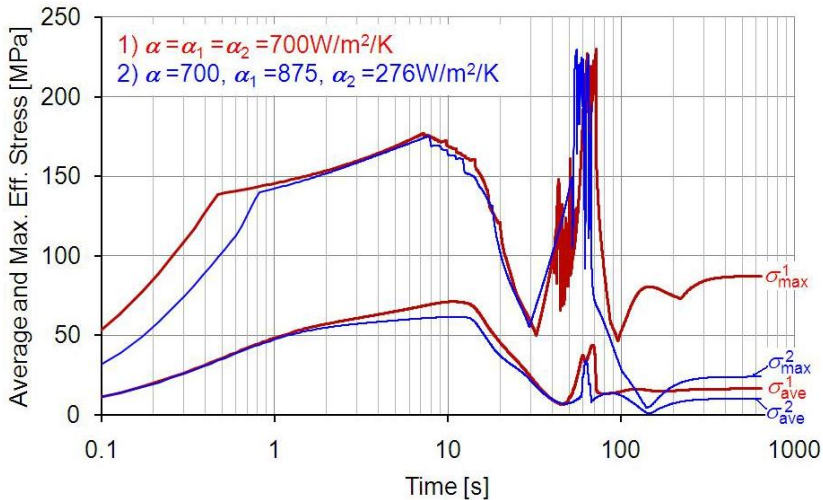


Figure 6.11: Average temperature and max. temperature difference vs. time for different cooling strategies (100Cr6, L profile)

6.3 L profiles made of C80

Many simulations have been performed for the L120×12 profile made of C80 to find out the cooling characteristics. Initially a series of simulations with a homogeneous HTCs ranging from 10 to 4500 $W/m^2/K$ has been performed to find out the critical cooling regions. The computed distortion and average effective stress are plotted in Fig. 6.12. The highest distortion occurs for the HTCs 100 and 3000 $W/m^2/K$. However, the highest value of the stresses occurs for the HTCs 20 and 450 $W/m^2/K$. The evolutions of temperature, phase fractions, distortion and stresses in time will be discussed in the following figures for the HTCs 20, 100 and 3000 $W/m^2/K$ in order to characterize the cooling behavior of the L profile made of C80.

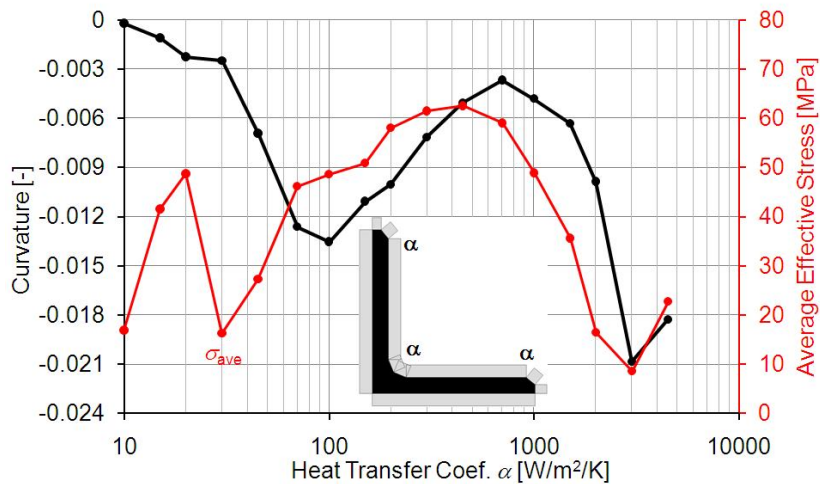


Figure 6.12: Average residual stress and maximum residual stress vs. time for different cooling strategies (C80, L profile)

The evolutions of the average temperatures and maximum temperature difference in time are plotted in Fig. 6.13 for three critical HTCs of 20, 100 and 3000 $W/m^2/K$. The latent heat generation effect can be clearly observed in Fig. 6.13 by the stationary temperature for the low cooling with $\alpha = 20 W/m^2/K$. The temperature difference between the hottest and coldest point is very high for the intensive cooling with $\alpha = 3000 W/m^2/K$.

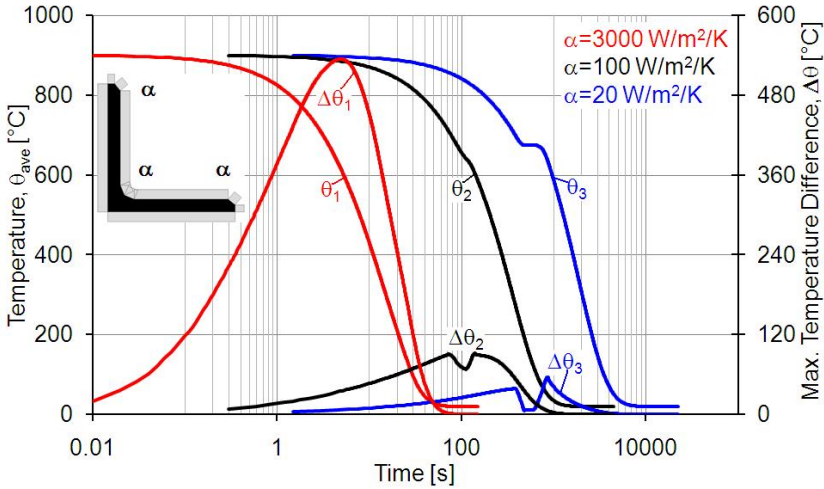


Figure 6.13: Average temperature and max. temperature difference vs. time for different HTC α (C80, L profile)

During the low cooling, the austenite completely converts into pearlite as shown in Fig. 6.14. However, in the case of intensive cooling, the austenite can also convert into martensite, which provides the strength and hardness to quenched steel. Because of the limitation of the Koistinen-Marburger equation, a small amount of austenite retains after the martensitic transformation as observed in Fig. 6.14. The sum of the phase fractions f_P and f_M is less than unity (the remaining part is austenite).

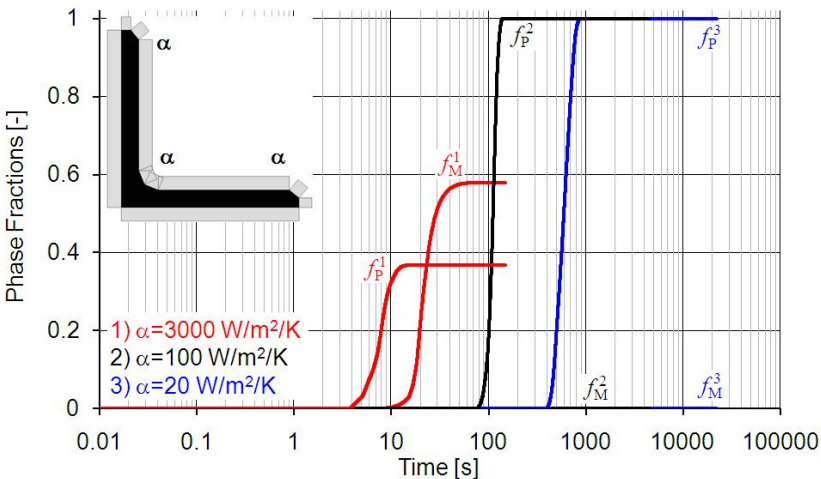


Figure 6.14: Phase fractions vs. time for different HTC α (C80, L profile)

The resulting distortions are compared in Fig. 6.15 for these three cooling regimes. During the phase transition, the direction of the distortion changes

and reaches its maximum value. Although the largest distortion occurs for the equal cooling with a HTC value of $3000 \text{ W/m}^2/\text{K}$, the residual stresses are much smaller as compared to other cooling regimes. The evolutions of the average and maximum effective stresses are plotted in Fig. 6.16. For the intensive cooling case, the residual stresses are very small since both the martensitic and the diffusive phase transitions take place with a small time shift due to large temperature gradient ($> 500 \text{ }^\circ\text{C}$). During the martensitic transformation, the high stresses relax by the TRIP. For the other cooling regimes only a diffusive transformation takes place. Therefore, during the phase transition the stress reaches its maximum and does not reduce afterward.

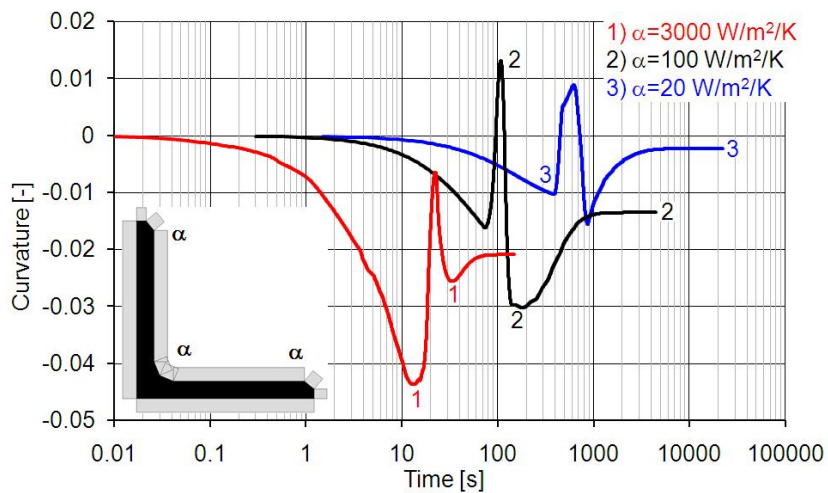


Figure 6.15: Distortion vs. time for different HTC α (C80, L profile)

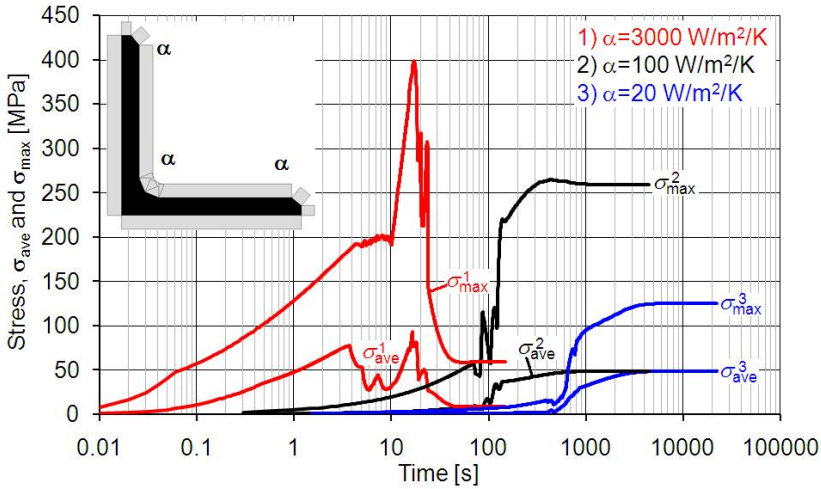


Figure 6.16: Average residual stress and maximum residual stress vs. time for different HTC α (C80, L profile)

6.4 L profiles made of C45

A series of simulations with uniform HTCs ranging from 10 to 4500 $W/m^2/K$ have been carried out for the L120 \times 12 profiles made of C45 steel. The effect of cooling on the distortion and residual stresses are shown in Fig. 6.17. For very low cooling (i.e., $\alpha = 10 W/m^2/K$), there is almost no distortion. However, the distortion rapidly increases and reaches its maximum value at a HTC $\alpha = 100 W/m^2/K$. Further increase in the HTC reduces the distortion gradually. The relation between the average residual stress and the HTC α is more complicated. Interestingly, the highest stresses are observed for the lowest cooling. This strange behavior can be explained by the strong phase transformation characteristics of C45. With increasing HTC, the stresses rapidly reduce and has a minimum at $\alpha = 30 W/m^2/K$ and then it increases and has a local maximum at $\alpha = 150 W/m^2/K$. Then it reduces again and has its second minimum at $\alpha = 2000 W/m^2/K$. After this point, the residual stresses increase with increasing HTC α .

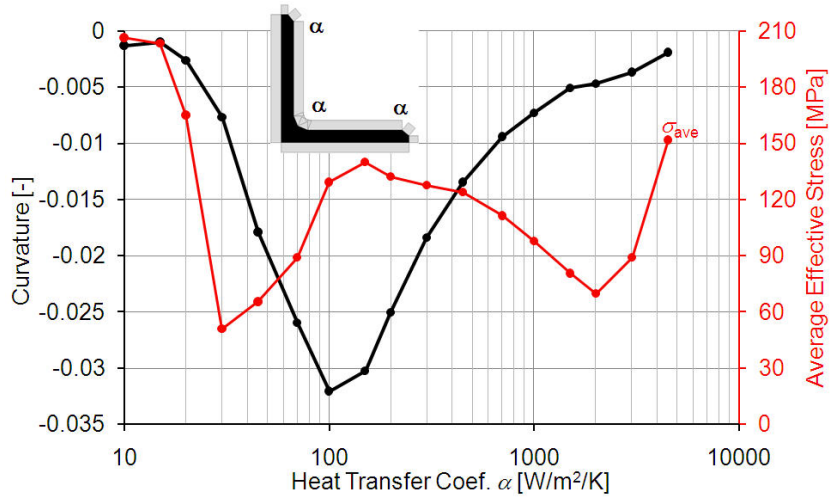


Figure 6.17: Distortion and average residual stress vs. HTC α (C45, L profile)

The variation of the average temperatures and the maximum temperature difference in time is plotted in Fig. 6.18 for the HTCs: 10, 100 and $4500 W/m^2/K$. The stationary temperature region during the cooling with $\alpha = 10 W/m^2/K$ is due to the phase transformation latent heat generation. For the cooling with a HTC $\alpha = 100 W/m^2/K$ the temperature difference between the hottest and coldest point is slightly reduced due to the latent heat generation. For the highest cooling ($\alpha = 4500 W/m^2/K$) the temperature difference between the hottest point and coldest point is very high since the heat conduction in the steel is relatively poor (i.e., aluminum has a higher conductivity and would have a smaller temperature difference).

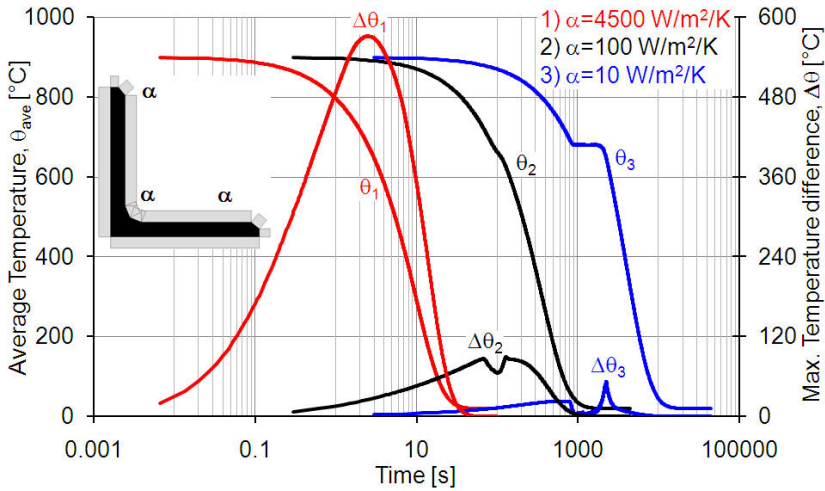


Figure 6.18: Average temperature and max. temperature difference vs. time for different HTC α (C45, L profile)

C45 is a pearlitic steel. Even at very high quenching rates, only pearlite forms. Austenite is completely converted into pearlite as shown in Fig. 6.19 for any intensity of cooling. As the cooling rate increases, a finer pearlitic micro structure is obtained.

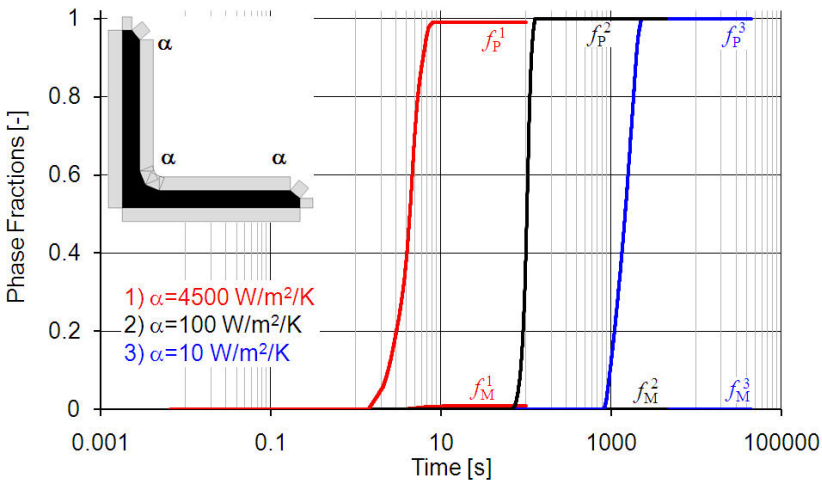


Figure 6.19: Phase fractions vs. time for different HTC α (C45, L profile)

The variations of the distortion in time are plotted in Fig. 6.20 for three different cooling intensities. At relatively low cooling rates ($\alpha \leq 100 \text{ W/m}^2/\text{K}$), the distortions change direction during the phase transformation. However, this phenomenon is not observed for the intensive cooling case. Therefore, the final distortion for the intensive cooling with $\alpha = 4500 \text{ W/m}^2/\text{K}$ is relatively small.

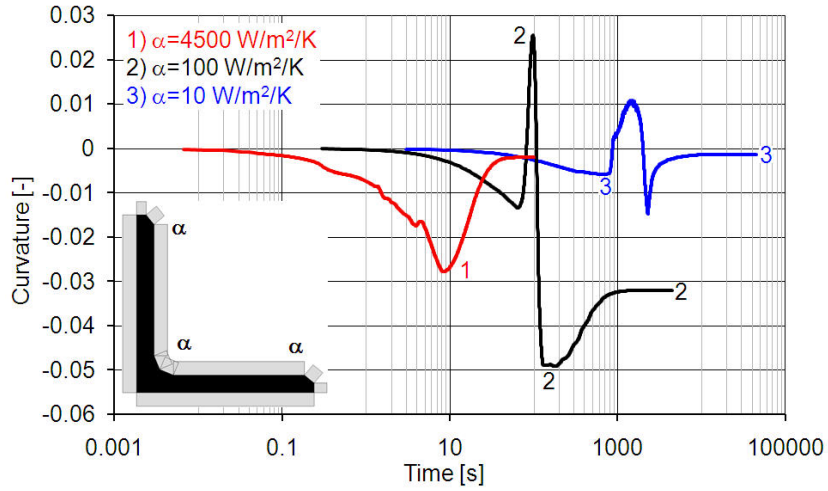


Figure 6.20: Distortion vs. time for different HTC α (C45, L profile)

The variations of stress in time are plotted in Fig. 6.21 for three different cooling intensities. For all cooling cases, the average stress rapidly increases during the phase transformation. For the low cooling with $\alpha = 10 \text{ W/m}^2/\text{K}$, there is almost no stress before the phase transition, and all stresses suddenly develop during the phase transition. The final average effective stress values are more or less similar. However, the maximum effective stress evolutions are quite different. Very high maximum effective stresses are generated for the intensive cooling with $\alpha = 4500 \text{ W/m}^2/\text{K}$. On the other hand, for low cooling intensities ($\alpha = 10$ or $100 \text{ W/m}^2/\text{K}$) the maximum effective stresses have similar values.

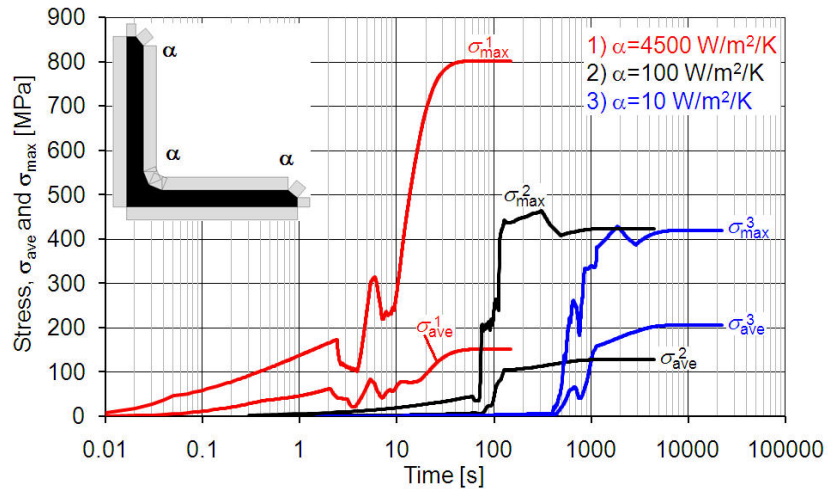


Figure 6.21: Average residual stress and maximum residual stress vs. time for different HTC α (C45, L profile)

6.5 Mesh convergence test

In finite element modeling, a finer mesh and small time steps typically result in a more accurate solution. However, a finer mesh comes with a cost of more computational time and large memory requirements since the number of unknowns are increased. When the time step size is reduced, the number of solutions to reach the state at a desired time increases. Therefore, a balance between accuracy and computing resources should be established. The question that always arises is: *How small do I need to make the elements and time step size before I can trust the solution?* In general there are no real firm answers on this. One way is to perform a mesh convergence study. The same problem is repeatedly solved by refining mesh and reducing the time step size until the results converge.

Mesh convergence tests have been performed for aluminum L120 profiles. Three different meshes have been considered as shown in Fig. 6.22. As the computer resources such as solution time and output file size are important characteristics of such a cooling simulation, they have been given in Tab. 6.1.

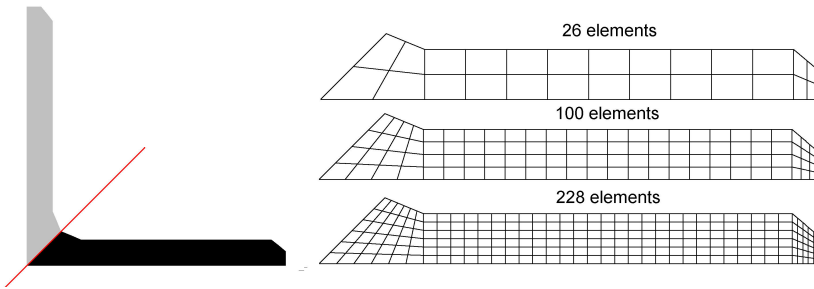


Figure 6.22: Three different meshes considered in the mesh convergence analysis (Aluminum, L profile)

Table 6.1: Required computer resources for different meshes and time steps

Number of elements	100 time steps		250 time steps		500 time steps		
	Solution time	Total output file size	Solution time	Total output file size	Solution time	Total output file size	
Coarse mesh	26	34s	2.0MB	76s	5.1MB	127s	10.3MB
Normal mesh	100	159s	7.5MB	379s	19.0MB	647s	38.3MB
Fine mesh	228	543s	16.7MB	1422s	42.5MB	2431s	85.9MB

The convergence characteristics of the developed finite element code is very good even for a very coarse mesh and large time stepping. This can be easily recognized from the computed distortion and average effective stress results. Although a very coarse mesh and large time stepping is enough for the distortion computation as shown in Fig. 6.23 and for the average stress computation as shown in Fig. 6.24, a relatively fine mesh is essential to capture the variation of the state variables over profile geometry. The computed distribution of the effective stress over the profile geometry is shown in Fig. 6.25 for three different

meshes. Note that for the coarse mesh the local variations are quite roughly captured.

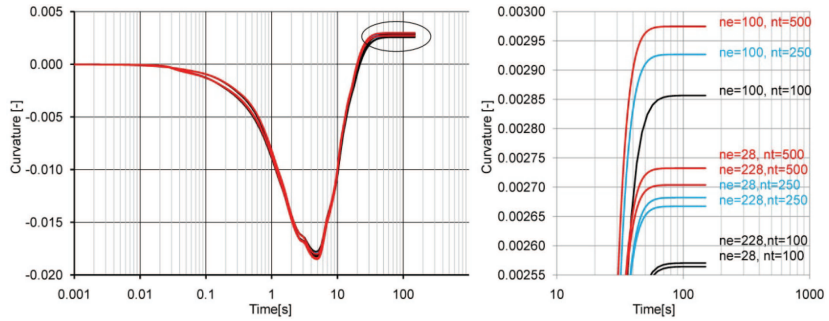


Figure 6.23: Distortion vs. time for different meshes and time steps (Aluminum, L profile)

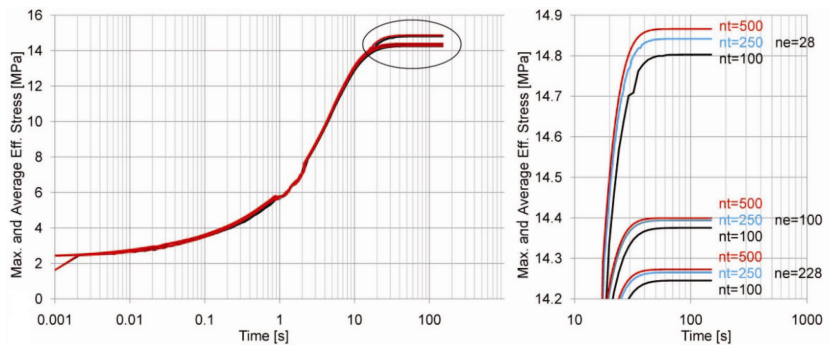


Figure 6.24: Maximum residual stress vs. time for different meshes and time steps (Aluminum, L profile)

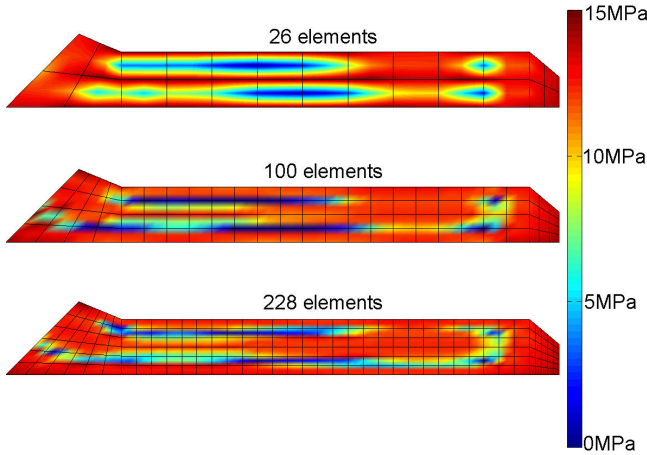


Figure 6.25: Contours of max. residual stress for different meshes (Aluminum, L profile)

6.6 Comparison of different sizes

The effect of profile size on the distortion and residual stresses are investigated for aluminum L profiles. Three different sizes, L60×6, L120×12 and L180×18, are considered in the simulations within a HTC range from 10 to 4500 $W/m^2/K$. The computed distortion and average effective stress for three different sizes of aluminum L profiles are plotted in Fig. 6.26 and in Fig. 6.27, respectively. The highest distortion and stresses occur for the highest HTC value of 4500 $W/m^2/K$. Interestingly, large aluminum profiles have a relatively higher distortion tendency after the cooling. Also, the average effective stress is apparently higher for large profile and lower for the small profile.

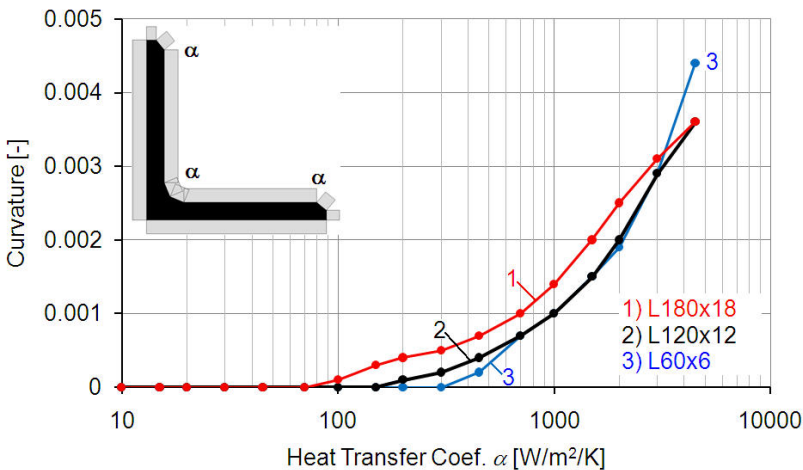


Figure 6.26: Distortion vs. HTC α for different sizes of Aluminum L profiles

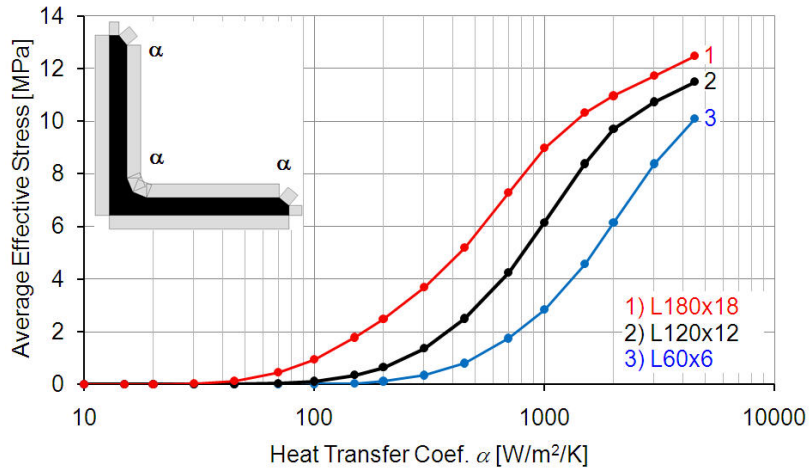


Figure 6.27: Average residual stress vs. HTC α for different sizes of aluminum L profile

A HTC value of $4500 \text{ W/m}^2/\text{K}$ causes the highest distortion and stresses in the considered cooling range. During the cooling the small profile has a higher maximum distortion and the large profile has smaller maximum distortion because of the smaller bending resistance of the small profile and the higher bending resistance of large profile. After the cooling, large profiles has more distortion due to higher plastifications.

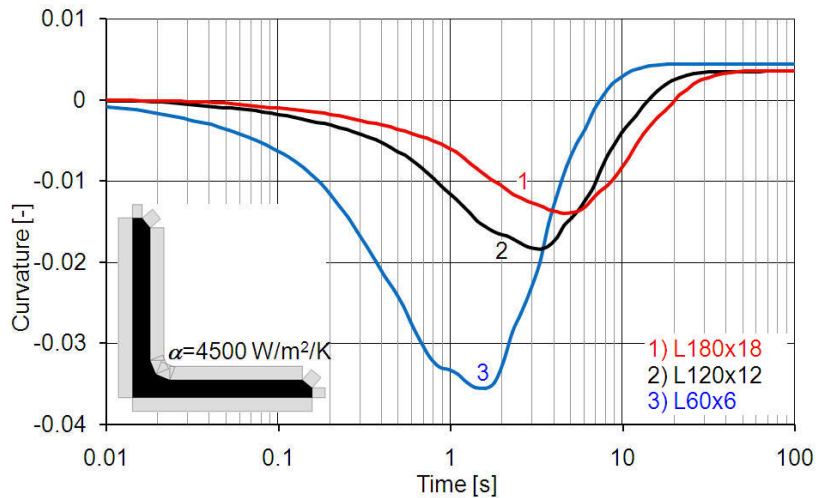


Figure 6.28: Distortion vs. time for different sizes of aluminum L profiles

The evolution of the average temperatures and maximum temperature differences in time are plotted in Fig. 6.29 for the HTC's of $4500 \text{ W/m}^2/\text{K}$. The large profile cools down slower and the temperature difference is higher whereas

the small profile cools down relatively faster with a small temperature difference.

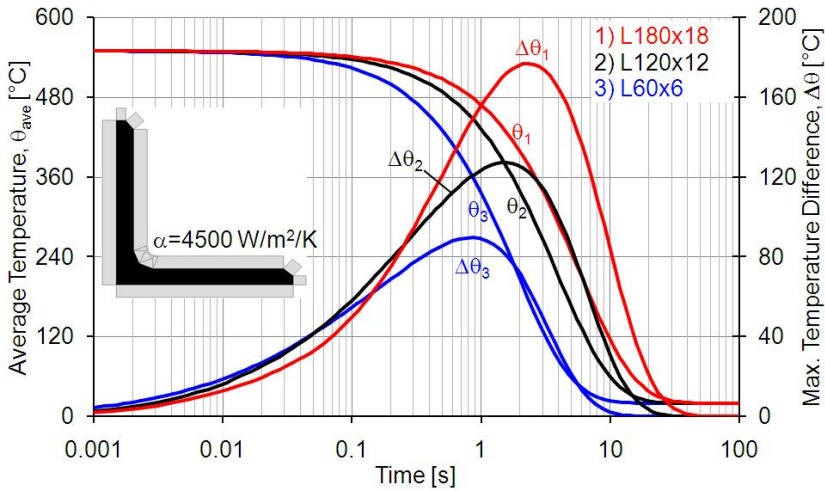


Figure 6.29: Average temperature and max. temperature difference vs. time for different sizes of aluminum L profiles

The evolution of the average and maximum effective stress in time is shown in Fig. 6.30 for the HTC's of $4500\text{ W/m}^2/\text{K}$. The large profile has the highest stresses due to higher temperature difference whereas the small profile has the lowest stresses.

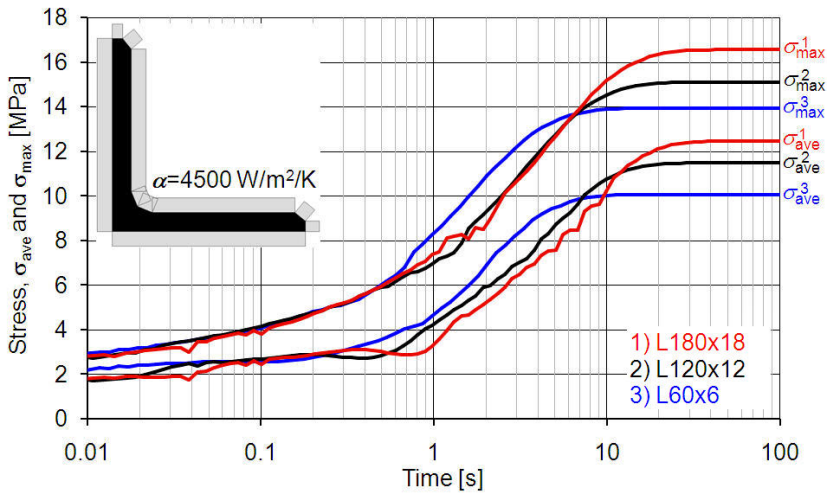


Figure 6.30: Average residual stress and max. residual stress vs. time for different sizes of aluminum L profiles

6.7 Comparison of different optimums

The distortion can be avoided and stresses can be reduced by a controlled cooling. The optimization analysis is carried out for the aluminum L120 profile which is homogeneously cooled with a HTC of $3000 \text{ W/m}^2/\text{K}$. The HTCs at the mass-lumped region of the profile (α_1) and at the ends of the legs (α_2) are varied in order to eliminate the distortion and reduce the maximum average effective stress after the cooling. The built-in optimization function $fmincon(\dots)$ in the Matlab is used and four local optimum cooling profiles have been obtained with different initial guesses. These local optimum cooling profiles are compared in Fig. 6.31. Increasing the cooling at the mass lumped regions and reducing the cooling at the leg ends produce relatively lower average effective stress values. However, in all cases the distortion is totally eliminated.

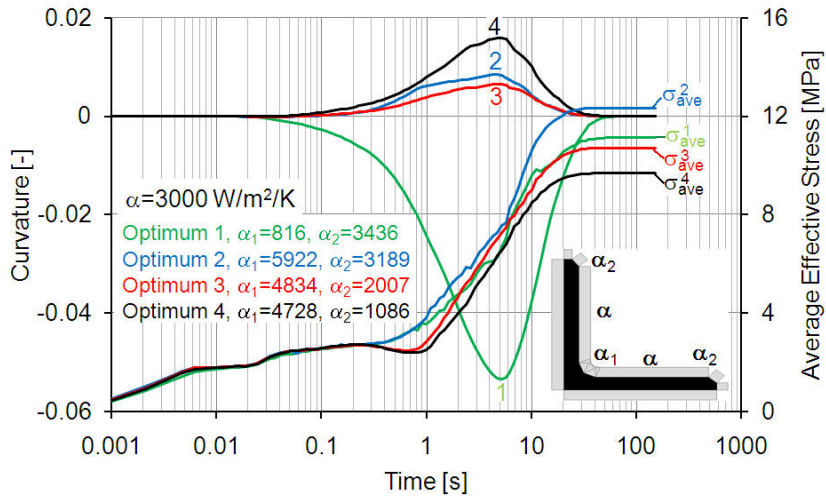


Figure 6.31: Distortion vs. time for different optimum coolings (Aluminum, L profile)

The axial stress distributions (Fig. 6.32) show the differences between these four optimum cooling profiles. The 1st optimum cooling profile is quite different from the other three since the cooling at the mass-lumped region is reduced. Such a heat transfer profile also produce a negative curvature evolution as seen in Fig. 6.31. The high plastic deformation in the reverse direction finally balances and ends up with no distortion. It is not a very preferable cooling strategy as the high plastic deformations may result in cracks.

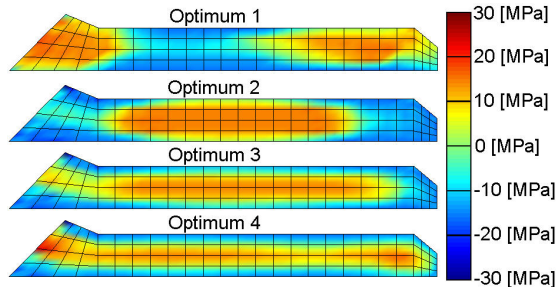


Figure 6.32: Contours of axial residual stress for different optimum coolings (Aluminum, L profile)

6.8 Comparison of different materials

The cooling behavior of 100Cr6, C45, C80 and aluminum is compared for L120×12 profiles. The most interesting result is the distortion vs. HTC for different materials. As shown in Fig. 6.33, the material behaviors are completely different. Surprisingly, the maximum distortion does not occur at high HTCs for phase changing metals. No distortion is observed in the 100Cr6 profiles up to $\alpha = 150 \text{ W/m}^2/\text{K}$ then suddenly the distortion increases till $\alpha = 700 \text{ W/m}^2/\text{K}$ has a maximum there and starts reducing for further increase of HTC. Steel C45 has a gradually increasing distortion in the low cooling range. The distortion obtains a maximum for a HTC $\alpha = 100 \text{ W/m}^2/\text{K}$. After this point the distortion gradually reduces with increasing HTC. Steel C80 has two maximum distortion regions at HTCs $\alpha = 100 \text{ W/m}^2/\text{K}$ and $\alpha = 3000 \text{ W/m}^2/\text{K}$. Between these two HTC values, the distortion is minimum when $\alpha = 700 \text{ W/m}^2/\text{K}$. Non-phase changing aluminum has much smaller distortion than phase changing steel alloys. The distortion of aluminum is only significant at very high heat transfer values.

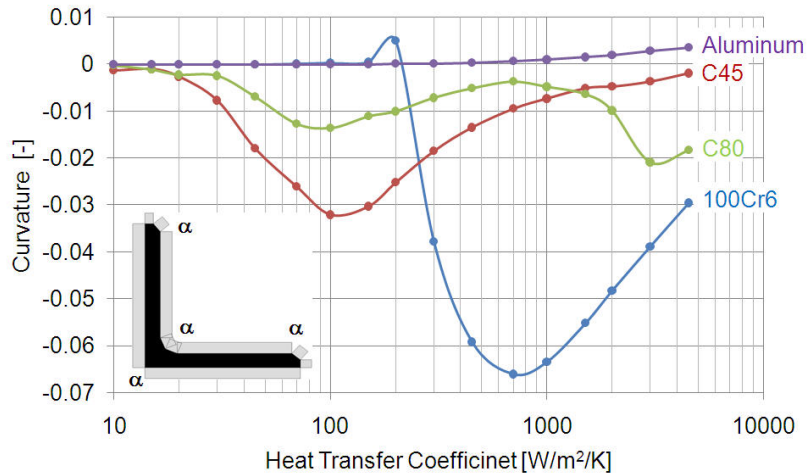


Figure 6.33: Distortion vs. HTC α for different materials (L profile)

6.9 T profiles made of aluminum

Similar simulations to those performed for aluminum L120 profiles have been carried out for aluminum T120×12 profiles. The purpose was to investigate the effect of the geometry on the distortion and stresses within the same cooling range, 10 to 4500 $W/m^2/K$ which is analyzed for L profiles. The computed final distortion, average effective stress and the maximum effective stress are plotted in Fig. 6.34. The distortion direction changes during the cooling when the HTC $\alpha = 100 W/m^2/K$. The highest distortion and stresses occur for a HTC value of 4500 $W/m^2/K$. The evolutions of temperature, distortion and stresses are investigated for the HTCs 45, 100 and 4500 $W/m^2/K$.

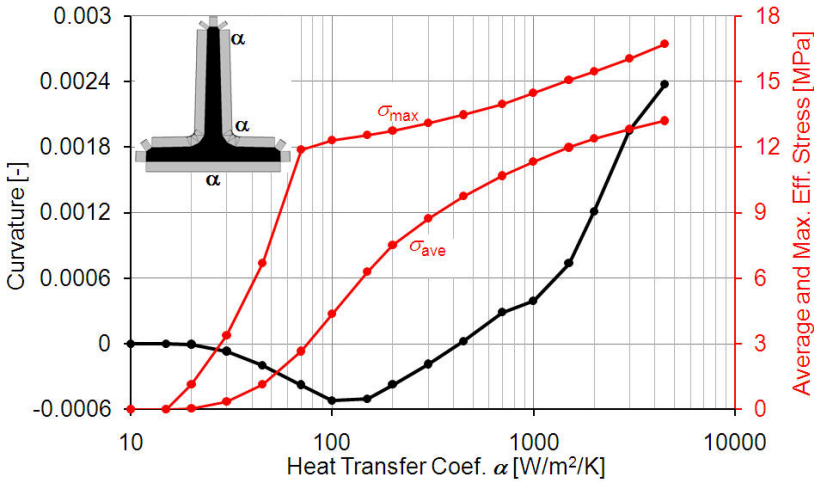


Figure 6.34: Distortion, average residual stress and max. residual stress vs. HTC α (Aluminum, T profile)

The evolution of the average temperatures and maximum temperature difference in time is illustrated in Fig. 6.35. The maximum temperature difference is much higher in the case of intensive cooling whereas it is relatively small for low coolings.

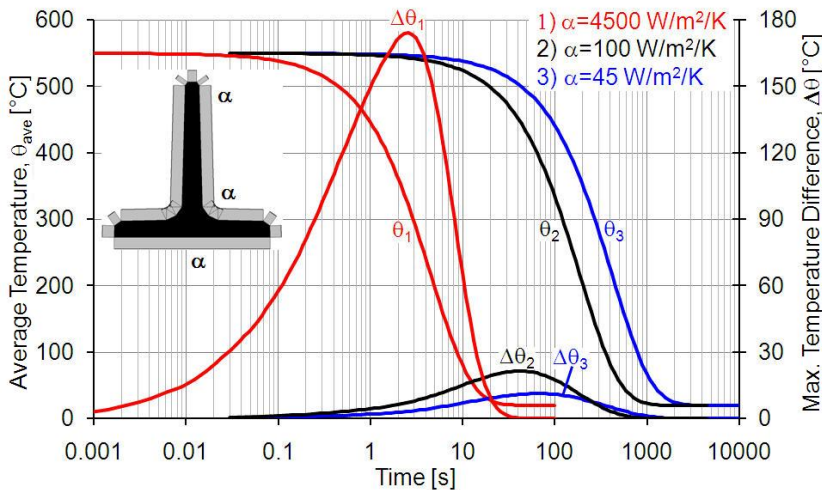


Figure 6.35: Average temperature and max. temperature difference vs. time for different HTC α (Aluminum, T profile)

The evolutions of the distortion and the stresses are compared for three different cooling intensities in Fig. 6.36 and Fig. 6.37, respectively. The distortion of the aluminum profiles is due to temperature gradient only. The bending of the profiles occurs about the natural axis of the cross section which is located

at the centroid. For the T profile, the natural axis is parallel to the flange. During a homogeneous cooling, the curvature is always negative in the beginning of the cooling since the mass lumped region is located below the natural axis. However, the final distortion direction is more difficult to estimate by only using simple rules. Depending on the cooling intensity it may obtain a positive or negative curvature.

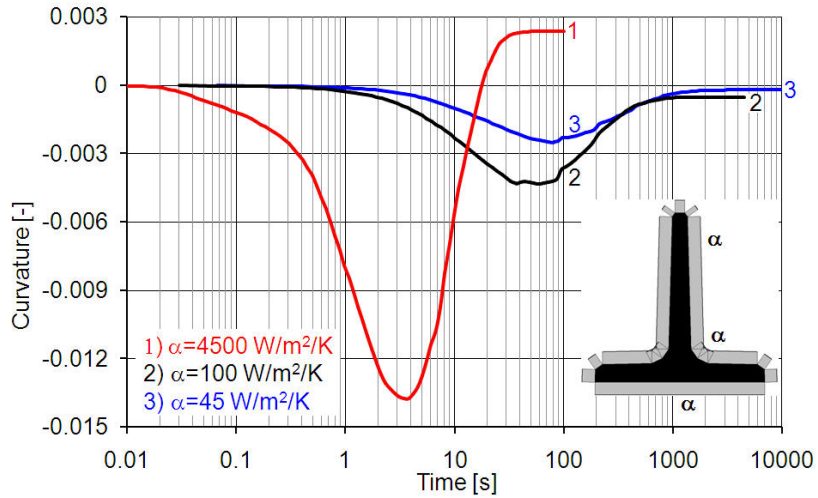


Figure 6.36: Distortion vs. time for different HTC α (Aluminum, T profile)

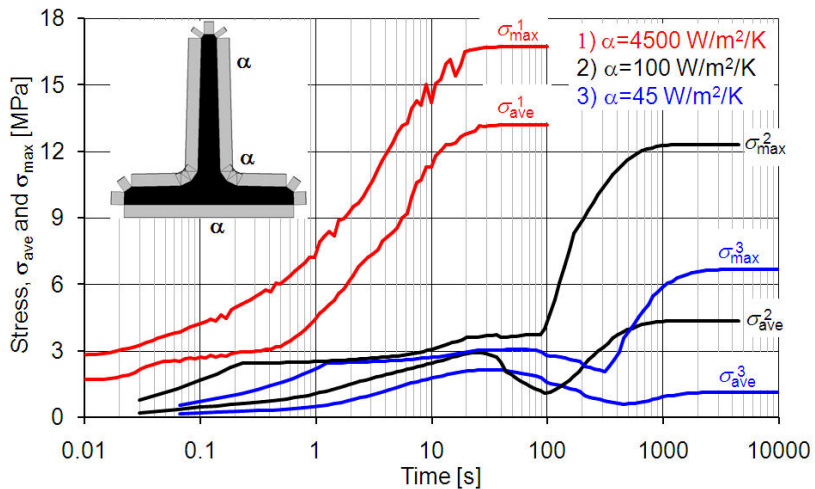


Figure 6.37: Average residual stress and max. residual stress vs. time for different HTC α (Aluminum, T profile)

The highest distortion occurs for the homogeneous cooling with a HTC of $4500 \text{ W/m}^2/\text{K}$ in the case of the aluminum T120 profile. In order to reduce the

distortion and stresses, the cooling can be optimized by increasing the cooling at the mass-lumped regions of the profile and by reducing the cooling at the ends of the legs. The HTC at the mass-lumped regions is designated by α_1 and it is designated by α_2 at ends of the legs. By increasing the value of α_1 and reducing the α_2 , it is intended to avoid the distortion and at the same time the average and maximum effective stress value are intended to be reduced. The distortion is avoided and internal stresses are minimized when $\alpha_1 = 5426 \text{ W/m}^2/\text{K}$ and $\alpha_2 = 3003 \text{ W/m}^2/\text{K}$.

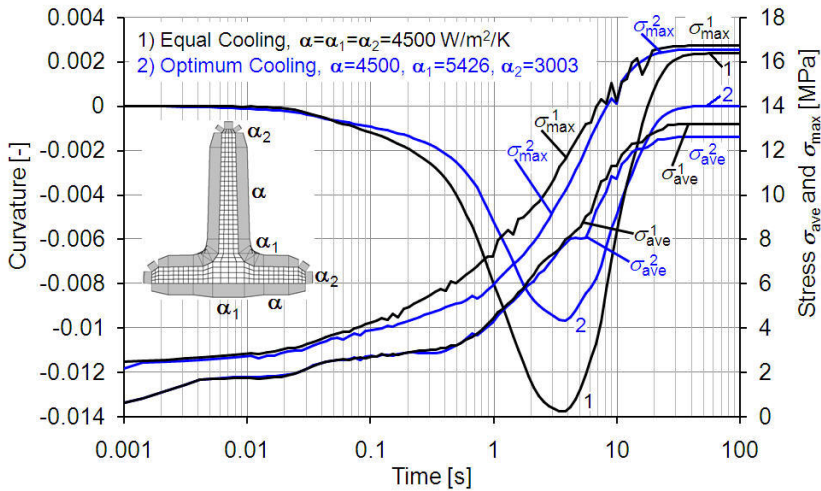


Figure 6.38: Distortion, average residual stress and max. residual stress vs. time for different cooling strategies (Aluminum, T profile)

6.10 Comparison of different geometries

After studying L and T profiles, U profiles are also studied in order to generalize the findings for all profile geometries. A series of simulations has been performed for the cooling of a U120×12 profile with the same range of HTCs 10 to $4500 \text{ W/m}^2/\text{K}$. The computed distortion and residual stresses are demonstrated in Fig. 6.39 (which is very similar to that of T profile given in Fig. 6.34). The highest distortion and stresses occur for a HTC value of $4500 \text{ W/m}^2/\text{K}$. The evolutions of temperature, distortion and stresses in time are investigated for the HTCs 20, 200 and $4500 \text{ W/m}^2/\text{K}$ in order to characterize the cooling behavior of the profile.

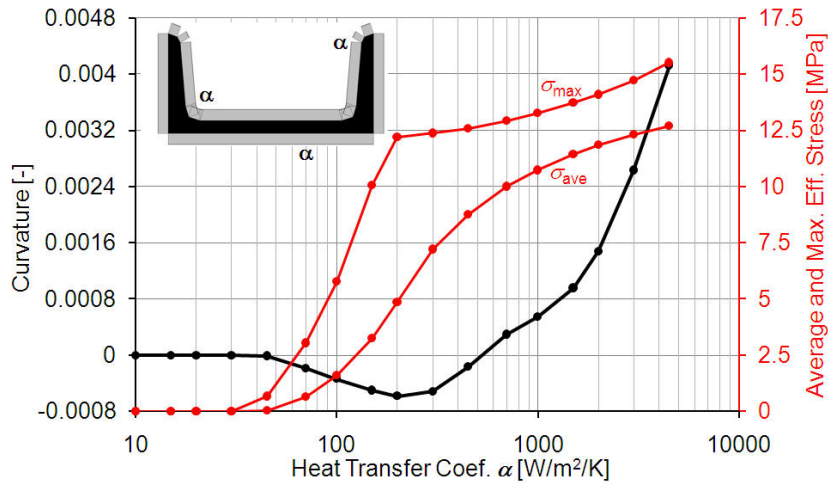


Figure 6.39: Distortion, average residual stress and max. residual stress vs. HTC α (Aluminum, U profile)

The evolutions of the average temperatures and the maximum temperature are illustrated in Fig. 6.40 for three different HTCs, 20, 200 and 4500 $W/m^2/K$. The maximum temperature difference is much higher in the case of intensive cooling but it is very small for low cooling regimes as expected.

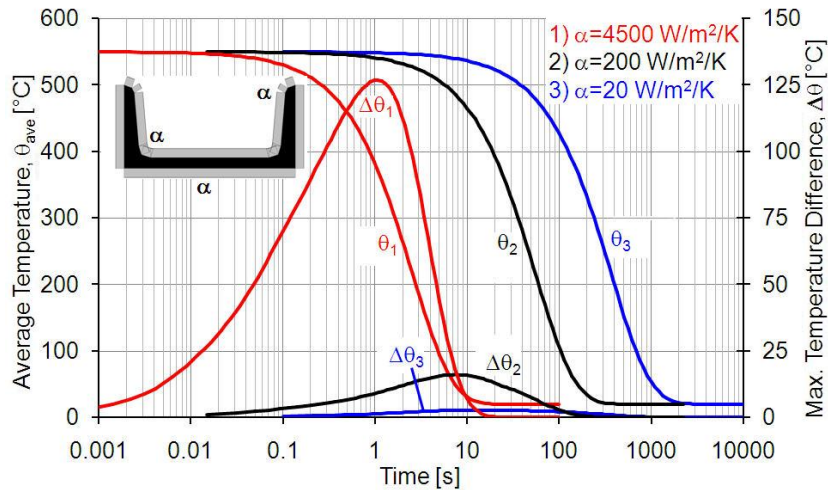


Figure 6.40: Average temperature and max. temperature difference vs. time for different HTC α (Aluminum, U profile)

The evolution of the distortions are compared for three different cooling intensities in Fig. 6.41. The natural axis of the U profile is parallel to its web and located at the centroid. The mass lumped regions remain below the natural axis. Therefore, the curvature is always negative at the initial stages of a homogeneous

cooling. However, depending on the cooling intensity, this behavior may change at later stages of the cooling. When the cooling is very high, the distortion changes its direction three times. The high plastic deformations due to high temperature gradients are responsible for the directional changes of distortion. The extend of the plastic zones are easily noticeable in Fig.6.42 which shows the average and the maximum effective stresses. For HTC $\alpha = 20 \text{ W/m}^2/\text{K}$, the stresses are always in the elastic range during the cooling. Therefore, there remain neither residual stress nor distortion after the cooling. When the cooling is increased to $\alpha = 200 \text{ W/m}^2/\text{K}$, the yielding of the material partly starts. The average effective stresses are much smaller than the maximum effective stresses. Therefore, one can say that after the cooling only a small portion of the profile is plastically deformed. However, the whole profile can plastically deformed for a very intensive cooling. Notice that the average residual stresses slightly smaller than the maximum effective stresses.

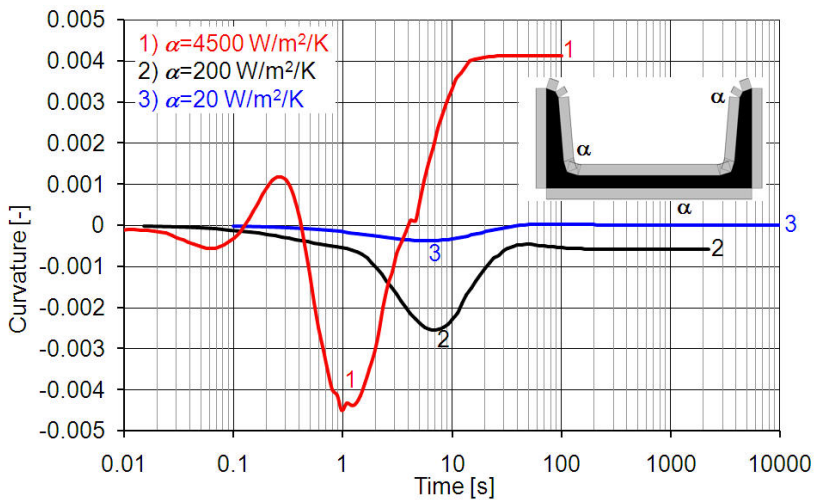


Figure 6.41: Distortion vs. time for different HTC α (Aluminum, U profile)

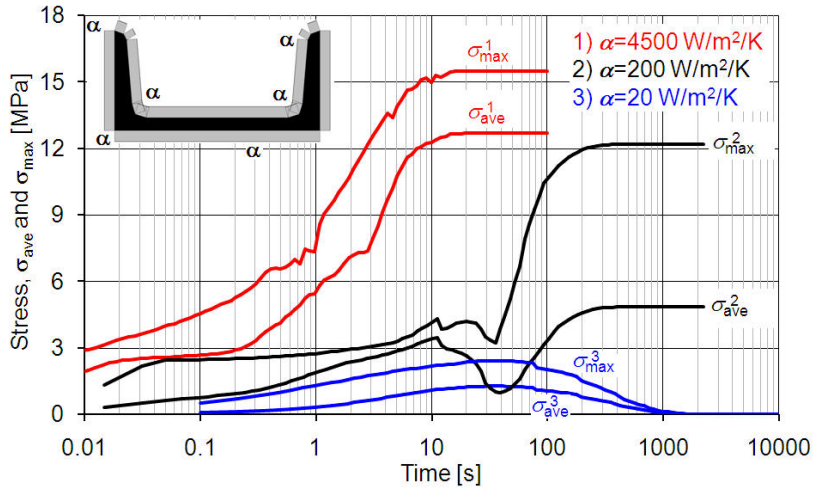


Figure 6.42: Average residual stress and max. residual stress vs. time for different HTC α (Aluminum, U profile)

Now the simulation results for L, T and U profiles are compared in the cooling range of 10 to 4500 $W/m^2/K$. Mostly, they have very similar characteristics. The different behaviors are explained for a complete understanding. The final distortions are very similar for the L, T and U profiles as shown in Fig. 6.43.

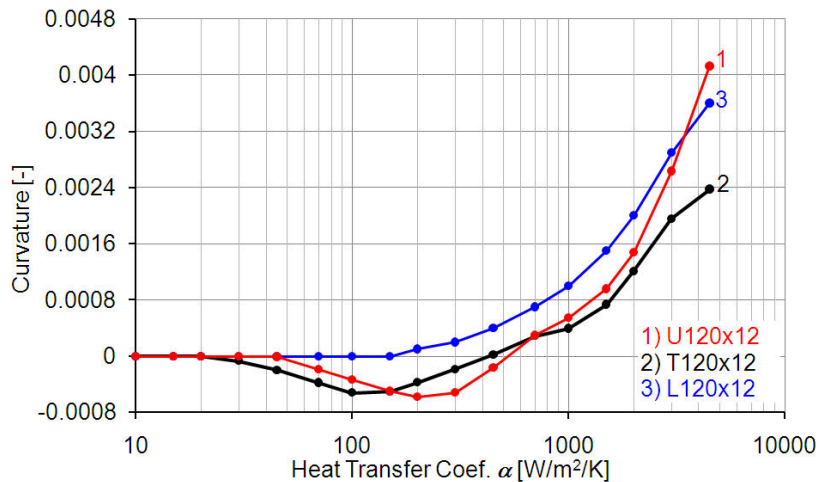


Figure 6.43: Distortion vs. HTC α for different geometries made of aluminum

The evolutions of the distortion for different geometries are compared in Fig. 6.44 for cooling with a homogeneous HTC of $\alpha = 4500 W/m^2/K$. Although the final distortion is maximum for the U profile, the distortion observed during the cooling is smaller. This is reasonable since the distortion of U profile changes the direction three times during the cooling.

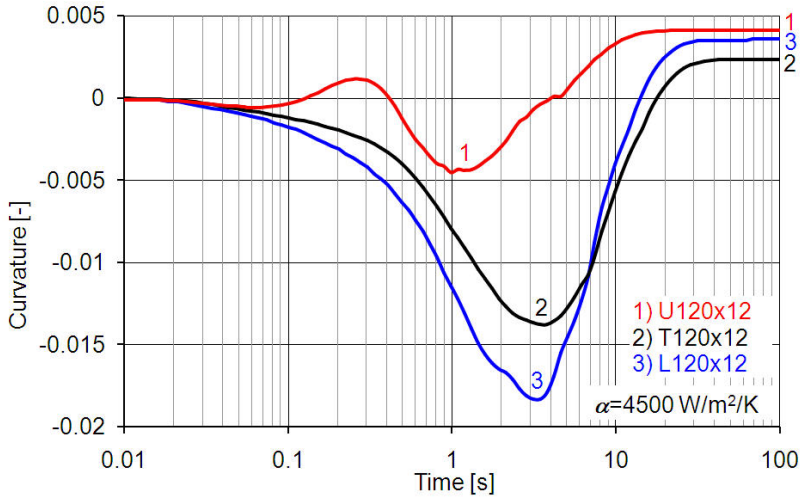


Figure 6.44: Distortion vs. time for different geometries (Aluminum)

The evolutions of temperature and maximum temperature difference are compared in Fig. 6.45 for L, T and U profile geometries when HTC $\alpha = 4500 \text{ W/m}^2/\text{K}$. The cooling of the U profile is relatively slow since it has two mass-lumped regions. The maximum temperature difference is higher for T profile because the mass-lumped region has less area for cooling.

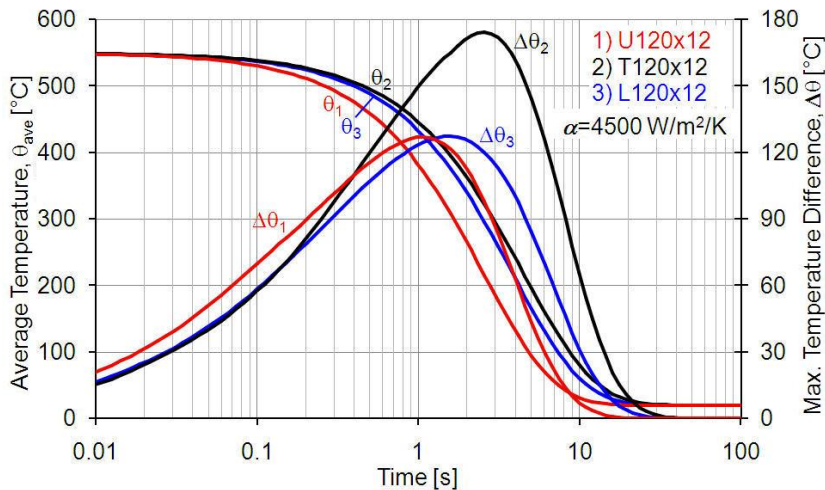


Figure 6.45: Average temperature and max. temperature difference vs. time for different geometries of aluminum profiles

The stress evolutions are very similar for these three profiles.

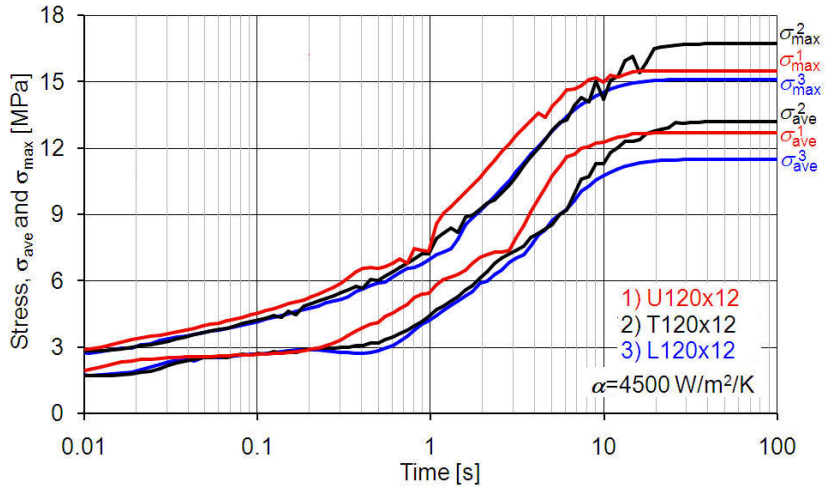


Figure 6.46: Average residual stress and max. residual stress vs. time for different geometries of aluminum profiles

6.11 Disks made of 100Cr6

A disk with a hole has been considered in the simulations. The outer edge of the disk is sharp and one quarter is straight as shown in Fig. 6.47. For a homogeneous quenching with $\text{HTC } 300 \text{ W/m}^2/\text{K}$, the central hole has a distortion which is also verified by experiments [BSO+05, BSO+06]. Many simulations have been performed for reducing the distortion and residual stresses in the disk. The HTC through an annular ring is increased gradually and the corresponding distortion and stresses are calculated. Since the disk is very thin it can be modeled by using plane stress finite elements. The distortion of the disk is described by the deviation of the central hole from the perfect circle. The computed distortion, average and maximum effective stress are plotted in Fig. 6.47. The minimum distortion and average effective stress are calculated for an increase of $\alpha_1 - \alpha = 850 \text{ W/m}^2/\text{K}$ in the HTC. Moreover, the maximum effective stress is minimized nearby when $\alpha_1 - \alpha = 1050 \text{ W/m}^2/\text{K}$. The evolutions of temperature, phase fractions, distortion and stresses in time are of interest for the HTC's ($\alpha_1 - \alpha =$) 0, 850 and $1050 \text{ W/m}^2/\text{K}$ in order to characterize the cooling behavior of the disk.

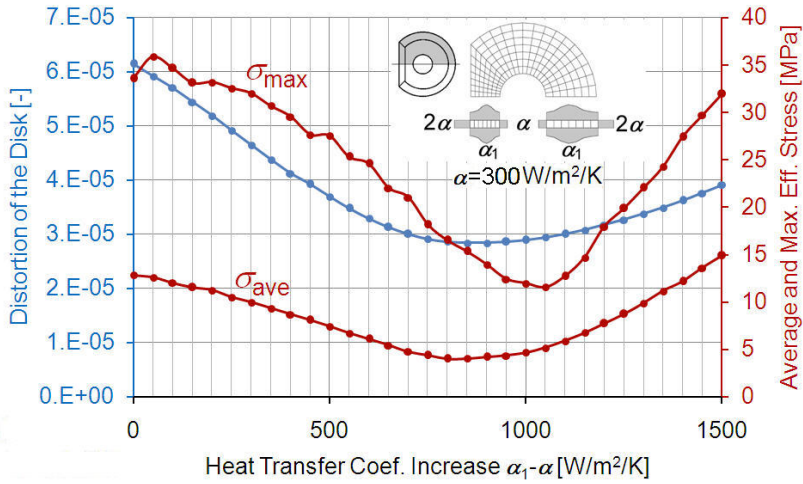


Figure 6.47: Distortion, average residual stress and max. residual stress vs. HTC $\alpha_1 - \alpha$ (100Cr6, Disk)

The evolutions of the average temperature and maximum temperature differences during the cooling time are plotted in Fig. 6.48. As expected the maximum temperature differences for the optimized cooling strategies are very small as compared to homogeneous cooling with HTC $\alpha = 300 \text{ W/m}^2/\text{K}$.

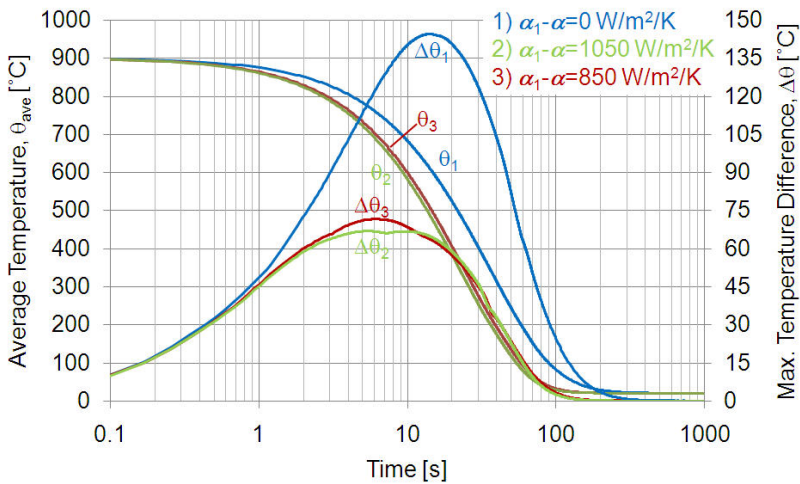


Figure 6.48: Average temperature and max. temperature difference vs. time for different cooling strategies (100Cr6, Disk)

The average phase fraction for the whole disk gives a clear idea of the transformation times. The total cooling provided by the homogeneous cooling is the smallest. Therefore, less martensite and more pearlite is observed in Fig. 6.49.

The pearlitic transformation took place approximately between $t = 10$ s and $t = 30$ s. The martensitic transformation took place approximately $t = 30$ s and $t = 110$ s.

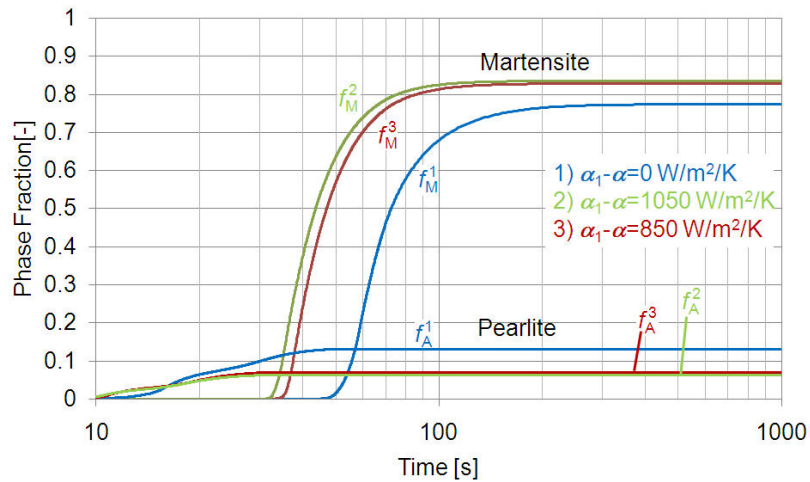


Figure 6.49: Phase fractions vs. time for different cooling strategies (100Cr6, Disk)

With Fig. 6.50, the evolution of the stresses will be explained. The phase transformations have a great influence on the stresses. In the initial period of cooling (up to $t = 10$ s), the stresses continuously increases due to the increasing temperature gradient and reaches a maximum. After $t = 10$ s, the stresses start decreasing due to reducing the temperature gradient and pearlitic phase transitions. Plastic strains introduced by the pearlitic transformation helps to relax the stresses. After $t = 30$ s, the stresses suddenly increase and fluctuate upon the start of martensitic transformation. The fluctuations gradually reduce and continues until martensitic transformation ends ($t = 110$ s).

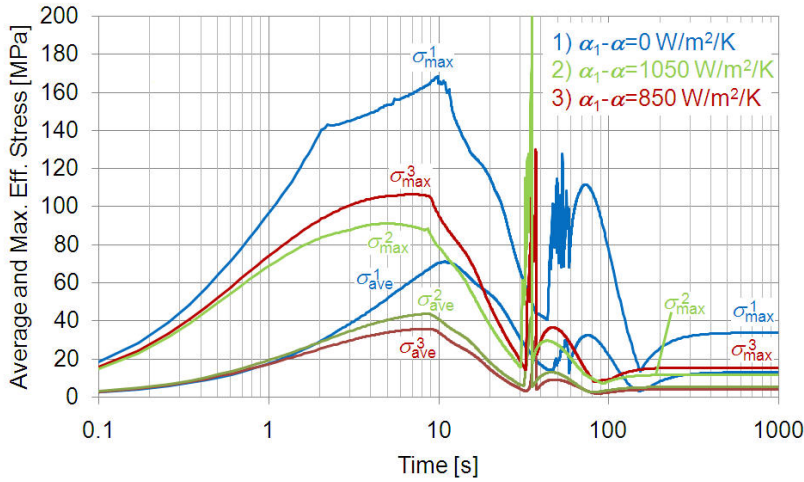


Figure 6.50: Average residual stress and max. residual stress vs. time for different different cooling strategies (100Cr6, Disk)

The contours of maximum stresses for standard cooling with a homogeneous HTC and for optimized cooling with HTC difference $\alpha_1 - \alpha = 850 \text{ W/m}^2/\text{K}$ are shown in Fig. 6.52. The stresses are reduced considerably with such an optimized cooling strategy.

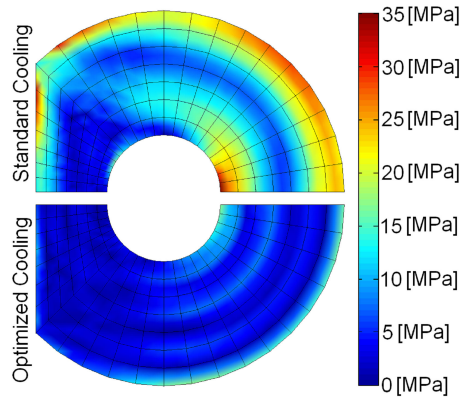


Figure 6.51: Contours of maximum residual stress for different optimum coolings (100Cr6, Disk)

The evolutions of the distortions are plotted in Fig. 6.52. It can be noticed from the figure that the distortion is initiated mainly by the martensitic phase transition.

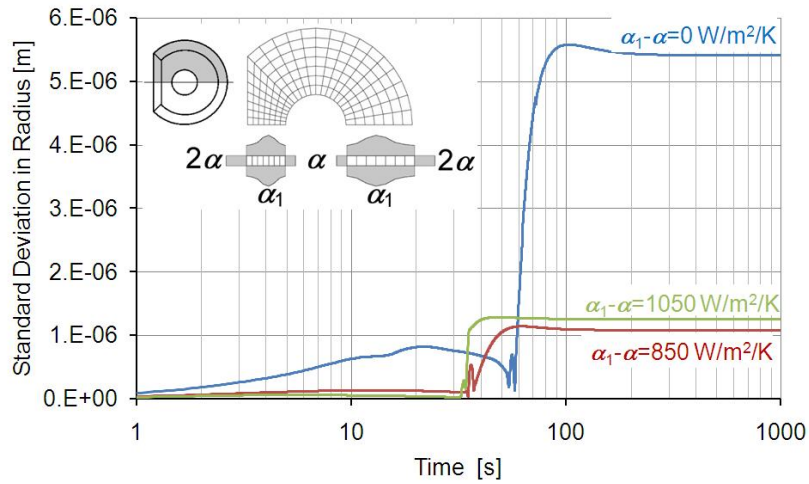


Figure 6.52: Distortion vs. time for different cooling strategies (100Cr6, Disk)

6.12 Effects of material properties on distortion and stresses

6.12.1 Effects of mechanical material properties

The effects of the mechanical material parameters (bulk modulus, shear modulus, yield strength, and hardening modulus) on the distortion and the residual stresses are investigated for an L120×12 profile made of 100Cr6. The bulk modulus and the shear modulus are used to describe the stress strain relationship in the elastic range, and additionally in the plastic range, shear modulus and the hardening modulus are used. The bulk modulus is related to the volumetric change under stress so it does not influence the plastic deformations. These parameters are modified for all phases by a multiplier, and changes in the distortion and residual stresses are observed (Figs. 6.53, 6.54 and 6.55). It can be noticed that the shear modulus has the highest influence while the hardening modulus has no influence.

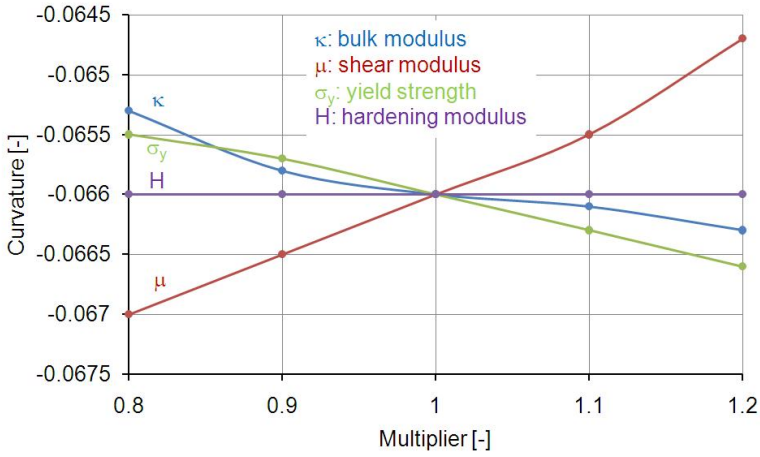


Figure 6.53: Sensitivity of distortion to the mechanical material properties (100Cr6, L profile)

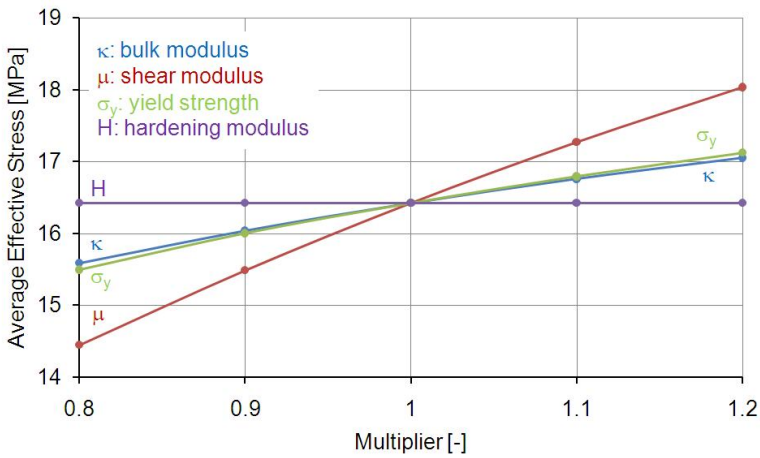


Figure 6.54: Sensitivity of average stress to the mechanical material properties (100Cr6, L profile)

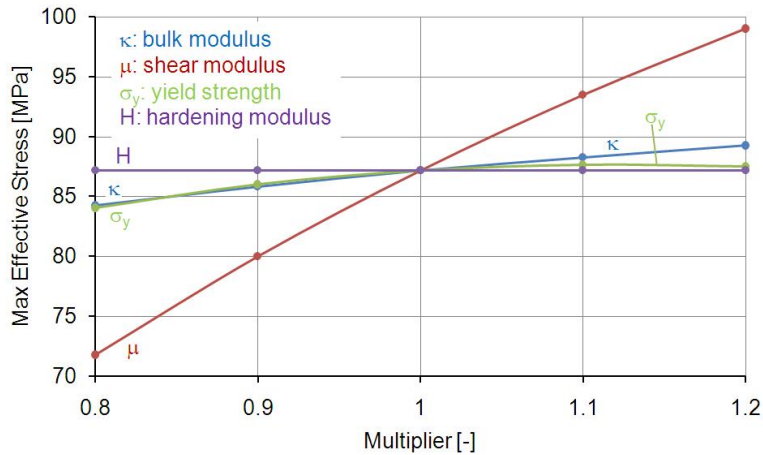


Figure 6.55: Sensitivity of maximum stress to the mechanical material properties (100Cr6, L profile)

6.12.2 Effects of thermal material properties

The material parameters which appear in the Fourier's heat conduction equation are called thermal material properties. The effects of thermal material parameters (conductivity, specific heat capacity, and density) on the distortion and residual stresses are investigated for an L120×12 profile made of 100Cr6. These parameters are modified for all phases by a multiplier and changes in the distortion and residual stresses are observed (Figs. 6.56, 6.57 and 6.58)

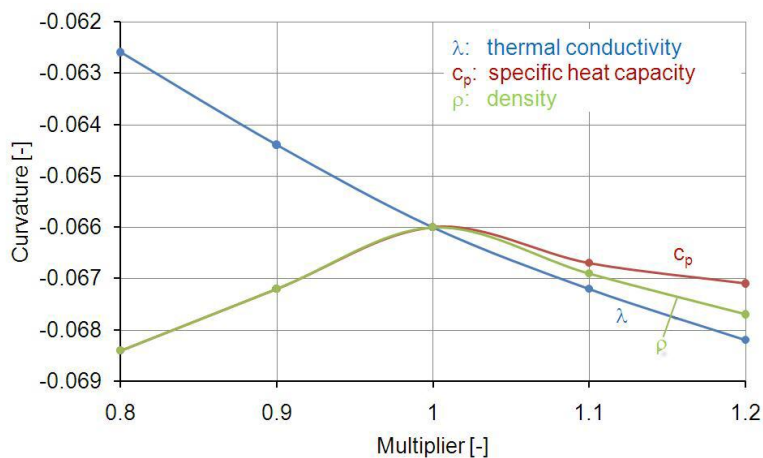


Figure 6.56: Sensitivity of distortion to the thermal material properties (100Cr6, L profile)

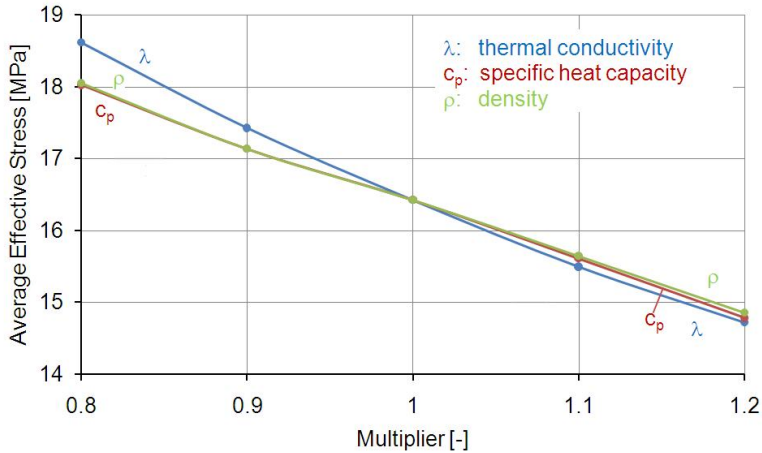


Figure 6.57: Sensitivity of average stress to the thermal material properties (100Cr6, L profile)

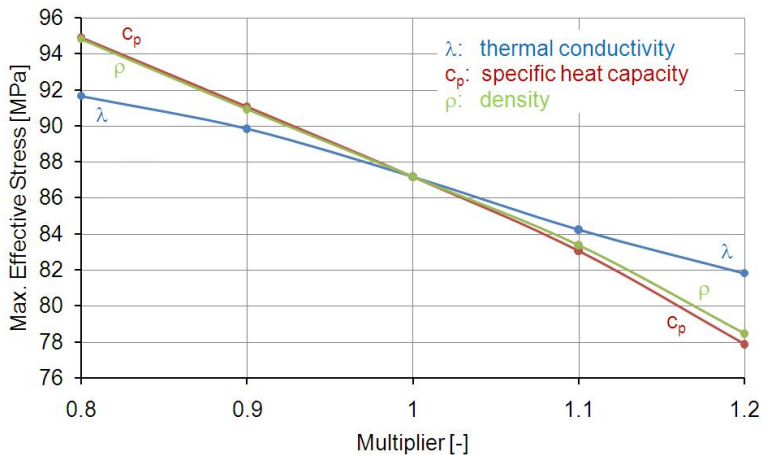


Figure 6.58: Sensitivity of maximum stress to the thermal material properties (100Cr6, L profile)

6.12.3 Effects of metallurgical material properties

The material properties which are used in the phase transformation computations are called metallurgical material properties. The Transformation Induced Plasticity (TRIP) has a great influence on distortion and residual stresses. Therefore, TRIP effects should be included in the model to obtain realistic and reliable simulation results. The effects of material properties which control the phase transformation have been studied here. The effects of TRIP or Greenwood-Johnson coefficients are skipped because in our model it is approximated in terms of densities and yield strengths.

The Time-Temperature-Transformation (TTT) diagram is the material property which controls the diffusional transformation. Therefore, its influence on the distortion and residual stresses are studied by shifting the transformation start and end times. The martensitic transformations are controlled by martensitic transformation start temperature and the temperature coefficient in the exponent. L120×12 profile made of steel 100Cr6 is considered in the simulations. The effect of these three parameters are summarized in Figs 6.59, 6.60 and 6.61.

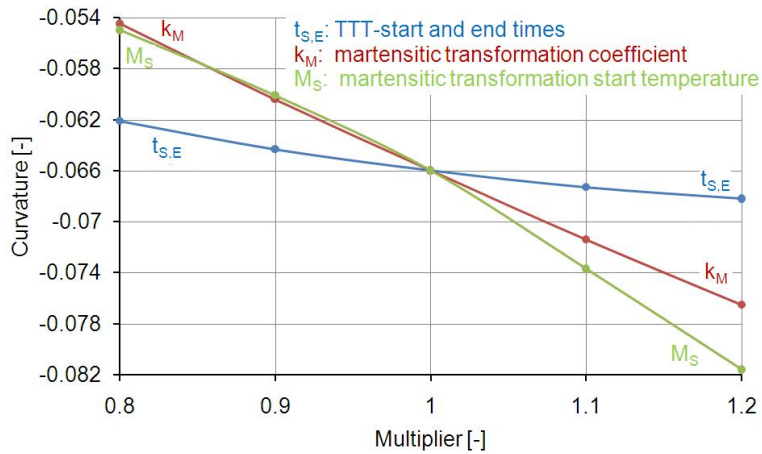


Figure 6.59: Sensitivity of distortion to the metallurgical material properties (100Cr6, L profile)

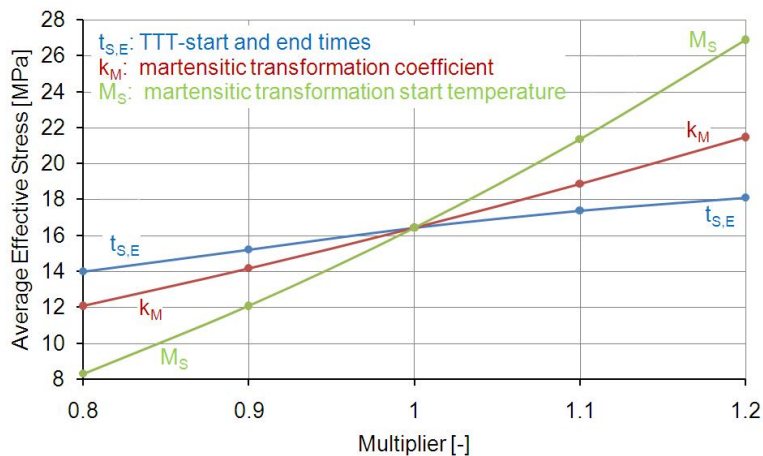


Figure 6.60: Sensitivity of average stress to the metallurgical material properties (100Cr6, L profile)

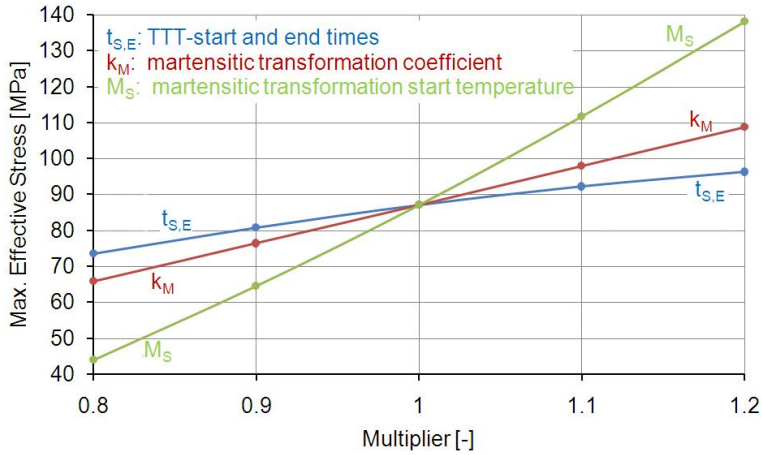


Figure 6.61: Sensitivity of maximum stress to the metallurgical material properties (100Cr6, L profile)

6.13 Summary and conclusions

This chapter was devoted to present all the simulation results. Many simulations were performed for different geometries (long profiles with different cross-sections and disks) and different materials (100Cr6, C80, C45, Aluminum). It has been found that phase transformation is the main reason for the large distortion. Non-phase changing metals may have distortion when they are intensively quenched.

The optimum cooling strategy can be obtained from finite element simulations. The simulation results show that the distortion and stresses can be reduced with an appropriate cooling strategy. Increasing the cooling at the mass-lumped regions reduces only the distortion but increases the stresses. However, an enhanced cooling at the mass-lumped region, and reduced cooling at the edges and thin parts, reduces both distortion and stresses. This optimization procedure is independent of geometries and metals. In practice, the local cooling can be adjusted e.g., with a nozzle field of gas or atomized water sprays.

Bibliography

- [AAN03] F.M. Al-Abbasi and J.A. Nemes. Micromechanical modeling of dual phase steels. *International Journal of Mechanical Sciences*, 45:1449–1465, 2003.
- [AB81] P.K. Agrawal and J.K. Brimacombe. Mathematical model of heat flow and austenite-pearlite transformation in eutectoid carbon steel rods for wire. *Metallurgical Transactions*, 12B:121–133, 1981.
- [AR05] J.C. Afonso and G. Ranalli. Elastic properties of three-phase composites: analytical model based on the modified shear-lag model and the method of cells. *Composites Science and Technology*, 65:1264–1275, 2005.
- [A.S79] A.S.M. *Metals Handbook*, volume 1-3. American Society for Metals, 9 edition, 1979.
- [AS93] F. Armero and J.C. Simo. A priori stability estimates and unconditionally stable product algorithms for nonlinear coupled thermo-plasticity. *International Journal of Plasticity*, 9:749–782, 1993.
- [Att05] M.A.M. Attalla. *Experimental Investigation of Heat Transfer Characteristics from Arrays of Free Impinging Circular Jets and Hole Channels*. PhD thesis, Otto-von-Guericke-Universitaet, Magdeburg, Germany, 2005.
- [Bat96] K.J. Bathe. *Finite Element Procedures*. Prentice-Hall Inc., 5 edition, 1996.
- [Ber98] A. Bertram. An alternative approach to finite plasticity based on material isomorphisms. *International Journal of Plasticity*, 14:353–374, 1998.
- [BH51] J.F.W. Bishop and R. Hill. A theory of the plastic distortion of a polycrystalline aggregate under combined stresses. *Phil. Mag.*, 42:414–427, 1951.
- [BH02] N. Boeck and G.A. Holzapfel. A large strain continuum and numerical model for transformation induced plasticity (tripling). In *Fifth World Congress on Computational Mechanics*, pages –, Austria, 2002.
- [BI98] A. Bokota and S. Iskierka. Numerical analysis of phase transformations and residual stresses in steel cone-shaped elements hardened by

- induction and flame methods. *International Journal of Mechanical Sciences*, 40:617–629, 1998.
- [BKS05] M. Brzoza, Y. Kaymak, and E. Specht. Study of controlled quenching for minimizing stress and equalizing hardness as examples for shafts and discs. In *12th International Metallurgy-Materials Congress and Fair*, Istanbul, Turkey, 2005. ISBN 9944-89-073-1.
- [BSO⁺05] M. Brzoza, E. Specht, J. Ohland, U. Fritsching, and P. Mayr. Simulation and measurement of hardness, microstructure and stresses during gas-quenching of shafts, (german: Simulation und messung von haerte, gefuege und spannung bei flexibler gasabschreckung am beispiel von wellen). *Haerterei Technische Mitteilungen*, 60:166–172, 2005.
- [BSO⁺06] M. Brzoza, E. Specht, J. Ohland, O. Belkessam, T. Lübben, and U. Fritsching. Minimizing stress and distortion for shafts and discs by controlled quenching in a field of nozzels. *Materials Science and Engineering Technology*, 37:97–102, 2006.
- [CB04] M. Canadija and J. Brnic. Associative coupled thermoplasticity at finite strain with temperature-dependent material parameters. *International Journal of Plasticity*, 20:1851–1874, 2004.
- [CCC02] M. Coret, S. Calloch, and A. Combescure. Experimental study of the phase transformation plasticity of 16mnd5 low carbon steel under multiaxial loading. *International Journal of Plasticity*, 18:1707–1727, 2002.
- [CJ96] H.S. Carslaw and J.C. Jaeger. *Conduction of Heat in Solids*. Oxford Science Publications, 2 edition, 1996.
- [CTO00] H. Cetinel, M. Toparli, and L. Ozsoyeller. A finite element based prediction of the microstructural evolution of steels subjected to the tempcore process. *Mechanics of Materials*, 32:339–347, 2000.
- [DB04] S. Dachkovski and M. Boehm. Finite thermoplasticity with phase changes based on isomorphisms. *International Journal of Plasticity*, 20:323–334, 2004.
- [DGSS87] S. Denis, E. Gautier, S. Sjoestroem, and A. Simon. Influence of stress on the kinetics of pearlitic transformation during continuous cooling. *Acta Metallica*, 35:1621–1632, 1987.
- [EH86] H.J. Exner and H.P. Hougardy. Introduction to the quantitative microstructure analysis, (german: Einfuehrung in die quantitative gefuegeanalyse). *DGM Informationsgesellschaft Oberursel*, pages 8–18, 1986.
- [FDS84] F.M.B. Fernandes, S. Denis, and A. Simon. Mathematical model coupling phase transformation and temperature evolution during quenching of steels. *Material Science and Technology*, 1:838–844, 1984.

- [FOTN98] F.D. Fischer, E.R. Oberaigner, K. Tanaka, and F. Nishimura. Transformation induced plasticity revised an updated formulation. *International Journal of Solids and Structures*, 38:2209–2227, 1998.
- [FRW⁺00] F.D. Fischer, G. Reisner, E. Werner, K. Tanaka, G. Cailletaud, and T. Antretter. A new view on transformation induced plasticity (trip). *International Journal of Plasticity*, 16:723–748, 2000.
- [GJ65] G.W. Greenwood and R.H. Johnson. The deformation of metals under small stress during phase transformation. *Proc. Royal Sci.*, A283:403–422, 1965.
- [Gla92] S. Glaser. *Berechnung gekoppelter thermomechanischer Prozesse*. PhD thesis, Universitaet Stuttgart, Germany, 1992.
- [GT96] C.H. Gur and A.E. Tekkaya. Finite element simulation of quench hardening. *Steel Research*, 67:298–306, 1996.
- [GTS96] C.H. Gur, A.E. Tekkaya, and W. Schuler. Effect of boundary conditions and workpiece geometry on residual stresses and microstructure in quenching process. *Steel Research International*, 67:501–506, 1996.
- [HE79] B. Hildenwall and T. Ericsson. Prediction of residual stresses in case-hardening steels, hardenable steels, hardenability concepts with application to steel. In *Proceeding of Symposium*, pages 579–605, Sheraton Chicago Hotel, 1979.
- [Hin90] E. Hinteregger. *Eigenspannungen und Verformungen in Schienen nach dem Walzen vor dem Richten*. PhD thesis, Montan Universitaet Leoben, Austria, 1990.
- [HJ02] Han H.N. and Lee J.K. A constitutive model for transformation superplasticity under external stress during phase transformation of steels. *ISIJ International*, 42:200–205, 2002.
- [Hoe96] D. Hoemberg. A numerical simulation of the jominy end-quench test. *Acta Materialia*, 44:4375–4385, 1996.
- [Hou90] H.P. Hougardy. *Phase Transition and Microstructure of Unalloyed Steel, (German: Umwandlung und Gefuege unlegierter Staehle)*. Steel Research Press, Dusseldorf, Germany, 1990.
- [IK05] T. Iwakuma and S. Koyama. An estimate of average elastic moduli of composites and polycrystals. *Mechanics of Materials*, 37:459–472, 2005.
- [JM39] W.A. Johnson and R.F. Mehl. Reaction kinetics in processes of nucleation and growth. *Trans AIME*, 135:416–458, 1939.
- [JM99] S. Jahanian and M. Mosleh. The mathematical modeling of phase transformation of steel during quenching. *Journal of Materials Engineering and Performance*, 8:75–82, 1999.

- [KBS05] Y. Kaymak, M. Brzoza, and E. Specht. Simulation of the distortion and microstructure distribution in steel profiles during cooling by finite element method. In *12th International Metallurgy-Materials Congress and Fair*, Istanbul, Turkey, 2005. ISBN 9944-89-073-1.
- [KBS06] Y. Kaymak, M. Brzoza, and E. Specht. Reducing the residual stresses and distortion by controlled quenching. In *15th IFHTSE and SMT20*, pages 403–408, Vienna, Austria, 2006. ISBN 3-901 384-19-7.
- [KIK05] J. Kim, S. Im, and H.-G. Kim. Numerical implementation of a thermo-elastic-plastic constitutive equation in consideration of transformation plasticity in welding. *International Journal of Plasticity*, 21:1383–1408, 2005.
- [KM59] D.P. Koistinen and R.E. Marburger. A general equation prescribing the extent of the austenite-martensite transformation in pure iron-carbon alloys and plain carbon steels. *Acta Metallica*, 7:59–60, 1959.
- [Kol37] A.N. Kolmogorov. (in russian). *Izv. Akad. Nauk. SSSR. Ser. Mat.*, 3:355–359, 1937.
- [KS05a] J. Krol and E. Specht. Atomized spray quenching as alternative technique for reduction of distortion and stresses. In *12th International Metallurgy-Materials Congress and Fair*, Istanbul, Turkey, 2005. ISBN 9944-89-073-1.
- [KS05b] J. Krol and E. Specht. Influence of quality of water and roughness of surface on quenching rate. In *International Conference on Continuous Casting of Non-Ferrous Metals*, pages 118–123, Neu-Ulm, Germany, 2005.
- [KS07] Y. Kaymak and E. Specht. Strategies for controlled quenching to reduce stresses and distortion. *Heat Processing*, 5:232–235, 2007.
- [KSP05] J. Krol, E. Specht, and F. Puschmann. Atomized spray for adjustment of local heat transfer in metal quenching. In *International Symposium on Heat and Mass Transfer in Spray Systems*, pages –, Antalya, Turkey, 2005.
- [Leb89] J.B. Leblond. Mathematical modelling of transformation plasticity in steels ii: coupling with strain hardening phenomena. *International Journal of Plasticity*, 5:573–591, 1989.
- [Lev98] V.I. Levitas. Thermomechanical theory of martensitic phase transformations in inelastic materials. *International Journal of Solids and Structures*, 35:889–940, 1998.
- [LL99] M.T. Lusk and Y.K. Lee. A global material model for simulating the transformation kinetics of low alloy steels. In *Proceedings of the 7th International Seminar of the International IFHT*, pages 273–282, 1999.

- [LMDD85] J.B. Leblond, G. Mottet, J. Devaux, and J.C. Devaux. Mathematical model of anisothermal phase transformations in steels, and predicted plastic behavior. *Material Science and Technology*, 1:815–822, 1985.
- [LNMA98] M.V. Li, D.V. Neibuer, L.L. Meekisho, and D.G. Attridge. A computational model for the prediction of steel hardenability. *Metallurgical and Materials Transactions B*, 29:661–672, 1998.
- [LPC⁺98] G. Lielens, P. Pirotte, A. Courniot, F. Dupret, and R. Keunings. Prediction of thermo-mechanical properties for compression molded composites. *Composites Part A*, 29A:63–70, 1998.
- [LSD99] Z. Li, S. Schmauder, and M. Dong. A simple mechanical model to predict fracture and yield strengths of particulate two-phase materials. *Computational Materials Science*, 15:11–21, 1999.
- [Mie03] C. Miehe. Computational micro-to-macro transitions for discretized micro-structures of heterogeneous materials at finite strains based on the minimization of averaged incremental energy. *Computer Methods in Applied Mechanics and Engineering*, 192:559–591, 2003.
- [Mit87] W. Mitter. *Umwandlungsplastizität und ihre Berücksichtigung bei der Berechnung von Eigenspannungen*. Materialkundlich-Technische Gebr. Bornträger, Berlin, Germany, 1987.
- [MN02] B.C. Muddle and J.F. Nie. Formation of bainite as a diffusional-displacive phase transformation. *Scripta Materialia*, 47:187–192, 2002.
- [MPD99] MPDB. Temperature dependent elastic and thermal properties database, 1999. Available from: www.jahm.com.
- [PBK⁺05] R. Pietzsch, M. Brzoza, Y. Kaymak, E. Specht, and A. Bertram. Minimizing the distortion of steel profiles by controlled cooling. *Steel Research International*, 76:399–407, 2005.
- [PBK⁺07] R. Pietzsch, M. Brzoza, Y. Kaymak, E. Specht, and A. Bertram. Simulation of the distortion of long steel profiles during cooling. *Journal of Applied Mechanics*, 74:427–437, 2007.
- [PCL⁺03] V.C. Prantil, M.L. Callabresi, J.F. Lathrop, G.S. Ramaswamy, and M.T. Lusk. Simulating distortion and residual stresses in carburized thin strips. *Journal of Engineering Materials and Technology*, 125:116–124, 2003.
- [Pie00] R. Pietzsch. *Simulation und Minimierung des Verzuges von Stahlprofilen bei der Abkühlung*. PhD thesis, Otto-von-Guericke Universität, Magdeburg, Germany, 2000.
- [PS04a] E. Puschmann and E. Specht. Atomized spray quenching as an alternative quenching method for defined adjustment of heat transfer. *Steel Research International*, 75:283–288, 2004.

- [PS04b] E. Puschmann and E. Specht. Transient measurement of heat transfer for metal quenching with atomized sprays. *Experimental Thermal and Fluid Science*, 28:607–615, 2004.
- [RO00] J. Ronda and G.J. Oliver. Consistent thermo-mechano-metallurgical model of welded steel with unified approach to derivation of phase evolution laws and transformation-induced plasticity. *Computer Methods in Applied Mechanics and Engineering*, 189:361–417, 2000.
- [Sch35] E. Scheil. Anlaufzeit den austenitumwandlung. *Archiv fuer Eisenhüttenwesen*, 8:565, 1935.
- [SDZW01] H. Sun, S. Di, N. Zhang, and C. Wu. Micromechanics of composite materials using multivariable finite element method and homogenization theory. *International Journal of Solids and Structures*, 38:3007–3020, 2001.
- [Ser03] S. Serajzadeh. Prediction of temperature distribution and phase transformation on the run-out table in the process of hot strip rolling. *Applied Mathematical Modelling*, 27:861–875, 2003.
- [SGM05] T. Sourmail and C. Garcia-Mateo. Critical assessment of models for predicting the ms temperature of steels. *Computational Materials Science*, 34:323–334, 2005.
- [SH97] J.C. Simo and T.J.R. Hughes. *Computational Inelasticity*. Springer, New York, 1997.
- [Sim88a] J.C. Simo. A framework for finite strain elastoplasticity based on maximum plastic dissipation and the multiplicative decomposition: Part i. continuum formulation. *Computer Methods in Applied Mechanics and Engineering*, 66:199–219, 1988.
- [Sim88b] J.C. Simo. A framework for finite strain elastoplasticity based on maximum plastic dissipation and the multiplicative decomposition: Part ii. computational aspects. *Computer Methods in Applied Mechanics and Engineering*, 68:1–31, 1988.
- [Sjo84] S. Sjöström. Interactions and constitutive models for calculating quench stresses in steel. *Materials Science and Technology*, 1:823–829, 1984.
- [SM92] J.C. Simo and C. Miehe. Associative coupled thermoplasticity at finite strains: Formulation, numerical analysis and implementation. *Computer Methods in Applied Mechanics and Engineering*, 98:41–104, 1992.
- [SMA02] S. Serajzadeh, H. Mirbagheri, and Taheri A.K. Modelling the temperature distribution and microstructural changes during hot rod rolling of a low carbon steel. *Journal of Materials Processing*, 125-126:89–96, 2002.
- [Smi76] C.J. Smithells. *Metals Reference Book*. Butterworth and Co., London, 5 edition, 1976.

- [Tay38] G.I. Taylor. Plastic strain in metals. *J. Inst. Metals*, 62:307–324, 1938.
- [Tay98] R.E. Taylor. *Thermal Expansion of Solids Data Series on Material Properties*, volume 1-4. ASM International, Ohio, 1998.
- [TCW01] L. Taleb, N. Cavallo, and F. Waeckel. Experimental analysis of transformation plasticity. *International Journal of Plasticity*, 17:1–20, 2001.
- [Tod99] M.T. Todinov. Influence of some parameters on the residual stresses from quenching. *Modelling and Simulation in Material Science Engineering*, 7:25–41, 1999.
- [Tou75] Y.S. Touloukian. *Thermophysical Properties of Matter: Volume 12 Thermal Expansion*, volume 12. IFI/Plenum, New York-Washington, 1975.
- [TS03] L. Taleb and F. Sidoroff. Experimental analysis of transformation plasticity a micromechanical modeling of the greenwood-johnson mechanism in transformation induced plasticity. *International Journal of Plasticity*, 19:1821–1842, 2003.
- [VV87] C. Verdi and A. Visintin. A mathematical model of the austenite-pearlite transformation in plain carbon steel based on the scheil’s additivity rule. *Acta Materialia*, 35:2711–2717, 1987.
- [WCY93] K.F. Wang, S. Chandrasekar, and H.T.Y. Yang. An efficient 2d finite element procedure for quenching analysis with phase change. *ASME Journal of Engineering for Industry*, 115:124–138, 1993.
- [WCY97] K.F. Wang, S. Chandrasekar, and H.T.Y. Yang. Experimental and computational study of the quenching of carbon steel. *ASME Journal of Manufacturing Science and Engineering*, 119:257–265, 1997.
- [YM03] Q. Yu and C.R. Muncie. Effect of cooling and stacking on buckling of plates. *AISE Steel Technology*, pages 35–44, 2003.
- [Yu77] H.J. Yu. *Berechnung von Abkuehlungs-, Umwandlungs-Schweiss-, sowie Verformungseigenstressen mit Hilfe der Methode der Finite Elemente*. PhD thesis, Universität Karlsruhe, Germany, 1977.
- [ZMC02] J.Z. Zhao, C. Mesplont, and De Cooman C. Calculation of the phase transformation kinetics from a dilatation curve. *Journal of Materials Processing Technology*, 129:345–348, 2002.

Appendix A

Material properties

A.1 Steel 100Cr6

Table A.1: Material properties of steel 100Cr6 [Pie00]

	Phases	0°C	200°C	400°C	600°C	800°C	1000°C
Elasticity Modulus [GPa]	A,P,M	212	202	186	166	141	112
Poisson's Ratio [-]	A,P,M	0.283	0.291	0.299	0.307	0.315	0.323
Yield Strength [MPa]	A	300	270	240	210	180	150
	P	479	472	400	277	118	-
	M	1116	914	712	510	-	-
Hardening Modulus [GPa]	A	12.0	10.4	8.8	7.2	5.6	4.0
	P	21.0	26.0	22.0	19.0	11.0	-
	M	63.0	40.0	17.0	-	-	-
Density [kg/m ³]	A	7980	7900	7820	7720	7620	7530
	P,M	7820	7740	7770	7620	7530	7460
Heat Conductivity [W/m/K]	A	14.5	17.2	19.9	22.6	25.3	28.0
	P,M	40.0	39.0	35.5	29.0	20.0	8.5
Heat Capacity [J/kg/K]	A	450	510	570	600	630	650
	P,M	410	550	620	790	1160	1850

A: austenite, P: pearlite, M: martensite

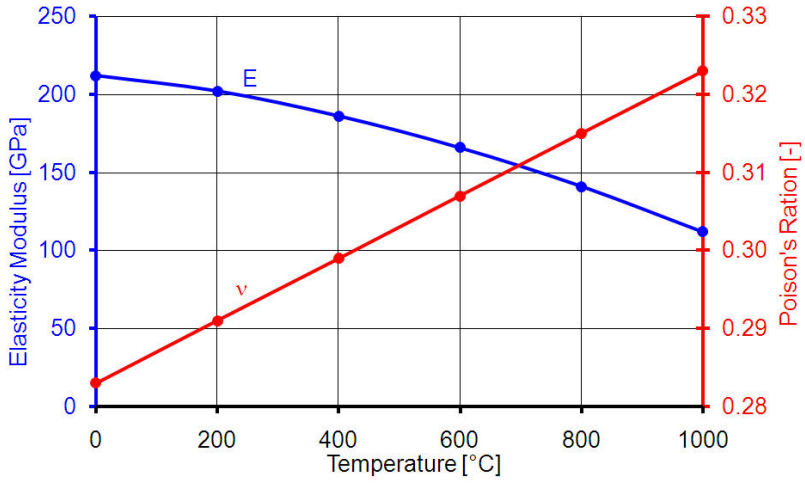


Figure A.1: Elasticity modulus and Poisson's ratio vs. temperature, (100Cr6)

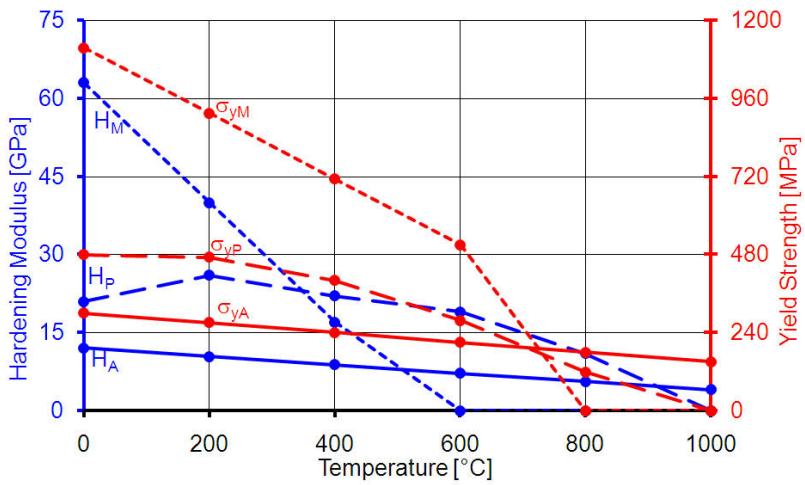


Figure A.2: Hardening modulus and yield strength vs. temperature, (100Cr6)

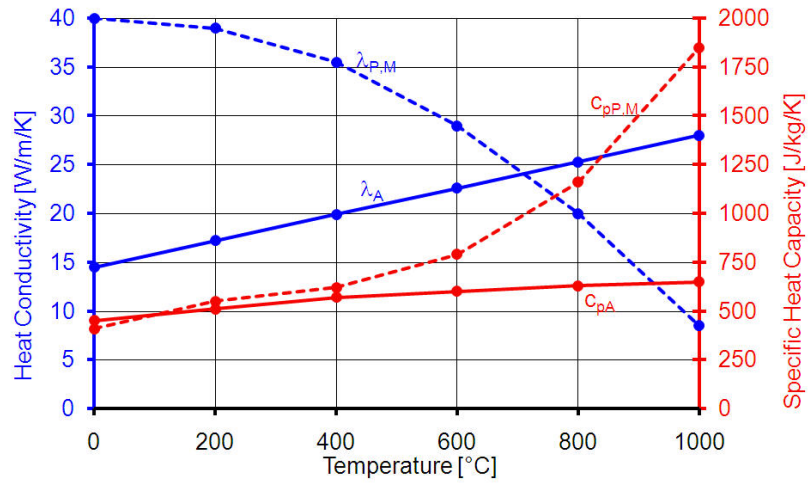


Figure A.3: Heat conductivity and specific heat capacity vs. temperature, (100Cr6)

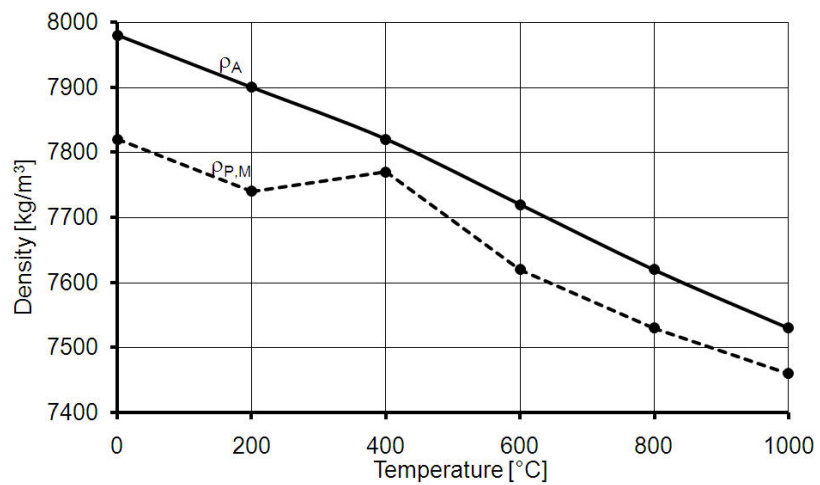


Figure A.4: Density vs. temperature, (100Cr6)



Werkstoff-Datenblatt

Saarstahl - 100Cr6

WerkstoffNr.:	Alte Werksmarke:	Internationale Bezeichnungen:
1.3605	RW3	BS: 2S135, 535A99 AFNOR: 100C6 SAE: 52100

Werkstoffgruppe:	Wälzlagerstahl nach EN ISO 683-17
-------------------------	-----------------------------------

Chemische Zusammensetzung: <small>(Richtanalyse in %)</small>	C	Si	Mn	Cr	Sonst.
	1,00	0,25	0,35	1,50	-

Verwendung:	Wälzlagerstahl für Kugeln und Rollen aller Abmessungen, Ringe und Scheiben in der Regel bis 30 mm Fertigwanddicke.
--------------------	--

Warmformgebung und Wärmebehandlung:	Schmieden oder Walzen:	1100 - 850°C
	Normalglühen:	870 - 900°C/Luft
	Weichglühen:	780 - 800°C/Ofen
	Härten:	800 - 830°C/Wasser
	Härten:	830 - 870°C/Öl
	Anlassen:	150 - 180°C

Mechanische Eigenschaften:	weichgeglüht, +A:	max. 207 HB
-----------------------------------	-------------------	-------------

Behandlungszustand:	Gehärtet und angelassen
----------------------------	-------------------------

Oberflächenhärte [HRC]:	ca. 62
--------------------------------	--------

Figure A.5: Data sheet supplied by Saarstahl AG, Germany (100Cr6)

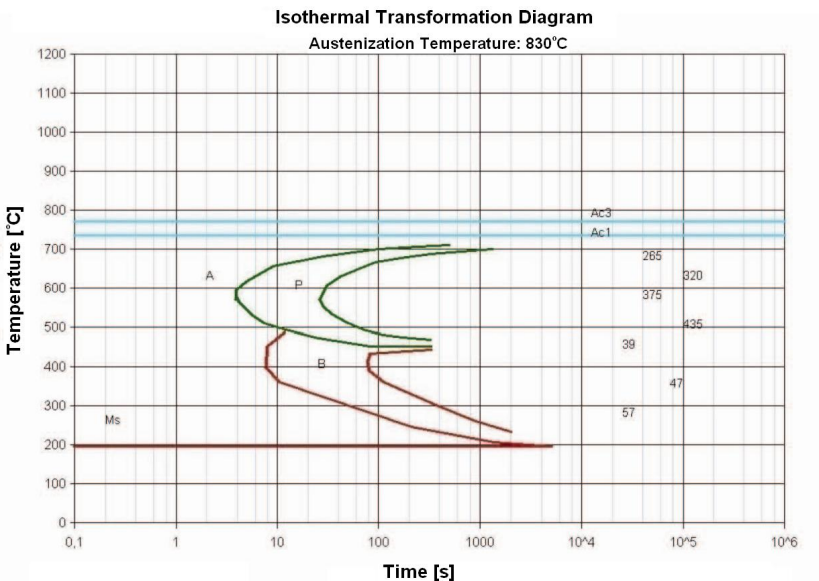


Figure A.6: Isothermal transformation diagram supplied by Saarstahl AG, Germany (100Cr6)

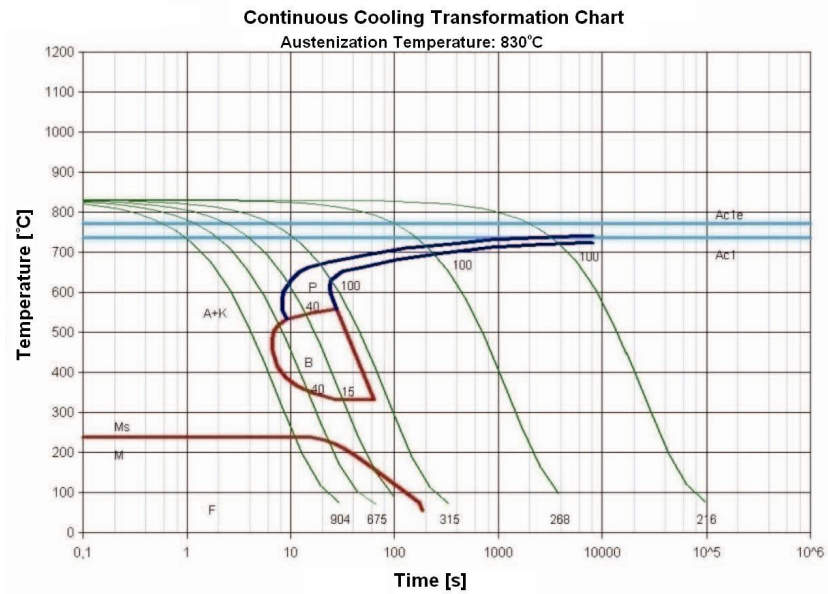


Figure A.7: Continuous cooling transformation diagram supplied by Saarstahl AG, Germany (100Cr6)

Table A.2: Numerical values for IT and CCT graphs and their graph, (100Cr6)

IT-data				CCT-data			
ts [s]	Ts [°C]	te [s]	Te [°C]	ts [s]	Ts [°C]	te [s]	Te [°C]
340.80	452	1373.06	700	8489.63	742	8533.18	723
79.92	452	305.80	687	848.96	732	862.10	713
24.64	474	91.87	666	127.84	710	104.18	681
7.67	509	42.58	631	22.79	675	31.79	652
5.78	529	31.08	607	14.16	660	24.11	627
4.26	564	26.62	571	12.21	651	24.11	599
3.96	578	28.47	554	10.15	630	27.97	558
3.96	596	35.91	532	8.49	601	15.85	548
5.08	618	49.45	511	8.36	574	9.21	533
8.91	655	73.59	493	8.45	552		
30.13	683	106.15	482	9.21	533		
93.79	700	192.18	474				
512.36	711	335.56	469				

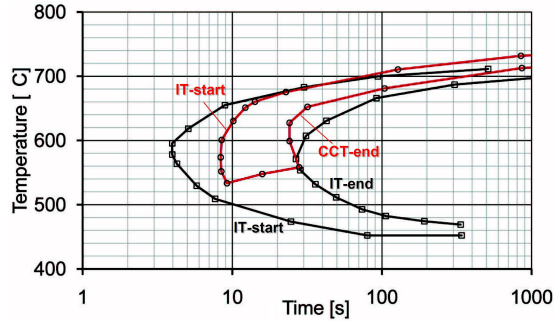


Figure A.8: Isothermal and continuous cooling transformation diagrams, (100Cr6)

A.2 Steel C45

Table A.3: Material properties of steel C45 [Pie00]

	Phases	0°C	200°C	400°C	600°C	800°C	1000°C
Elasticity Modulus [GPa]	A	200	160	120	80	40	-
	P,M	215	196	177	158	140	121
Shear Modulus [GPa]	A	80	64	48	32	16	-
	P,M	83	75	67	59	52	44
Yield Strength [MPa]	A	250	200	150	100	50	-
	P	550	420	470	470	180	-
	M	1000	940	800	-	-	-
Hardening Modulus [GPa]	A	4.2	4.0	3.7	3.1	2.3	1.4
	P	5.1	5.8	4.9	2.6	-	-
	M	12.5	10.0	7.5	-	-	-
Density [kg/m ³]	A	7940	7860	7790	7700	7600	7500
	P,M	7850	7790	7710	7630	7530	7430
Heat Conductivity [W/m/K]	A	14.8	17.3	19.6	21.9	24.3	26.7
	P,M	48.8	46.5	41.0	35.0	26.0	17.0
Heat Capacity [J/kg/K]	A	450	510	570	600	630	650
	P,M	410	550	620	790	1160	1850

A: austenite, P: pearlite, M: martensite

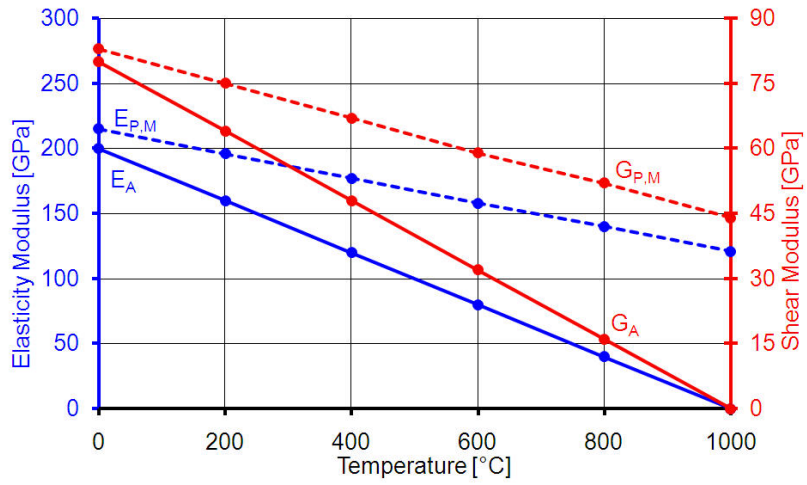


Figure A.9: Elasticity modulus and shear modulus vs. temperature, (C45)

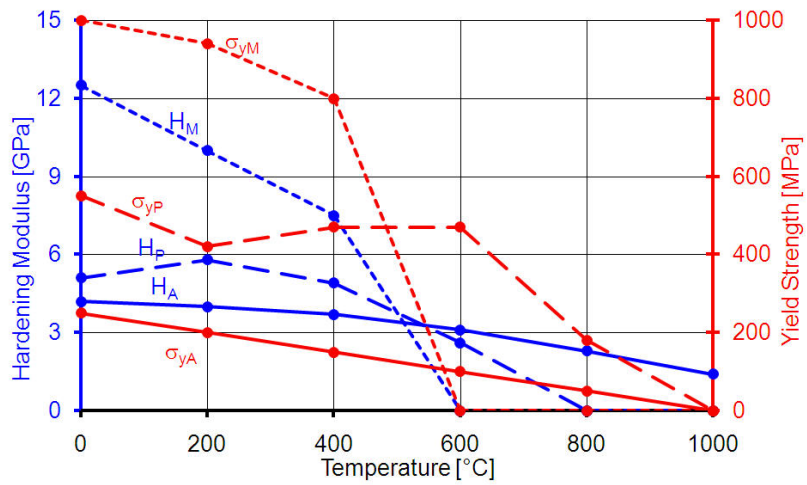


Figure A.10: Hardening modulus and yield strength vs. temperature, (C45)

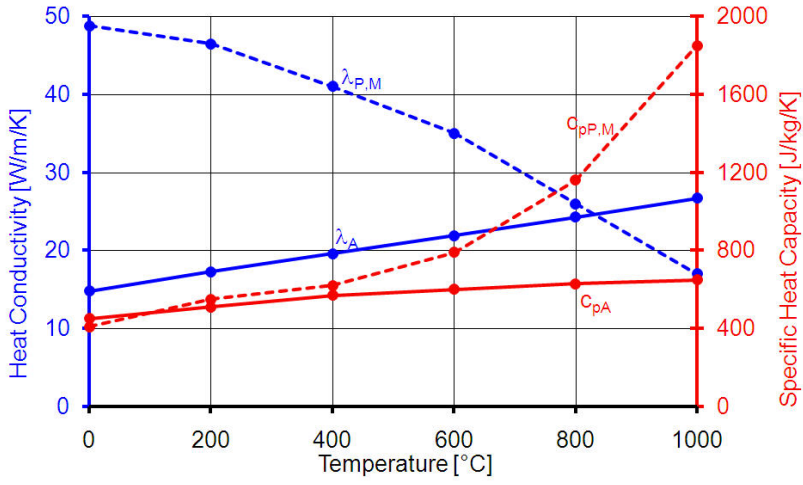


Figure A.11: Heat conductivity and specific heat capacity vs. temperature, (C45)

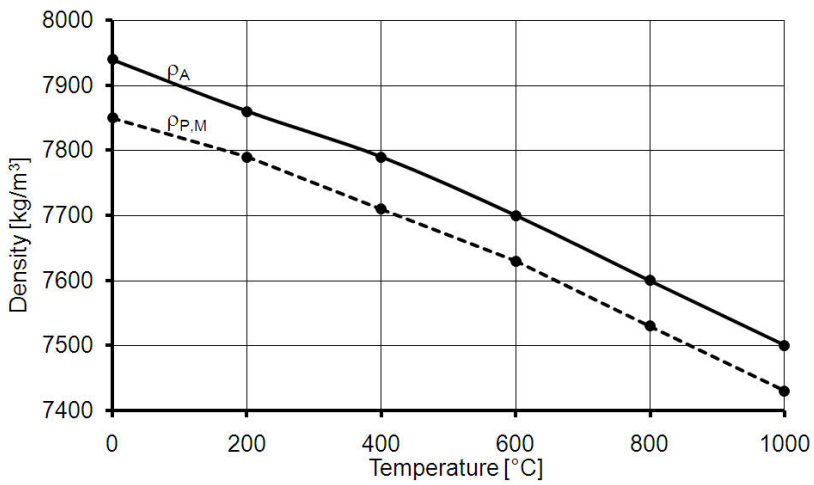


Figure A.12: Density vs. temperature, (C45)

A.3 Steel C80

Table A.4: Material properties of steel C80 [Pie00]

	Phases	0°C	200°C	400°C	600°C	800°C	1000°C
Elasticity Modulus [GPa]	A	220	176	132	88	44	-
	P,M	220	200	175	133	80	13
Shear Modulus [GPa]	A	80	64	48	32	16	-
	P,M	83	75	67	59	52	44
Yield Strength [MPa]	A	250	200	150	100	50	-
	P	650	625	450	375	150	-
	M	1000	945	775	505	150	-
Hardening Modulus [GPa]	A	1.4	1.4	1.5	1.5	1.4	1.3
	P	4.0	4.7	4.5	1.8	-	-
	M	60.0	50.0	40.0	-	-	-
Density [kg/m ³]	A	7740	7690	7640	7590	7540	7490
	P,M	7860	7790	7720	7650	7570	7490
Heat Conductivity [W/m/K]	A	6	10	14	18	22	26
	P,M	50	45	38	32	29	27
Heat Capacity [J/kg/K]	A	450	510	570	600	630	650
	P,M	410	550	620	790	1160	1850

A: austenite, P: pearlite, M: martensite

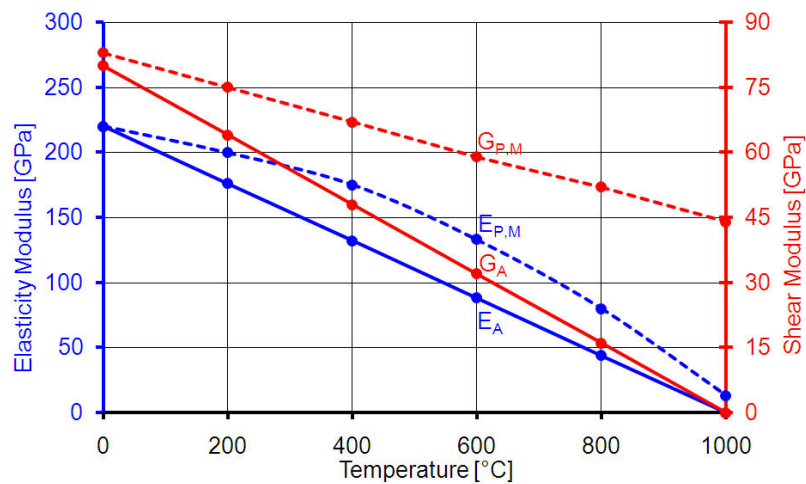


Figure A.13: Elasticity modulus and shear modulus vs. temperature, (C80)

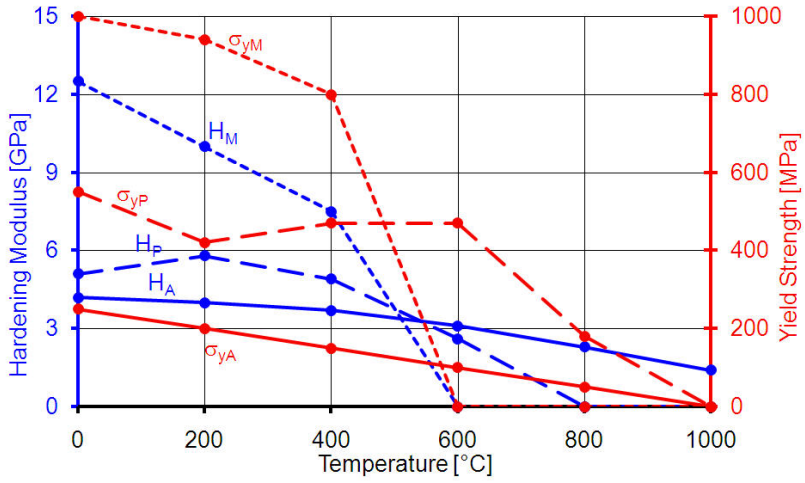


Figure A.14: Hardening modulus and yield strength vs. temperature, (C80)

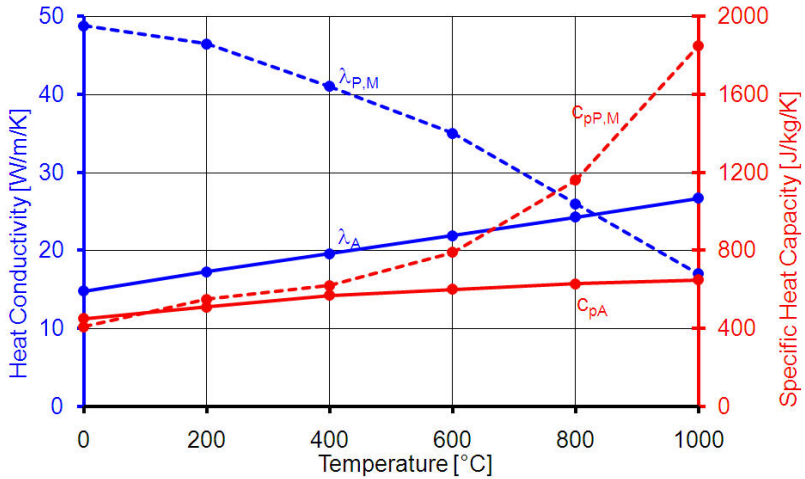


Figure A.15: Heat conductivity and specific heat capacity vs. temperature, (C80)

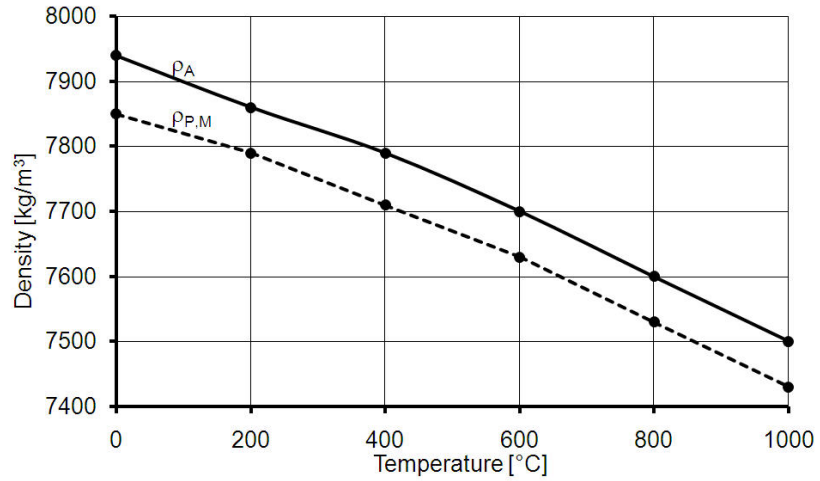


Figure A.16: Density vs. temperature, (C80)

A.4 Aluminum

Table A.5: Material properties of Aluminum [MPD99]

	0°C	100°C	200°C	300°C	400°C	500°C	550°C
Elasticity Modulus [GPa]	70	67.6	63.94	59.76	54.94	49.32	46.17
Poison's ratio [-]	0.33	0.33	0.33	0.34	0.36	0.39	0.41
Yield Strength [MPa]	12.4	10.58	8.76	6.95	5.13	3.31	2.4
Hardening Modulus [GPa]	0.78	0.725	0.671	0.616	0.562	0.507	0.48
Density [kg/m ³]	2704	2685	2665	2643	2620	2595	2582
Heat Conductivity [W/m/K]	234.4	240.1	237.5	232.4	226.5	219.6	215.8
Heat Capacity [J/kg/K]	878.7	939.7	986.2	1028.3	1073.8	1130.5	1165.6

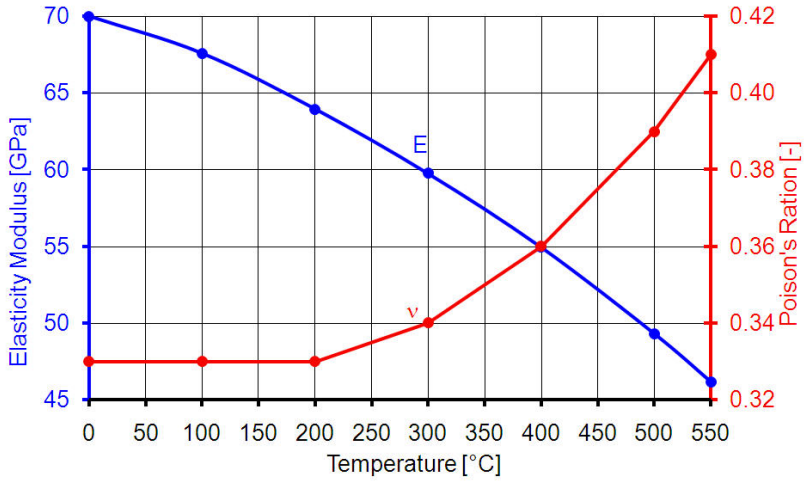


Figure A.17: Elasticity modulus and Poisson's ratio vs. temperature, (Aluminum)

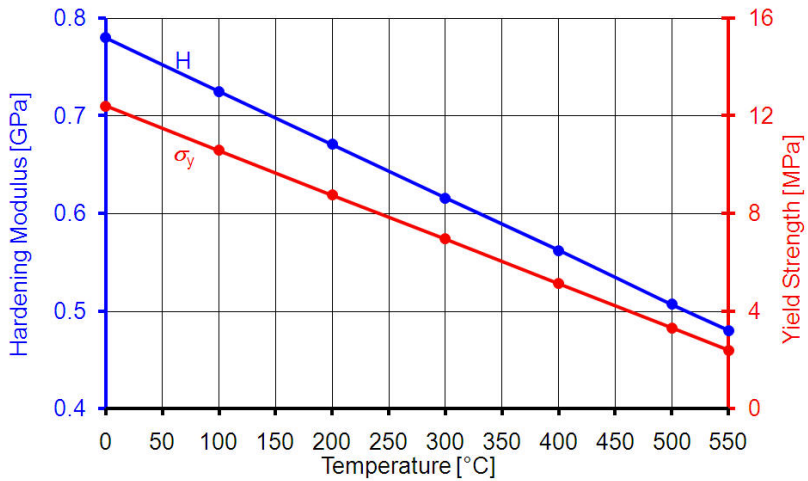


Figure A.18: Hardening modulus and yield strength vs. temperature, (Aluminum)

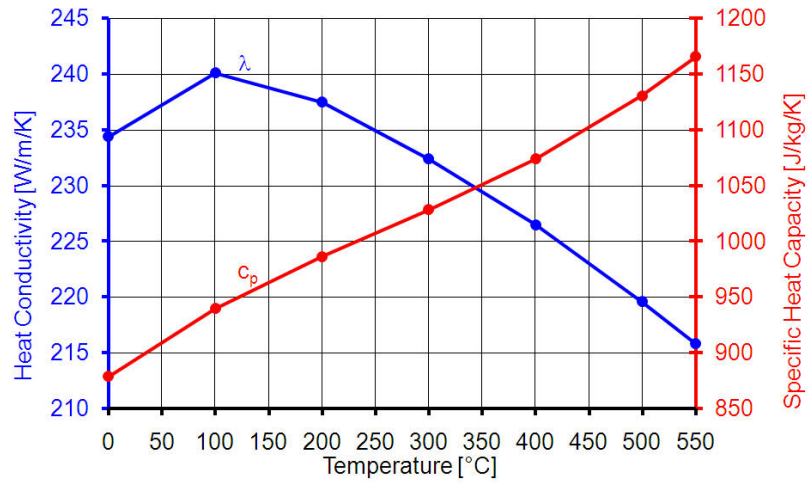


Figure A.19: Heat conductivity and specific heat capacity vs. temperature, (Aluminum)

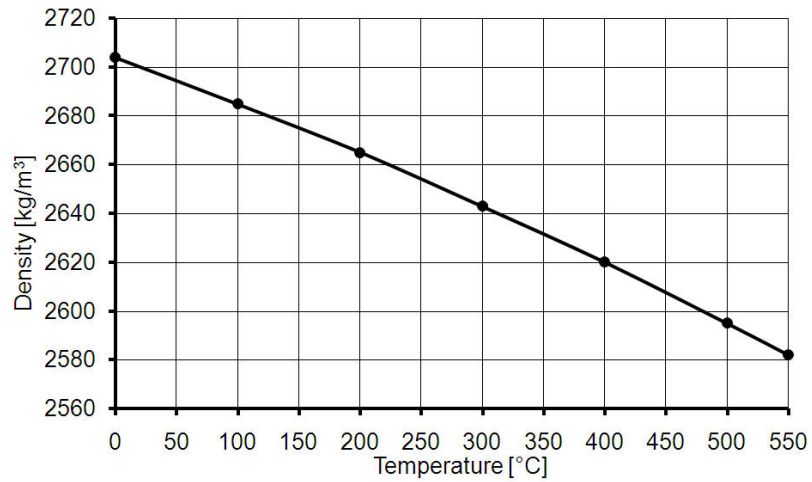


Figure A.20: Density vs. temperature, (Aluminum)

Curriculum Vitae

Personal data

Name: Yalçın Kaymak
Date of Birth: 08.07.1978
Place of Birth: Ankara, Turkey
Parents: Ali Sait Kaymak and Asiye Kaymak
Marital status: Single
Nationality: Turkish

School Education

1984–1988 Primary School, Şenyuva İlköğretim Okulu, Ankara
1988–1989 Primary School, Ayvalı İlköğretim Okulu, Ankara
1989–1992 Secondary School, Ayvalı İlköğretim Okulu, Ankara
1992–1995 High School, Ankara Gazi Lisesi

University Education

1995–2000 Undergraduate Studies of Civil Engineering,
Middle East Technical University, Ankara
2000–2003 M.Sc. in Structural Mechanics of Civil Engineering,
Middle East Technical University, Ankara
2003–2007 Ph.D. in Fluid Mechanics and Thermodynamics
Institute, Otto-von-Guericke University, Magdeburg

Professional Occupation

2000–2003 Teaching Assistant, Civil Engineering,
Middle East Technical University, Ankara
2006–2007 Research Associate, Fluid Mechanics and Thermodynamics
Institute, Otto-von-Guericke University, Magdeburg